TITANIUM-NIOBIUM BASED SHAPE MEMORY ALLOYS FOR MEDICAL IMPLANT APPLICATIONS

A Dissertation

by

Ji Ma

Submitted to the Office of Graduate Studies of

Texas A&M University

in partial fulfillment of the requirements for the degree of

DOCTOR OF PHILOSOPHY

May 2012

Major Subject: Mechanical Engineering

Titanium-niobium Based Shape Memory Alloys for Medical Implant Applications

TITANIUM-NIOBIUM BASED SHAPE MEMORY ALLOYS FOR MEDICAL IMPLANT APPLICATIONS

A Dissertation

by

Ji Ma

Submitted to the Office of Graduate Studies of

Texas A&M University

in partial fulfillment of the requirements for the degree of

DOCTOR OF PHILOSOPHY

Approved by:

Chair of Committee,	Ibrahim Karaman
Committee Members,	Raymundo Arroyave
	K. Ted Hartwig
	Dimitris Lagoudas
Head of Department,	Jerald Caton

May 2012

Major Subject: Mechanical Engineering

ABSTRACT

Titanium-niobium based Shape Memory Alloys for Medical Implant Applications.

(May 2012)

Ji Ma, B.S., Texas A&M University;

Chair of Advisory Committee: Dr. Ibrahim Karaman

Stress shielding is a potential problem facing the long-term reliability of structural medical implants such as knee and hip replacements. Because the large elastic modulus mismatch between the implant and the human bone, the load on the bone surrounding the implant is greatly reduced, causing a reduction in bone mass over time. This bone resorption causes difficulties in revision surgeries, and if left unattended, may eventually lead to the loosening of the implant. Thus, it is desirable to introduce an implant material that possess an elastic modulus comparable to that of the bone, while still retaining the other desired characteristics for biomedical alloys, such as strength, biocompatibility, corrosion resistance, and fatigue resistance. However, the lowest elastic modulus achieved so far in a biomedical alloy has been 55 GPa, more than double that of bones.

In this study, we achieve an effective elastic modulus as low as 25 GPa in a $Ti_{74}Nb_{26}$ shape memory alloy without sacrificing other mechanical properties. Furthermore, the alloy is able to automatically adjust its effective modulus based on the condition of the surrounding bone: when the implant carries a larger-than-desired portion of the load, its modulus will be reduced to transfer more load to the surrounding bone. This low effective modulus is brought about by the simultaneous activation of elastic deformation and stress-induced phase transformation enabled by superelastic cycling.

We utilize a combination of equal channel angular extrusion and post-extrusion heat treatments to optimize the microstructure and crystallographic

texture of the $Ti_{74}Nb_{26}$ shape memory alloy in order to achieve the best shape memory and superelastic response. We also investigate the effect of ternary zirconium alloy on these properties and further study the low-cycle functional fatigue behavior of the alloy to determine the microstructure that leads to the most effective modulus reduction. We find that microstructure plays a large role in the stability of the reduced effective modulus.

Finally, we confirm the excellent biocompatibility and corrosion resistance of the Ti-Nb shape memory alloys. Since they also possess comparable fatigue resistance to other biomedical alloys, we believe that they have the potential to bring significant improvements to medical implants.

ACKNOWLEDGEMENTS

I thank my research advisor, Professor Ibrahim Karaman for his guidance and support over my graduate research career. In the six years that I have worked with him, he has taught me many things and was always willing to help me when I needed it. Most importantly, he gave me the freedom and responsibility to steer the course of my own research, and allowed me to pursue my own research interests. This freedom has allowed me to growth tremendously, both as a researcher and as a person. For this I am forever grateful.

I would also like to thank Dr. Benat Kockar, who helped me a great deal during my first years of research work both in guiding me through many experimental techniques as well as helping me understand the fundamentals of shape memory alloys.

NOMENCLATURE

SMA	Shape memory alloys
ECAE	Equal channel angular extrusion
M_s	Martensite start temperature
M_f	Martensite finish temperature
A_s	Austenite start temperature
A_f	Austenite finish temperature
ΔT	Thermal hysteresis
$\Delta\sigma$	Stress hysteresis
ε_{irr}	Irrecoverable strain
ε_{rec}	Recoverable strain
σ_{SIM}	Transformation stress

TABLE OF CONTENTS

LIST OF FIGURES

FIGURE Page

FIGURE Page

FIGURE Page

FIGURE Page

LIST OF TABLES

1. INTRODUCTION: TOWARD A FLEXIBLE STRUCTURAL MEDICAL IMPLANT

As modern medical technology continues to increase the life-expectancy of patients worldwide, the requirements of long-term bio-implants, particularly those subjected to load-bearing applications such as hip and knee replacements, are repeated tightened. Not only must these implants maintain their functional capability over increasingly longer time periods, the biocompatibility and corrosion resistance of the material must be constantly improved to reduce the adverse physiological effects of the human body. In recent years, these strict requirements have shown signs of outpacing the existing biomedical implant technology, evident from a number of implant failures or implant-related medical emergencies that have surfaced [1-4]. These failures have largely resulted in the inherent limitations of the implant materials and their inability to satisfy all required design requirements for such applications, thus a new generation of implant materials is needed.

A structural implant material must satisfy a large number of strict requirements simultaneously: it must be strong enough to shoulder the loads of a human body; it must possess adequate fatigue resistance to withstand millions of load-unload cycles; it must not corrode or wear excessively to prevent leaching and buildup of debris inside the human body; it must be completely non-toxic, and it must form a good match with existing body structure to ensure it is adequately accepted by and incorporated into the body for a large number of years [4-8]. In addition, the requirement for longer implant durations also introduces and intensifies certain dormant difficulties, such as stress shielding. Such a material must be strong yet flexible, bio-inert yet allow for sufficient bio-integration. Such a material has not yet been used in existing implants.

Existing structural implant materials are generally made of stainless steel, Co-Cr alloys, pure titanium, or titanium alloys such as Ti-6Al-4V [7]. These materials each manage to satisfy a large portion, but not all of the requirements for

---

This dissertation follows the style of Acta Materialia.

bio-implant materials. In particular, none of these materials satisfactorily addresses the issue of stress shielding.

The effect of stress shielding in implants is both a controversial and an ambiguous one [9-16]. It is caused by the elastic modulus differences between the human bone (usually 10-30 GPa), and the implant, which exceeds 100 GPa in all materials that is currently being used [7]. This difference results in the majority of the load being carried by the implant. The surrounding bone, which experiences very little load, gradually undergoes resorption as a consequence of Wolff's Law [17] and weakens over time, and the resulting loss of bone mass (localized osteoporosis) may cause difficulties in revision surgeries, and possibly the loosening of the implant and other further complications with the associated bone loss. This effect of stress shielding on bone loss has been clearly demonstrated in both animal studies [9, 18] and clinical observations in humans [9, 11, 13, 14-16, 19, 20]. However, the direct relationship between stress shielding, bone loss and the failure rate of implants has not been clinically established [11, 12, 15]. However, while the effect of stress shielding can lay dormant for years, if left unattended, the potential outcome can be disastrous. Bone loss in the implant zone makes it nearly impossible to repair or replace the implant, and can cause major discomfort for the patient. Furthermore, the preservation of bone mass is an important goal for all orthpaedic surgery and implants. The ever-increasing expected lifetime of implants makes stress shielding an important issue to consider in structural implants.

It is then the aim of the present work to create a material that addresses the potential concerns of stress-shielding, while maintaining, if not improving upon the critical properties of existing implant materials. In this endeavor, we have successfully engineered a Ti-Nb based shape memory alloy with adequate strength and fatigue resistance, excellent biocompatibility and corrosion resistance, and an ultra-low effective stiffness of below 30 GPa, less than 1/3 the value of titanium-based biomaterials and 1/6 of stainless steel and Co-Cr alloys. This alloy is also

capable to automatically reducing its effective stiffness, thus transferring more stress to the bone, in response to any bone loss in order to slow the effect of stress shielding. It is our belief that the combination of properties possessed by the Ti-Nb shape memory alloy makes it a potential material capable of satisfying all of the requirements for a next-generation hip or knee implant.

2. TECHNICAL BACKGROUND

2.1. Stress shielding and requirements of medical structural implant materials

Structural implant materials such as hip and knee replacements procedures have eclipsed over 1 million per year [7] as shown in Figure 2.1, and the long lifetime of structural medical implants imposes many strict requirements both in its reliability and safety. As such, potential and new replacements are often put through rigorous testing and clinical trials. Despite these efforts, a significant number of implant failures still occur every year [21]. Unfortunately, because of the intrusive nature of the implant surgical procedure, a failed implant part becomes very difficult to replace, and the success rate for such revision procedures are generally much lower. These failures occur for various reasons ranging from excessive wear of the implant material, lack of biocompatibility, to the loosening of the implant [22].

A widely publicized case of implant failure occurred recently with Articular Surface Replacement (A.S.R.), a hip replacement manufactured by DePuy Orthopaedics, a division of Johnson & Johnson the largest maker of replacement hips worldwide. The ASR is a metal-on-metal implant that was first sold in foreign countries in 2003 and in the US in 2008 [1-3], and later recalled in 2009. Although designed to operate for 15 years and improve the range of movement for the patient, thousands of such implants have failed in only a couple of years. The implant, which is made of a cobalt-chromium alloy, suffers from wear problems that liberate cobalt residues that are toxic to the body, causing infections and acceleration the loosening of the implants [1-3]. The implant failed for the combination of inadequate wear resistance, and lack of biocompatibility of one of its elemental constituents. Cobalt-chromium alloys are normally considered to be safe due to the chromium oxide layers that envelopes the alloy. However, mechanical wear compromises this oxide layer and allow the toxic cobalt ions to be

liberated into the body. Thus, it is safer to use a material containing no bio-toxic elements.

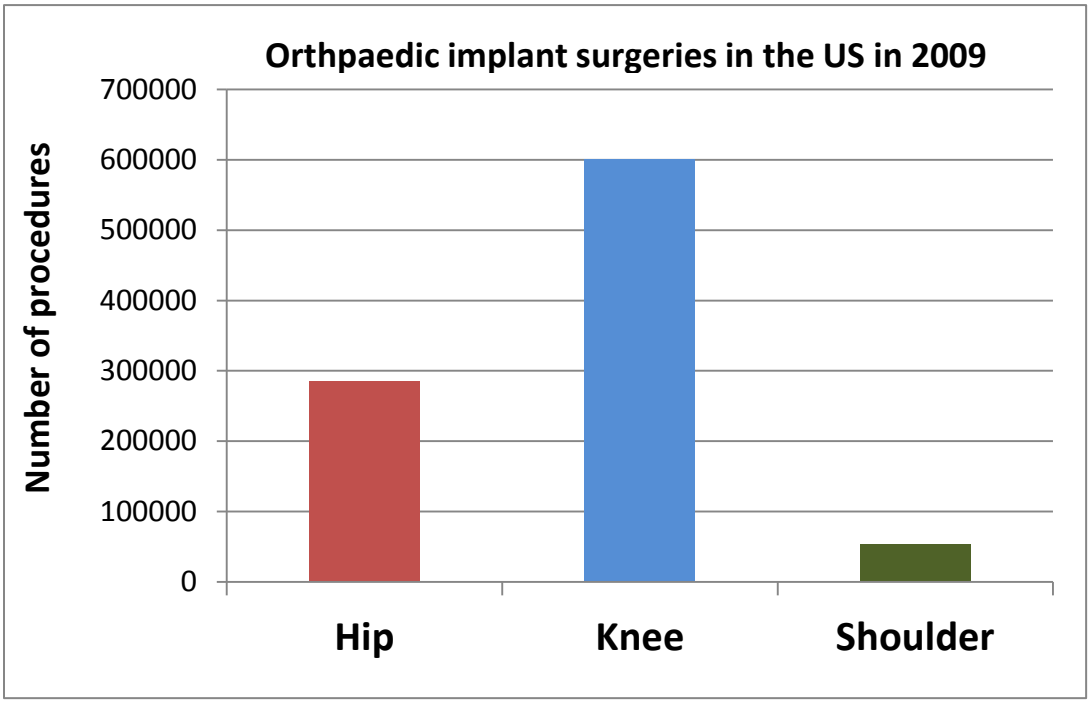

Figure 2.1. Estimated number of orthopedic operation procedures in the United States per year. Source: American Academy of Orthpedic Surgeons [7, 24].

While wear and toxicity are long-considered problems in the medical implant community, there is another potential criterion that lurks. The elastic modulus of the implant material, often a stainless steel or Co-Cr alloy, is about 10 times higher than the elastic modulus of the human bone (Figure 2.2). Since load of the body is then carried with the implant and the surrounding bone in parallel, the stiff implant will carry a large majority of the load, given by Equation 2-1.

$$\frac{E_1}{E_2} = \frac{\sigma_1}{\sigma_2} \qquad \text{(Equation 2-1)}$$

Where E_1 and E_2 are the elastic moduli of the implant and bone, respectively, and σ_1 and σ_2 are the respective stress they carry when loaded in parallel. Although the actual stress state of the bone and implant is much more complicated than Equation 2-1, the effect of stress shielding occurs for the same reasons. The bone, which is a living tissue that constantly adapts itself to the surrounding, will become weaker as a result of lack of loading, according to Wolff's Law [17]. Over time, this leads to the reduction of bone mass (resorption) and bone quality of bones that surrounds the implant.

Loss in bone density caused by stress shielding is frequently observed in patients receiving implants in numerous studies [9, 13-15, 18]. The reduction of mineral density in the bone surrounding an implant is generally estimated to be up to 50% after three years of implantation [9]. It was also estimated that pronounced bone resorption occurred in 33% of patients receiving implants after 5-13 years [9]. This was echoed by the study of McAuley [19, 20] which demonstrated about 18.4% loss in the bone mineral density of patients due to stress shield in implants which porous-coated stems, compared to about 40% loss in bone mineral density in implants without stem coating. Scott and Jaffe [23] also reports about 22-26% loss in bone mineral density of the femur bone of implants with hydroxyapatite coatings after 5-7 years of implantation. Overall, the observed loss of bone mass show a very large spread from 7% to over 50%

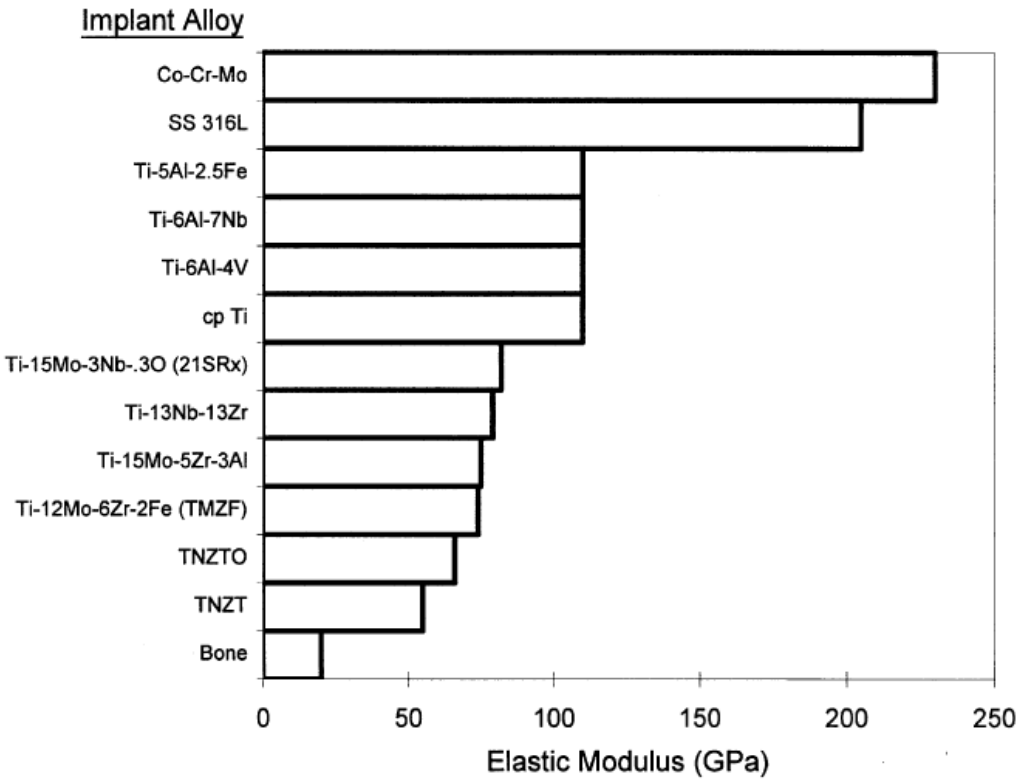

Figure 2.2: Elastic modulus of a variety of engineering materials compared to that of the human bone. At the present, only stainless steel, Co-Cr alloys, cp-Ti and Ti-6V-4Al alloys have actually been used in actual implants [5].

However, the widespread loss in bone density has not been shown to lead to deterioration of implant performance. Engh *et al*. [11] studied 223 porous-coated hip implants that have been implanted for a minimum of 2 years and an average of 13.9 years. While signs of stress shielding from bone resorption was observed in over 20% of the cases. However, there was no statistically significant difference in the survival rate of implants showing signs of stress shielding and those that do not. Loosening of the implant was not observed in any of the cases showing signs of stress shielding. No bone fracture occurred, and there were otherwise no complaints of discomfort or pain from patients. This was in agreement with an

earlier study [12] which also concluded that stress shielding did not lead to a statistically significant increase in implant failure rate nor patient discomfort. More unclear is the effect of bone loss in the difficulty of revision surgeries, and neither study show sufficient data to form a definite conclusion.

On the other hand, a recent study directly correlated a failure in a femoral endoprosthesis with stress shielding in a transfemoral amputee [15]. This implant with porous coating was designed to support the stump of the amputee to allow better fit and load transfer with the leg prosthesis. Although no signs of problems was observed during a 12-month follow up, which reported improved alignment of the implant with the patient's leg, At 24 months after implant, the patient suffered a minor trauma with resulted in the fracture of the femur bone. The bone surrounding the implant showed extensive osteoporosis from the effect of stress shielding, and is believed to be the primary reason for the failure.

The femoral endoprosthesis is an experimental implant with a much wider implant stem than a conventional implant used in total hip replacements [15]. Thus, it is likely that bone resorption caused by stress shielding is much greater in this case. This means that it is likely that the lack of clinical evidence for adverse effect of stress shielding in total hip replacements is related to the relatively small degree of bone resorption. If the magnitude of bone loss becomes high enough, stress shielding is expected to become a significant contributing factor to failure.

2.2. Shape memory alloys and applications to medical implants

2.2.1. Properties of shape memory alloys and medical applications

Martensitic transformation is a solid-to-solid phase transformation that occurs through a coordinated shear movement of atoms over very short (on the order of angstroms) distances where atoms retain their neighboring relationship with one another. The high temperature phase, austenite, transforms to a low temperature phase, martensite, upon cooling. Because the crystal structure of

austenite is different than that of martensite, it is possible to obtain a macroscopic shape change that accompanies the transformation.

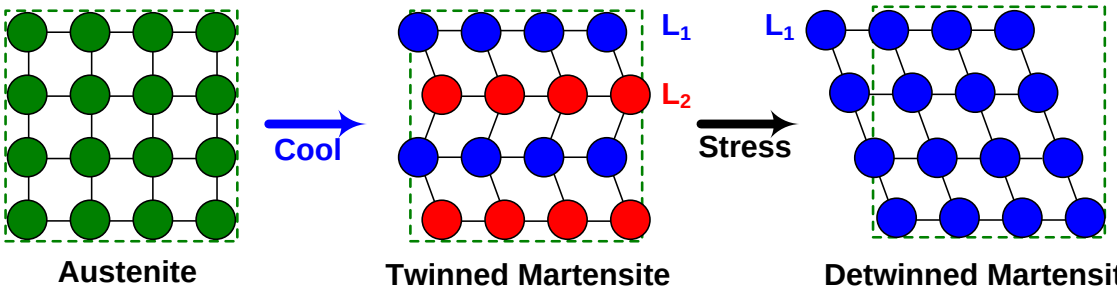

Figure 2.3: A simplified illustration of the austenite and martensite structures at the atomistic level. In the absence of stress, austenite transforms to twined martensite upon cooling in order to accommodate strain caused by a change in crystal structure. The twinned martensite is composed of multiple twin-related lattice correspondence variants, labeled L_1 and L_2 in this figure. When stress is applied, the martensite may detwin, resulting in a single lattice correspondence variant structure and a net shape change.

When martensite forms inside austenite, the difference in their crystal structures generates large local strain. This strain is large enough so it cannot be purely accommodated elastically. Instead in SMAs, the strain is accommodated by producing a twinned martensite structure (see Figure 2.3). When the higher symmetry austenite transforms to the lower symmetry martensite, it may do so in several "ways" called martensite lattice correspondence variants. The number of such variants that can be formed is determined by the crystal structure of martensite and austenite. For example, there are 12 lattice correspondence variants of a monoclinic martensite to a cubic austenite [25]. In essence, each lattice correspondence variant is a "variation" of the martensite with a different

orientation relationship to the austenite, but they are all energetically equivalent to one another under stress-free conditions. By forming a structure of twin-related lattice correspondence variants, the martensite is able to accommodate a large portion of the strain associated with the change in crystal structure. These twin-related lattice correspondence variants are collectively referred to as a habit plane variant, and several different habit plane variants can then be formed in such a way that together, they eliminate the remaining strain of the transformation. This means that the transformation from austenite to martensite can be made to cause nearly no macroscopic shape change, and the resulting structure of the martensite phase that accomplishes this is then considered to be "self-accommodated", as seen in Figure 2.4. Under an external biasing stress, certain habit plane variants become energetically favored and form or grow at the expense of others in a process known as martensite re-orientation. In addition, the martensite may also detwin, where analogously, the lattice correspondence variant favored under stress grows at the expense of others. Both martensite re-orientation and detwinning results in the macroscopic shape change, and give rise to the shape memory behavior and superelasticity. More details can be found in literature regarding the nature of martensitic transformation [26-28], structural description of twinning in martensite [29-35], and self-accommodation [36-39]. For the sake of simplicity, detwinning and martensite reorientation will not be treated separately in this introductory section.

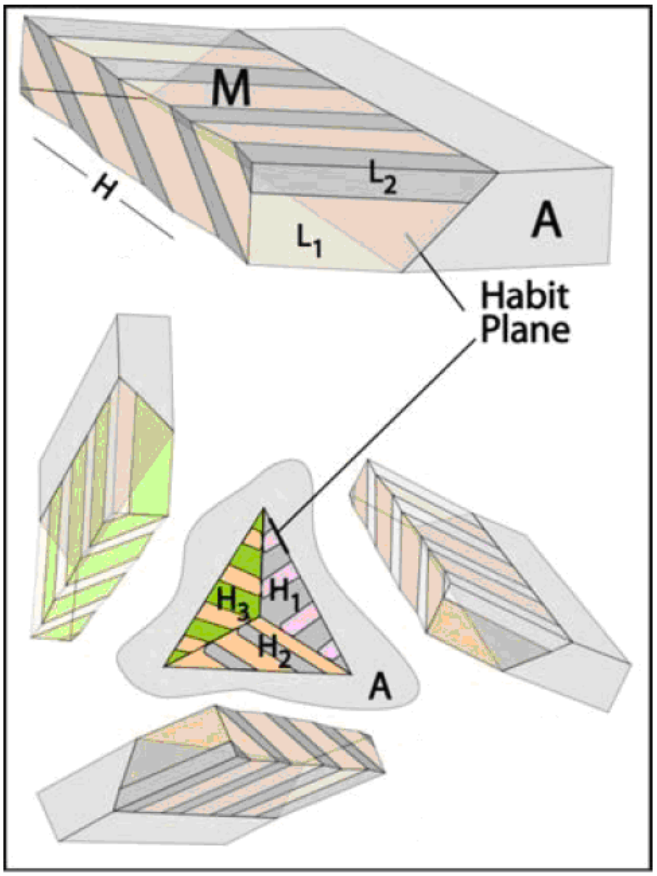

Figure 2.4: Process of self-accommodation in martensite [40]. L_1 and L_2 are two different lattice correspondence variants. Without stress, pairs of twin-related lattice correspondence variants form a habit plane variant (H_1, H_2, H_3), and several habit plane variants can then arrange themselves in such a way that results in no net shear, and approximate no volume change from the transformation, shown in the middle triangle. When external stress is applied, the degeneracy of the various habit plane variants and lattice correspondence variants are lifted, and the most favorable variant – the one most fit to accommodate the desired strain – is formed at the expense of others.

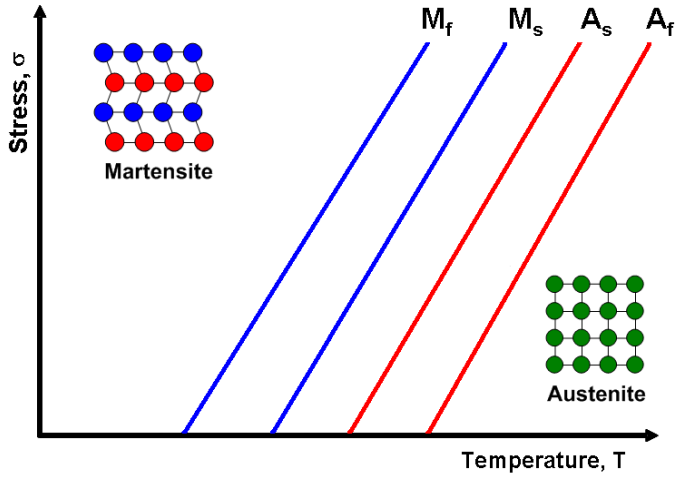

Figure 2.5: A σ-T phase diagram of SMAs undergoing martensitic transformation. Above A_f, the specimen is fully in the austenite state, and below M_f, the material is fully martensitic.

The martensitic transformation can be induced both thermally and through the application of stress. In other words, application of stress and reduction in temperature both act as driving forces for the austenite → martensite transformation. In fact, there is a linear relationship between the two. This relationship is derived from the thermodynamics relationships of phase transformation and is called the Clausius-Clapeyron relationship. Roughly, it states that $\frac{d\sigma}{dT} = constant$.

The real transformation process, however, is much more complicated. In general, the transformation is not completed immediately at a single temperature, but occurs gradually over a range of temperature. The temperature during cooling at which the transformation from austenite to martensite, or the forward transformation, first begins is called the martensite start (M_s) temperature. The temperature at which the forward transformation reaches completion is called the martensite finish (M_f) temperature. Conversely, upon heating above the austenite

start (A_s) temperature, the martensite begins to transform back to austenite - the reverse transformation. The temperature at which reverse transformation is completed is austenite finish (A_f) temperature. Each of these temperatures follows a Clausius-Clapeyron shown in Figure 2.5. However in reality, the slopes of the σ-T relationship of each transformation temperature are generally not the same, and may not even be a straight line due to the effect of microstructural features such as grain size, and microstructural mechanisms such as dislocation slip. Nevertheless, idealized versions are used here for simplicity and to convey the important parameters/mechanisms.

The deformation response of SMAs depends on the testing temperature relative to the transformation temperatures (M_s, M_f, A_s, and A_f) of the alloy. If the material is deformed below the M_f temperature in a self-accommodated martensite structure (Figure 2.4), then the strain is accommodated by the growth of one variant favored by the stress in the expense of others, as well as detwinning (Figure 2.6). Since all martensite variants are equally stable in the absence of external and internal stresses, the martensite stays in the re-oriented and detwinned state, and remains in the deformed shape after unloading. When heated above A_f temperature after unloading, all martensite transforms back to austenite. When the austenite is once again cooled below M_f, the martensite will again form in a self-accommodated state, and all deformations from detwinning are recovered in the absence of plasticity; this is the one-way shape memory effect (Figure 2.6). This means that the austenite shape of the alloy is “remembered”, and the material can return to this shape even after deformation in the martensite state. This ability enables “deployable bio-devices” that are deployed in a deformed martensite state to facilitate easy installation, and then morphs into the desired shape as it is warmed to body temperature.

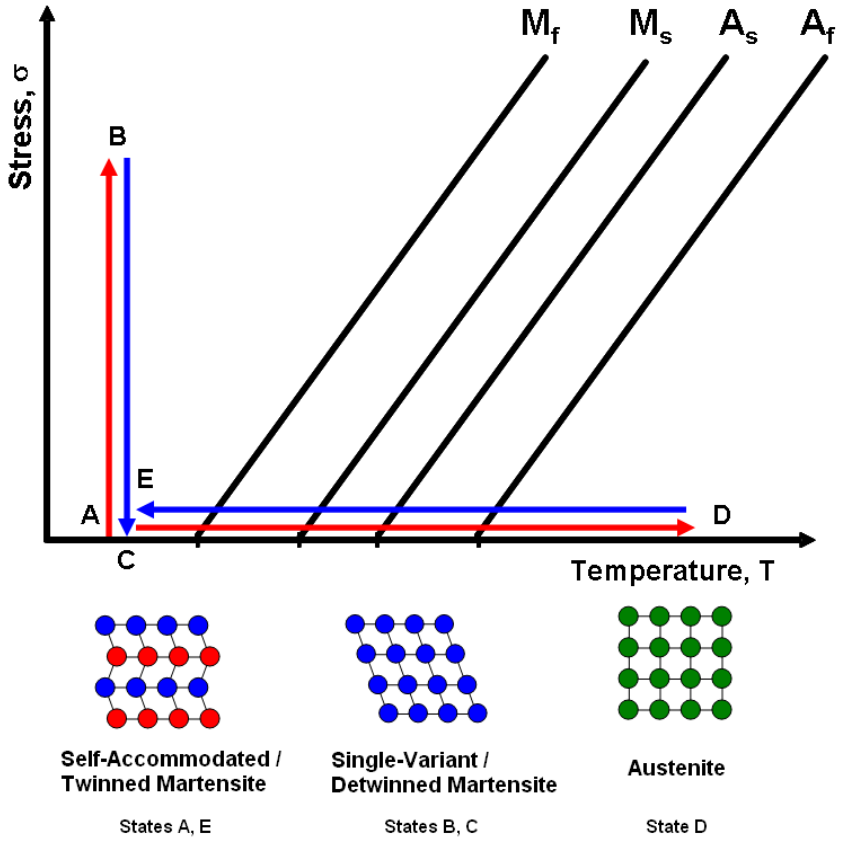

(a)

Figure 2.6: (a) Demonstration of the shape memory effect using σ-T phase diagram. An initially twinned (self-accommodated) martensite (state A) is deformed at temperature below M_f, causing it to detwin (state B) and remain in the detwinned state after unloading (State C). This leads to an external shape change (shown in (b)). Upon heating to above A_f, the detwinned martensite transforms fully back into austenite (state D), which again transforms to twinned (self-accommodated) martensite when cooled below M_f, restoring the initial shape. (b) Demonstration of the shape memory effect on a σ-ε diagram [41].

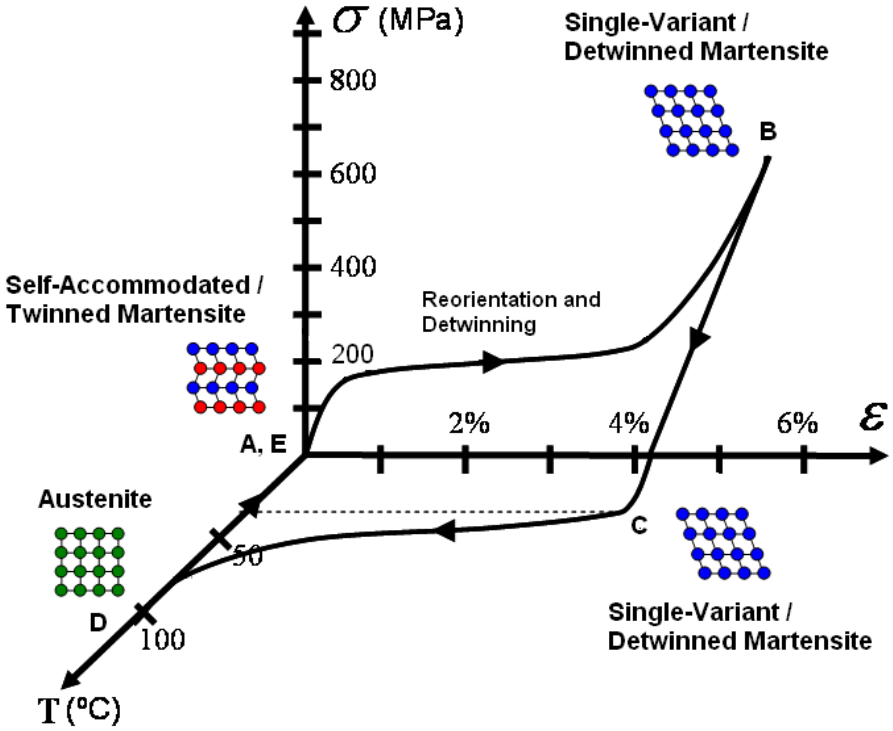

(b)

Figure 2.6 Continued

On the other hand, if sufficient stress is applied in the austenite state, the austenite may transform into martensite in a single-variant configuration, which results in a macroscopic shape change. When the stress is removed, however, the martensite becomes unstable and reverts to austenite, and recovers this change in shape. This effect is known as superelasticity (Figure 2.7): the material is able to sustain a large amount of recoverable strain (up to 20% in some single crystals and 8% in commercially available SMAs), and functions as a "super-spring". The flexibility has been utilized in a number of biomedical applications such as orthodontic arch wires and temporarily bone staples and braces to promote healing.

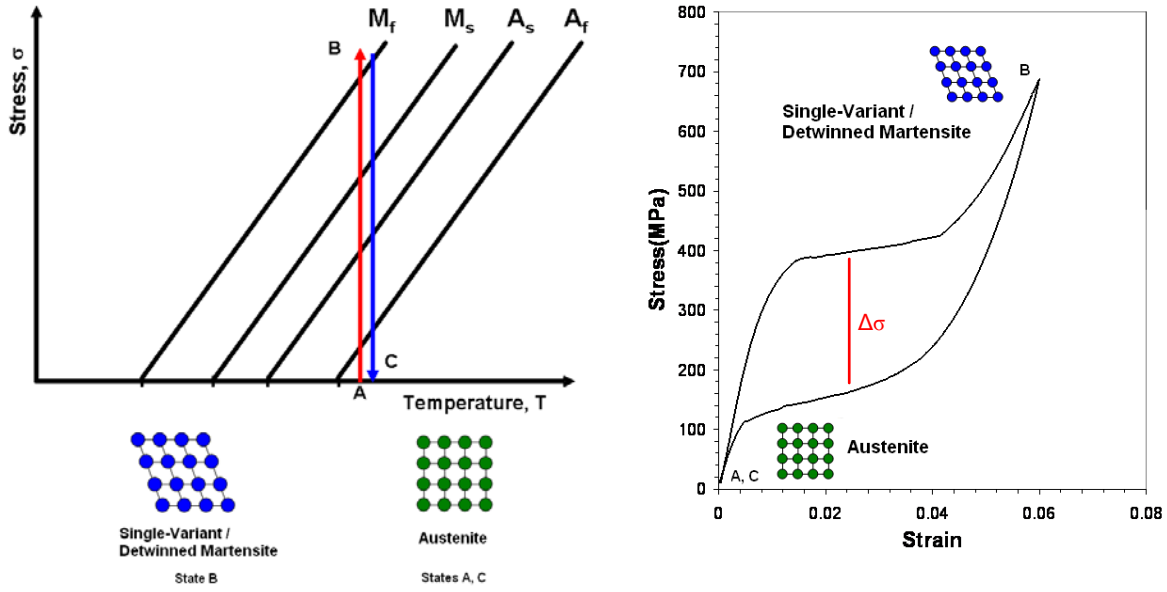

Figure 2.7: (a) Demonstration of superelasticity using a σ-T phase diagram. Initial austenite (state A) is deformed at temperatures above A_f, and with sufficient stress, becomes fully martensite in detwinned state (state B). When stress is removed upon unloading, the specimen returns to a fully austenite state and recovers all imposed deformation immediately (state C). (b) Demonstration of superelasticity on a σ-ε diagram [41].

These two unique abilities of SMAs have greatly simplified the surgical procedures of some implant operations, as well as improved upon the performances of many medical devices and components. For these reasons, SMAs have established a firm foothold in the medical devices and small implants market, and is now a multi-million dollar industry. Yet, there is one major medical implants market that SMAs have yet to penetrate – the long-term, structural medical implants such as knee and hip implants, where the unique properties of SMAs may have profound impacts.

2.2.2. Shape memory alloys and medical structural implants

In the scientific and technical literature, SMAs have been mentioned numerous times as a potential material for orthopaedic implants. However, the main reason for their inclusion generally has little to do with their shape memory or superelastic behavior. Instead, the workhorse Ni-Ti SMA (nitinol) is known to possess much lower elastic modulus than currently used implant alloys. In the austenite state, nitinol is reported to have an elastic modulus of between 60-80 GPa, while in the martensite state, this number is 30-60 GPa [7]. The low stiffness reduces the risks of stress shielding and makes Ni-Ti an attractive implant material: not as a shape memory alloy, but simply a metallic alloy with low elastic modulus.

However, the low martensite modulus of nitinol is a misleading one. Numerous neutron diffraction, atomistic simulation, and synchrotron diffraction work has shown that the actual elastic modulus of the martensite is well over 100 GPa [42-45]. The reason that a small modulus is observed in a conventional stress-strain diagram is the simultaneous activation of martensite reorientation and martensite detwinning alongside elastic deformation [42, 45]. Unfortunately, strain caused by martensite reorientation and detwinning does not recover upon unloading, so even at very low applied stress level, irrecoverable strain can be observed in a stress-strain diagram of nitinol in the martensite state. This means that nitinol cannot be used in the martensite state as an implant material as it will continuously undergo permanent shape change as stress is applied.

On the other hand, the low “apparent’ modulus of the nitinol martensite provided us with the inspiration for our work. Instead of irreversible mechanisms such as martensite reorientation or detwinning, it may be possible to activate a reversible deformation mechanism, such as stress-induced phase transformation, concurrently with elastic deformation to reduce the effective modulus of the alloy. In most shape memory alloys, including nitinol, the stress required to activate stress-induced phase transformation are quite high (~200-300 MPa). Since

implants do not typically experience such loads, it is not possible to take advantage of this mechanism.

2.2.3 Ni-Ti shape memory alloys and their concerns

Ni-Ti SMAs, known commercially as “nitinol”, is the staple and workhorse of shape memory alloy applications. They possess very high transformation strain up to 8%, excellent strength, and good corrosion resistance and biocompatibility. With adequate workability and transformation temperature near the human body temperature, they are the natural choice for biomedical applications, and are currently the only commercialized shape memory alloys.

However, there have been some recent concerns raised about the biocompatibility of nitinol due to the high nickel concentration of the material. While nickel is an essential element to the human body, it is also known to be toxic in a large enough dosage. Furthermore, it is reported that 4.5% [46] to 8% [47] of the general population are hypersensitive to nickel. Nickel has been shown to be toxic [48-50], and possibly carcinogenic [51-53]. This has raised questions regarding the long term use of Ti-Ni due to the possibility of large amounts of nickel release into the body, particular in large implants such as hip replacements.

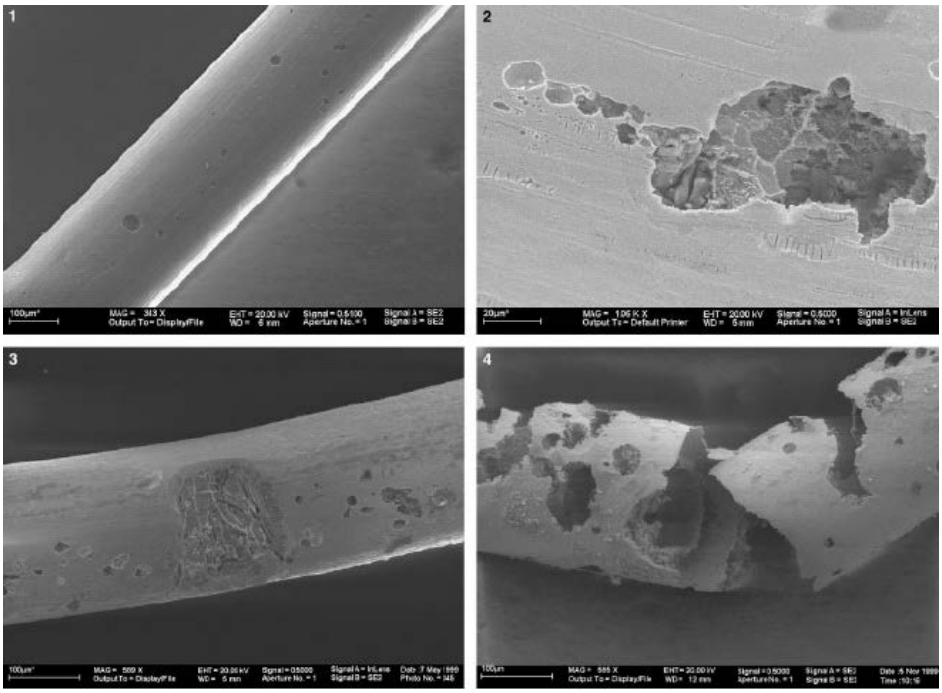

Figure 2.8: SEM images of Ti-Ni wire segments from endovascular grafts. 1. A 16-month-old stent containing corrosion pits. 2. A close-up of one of the corrosion pits in a 21-month-old stent. 3. A 34-month-old stent showing large corrosion defects. 4. Complete disintegration of a 9-month-old stent component [54]

It was argued in numerous in vivo and in vitro investigations that nitinol is at least as biocompatible as pure titanium [48, 55-61]. However, several recent clinical and in vivo studies, especially on Ti-Ni endovascular stents, have challenged the corrosion resistance and safety of Ti-Ni alloys in the body [62-72]. Shih et al. [63] demonstrated the cytotoxicity of corrosion products of nitinol, which has also shown to have a local inflammatory effect by causing increased monocyte secretion [68]. Heintz *et al.* [54] found severe corrosion in explanted endovascular stents from patients after relatively short use. All stents contained some form of corrosion damage, as shown in Figure 2.8 and Figure 2.9. It was suggested that the damage was due to the corrosion under dynamic stress conditions [68]. Such corrosion can

be detrimental since, once slightly corroded in vivo, nickel ions can escape and cause production of functionally distinct cytokines and reactive oxygen species. In addition, many authors have pointed out the lack of consistent long-term in-vivo biocompatibility data for Ti-Ni [56, 58].

Nevertheless, nitinol medical components and devices are actively used in applications today. Concerns regarding ion leaching are relevant when the amount of ion release is large. Most nitinol devices, such as stents, are quite small in size, thus large release is not expected. However, this may not be necessarily true in large implants such as the hip or knee replacements. Here, the effects of nickel release may become magnified. Further study is needed to clarify this concern.

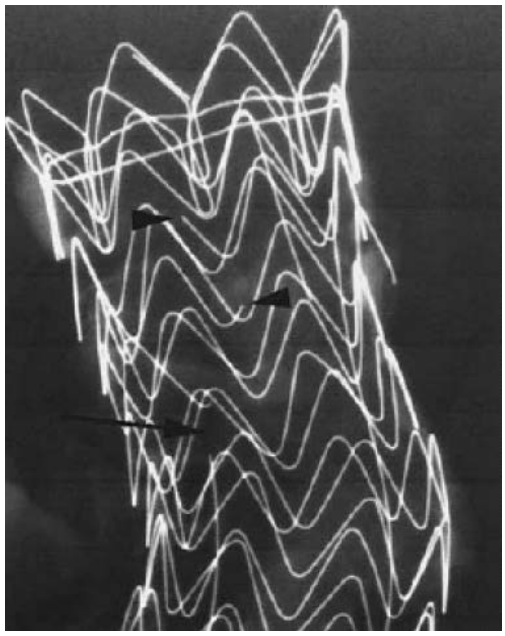

Figure 2.9: Mechanical failure of an endovascular TiNi stent graft after 32 month of use [69]

2.2.4. Ti-Nb Shape Memory Alloys

In light of such controversies on Ti-Ni, new Ni-free Ti SMAs with bio-inert constituents have recently been proposed as life expectancy and need for implants grow at an ever faster pace. Two major systems have been the Ti-Mo [73-78], and the Ti-Nb systems [79-105]. In addition, many ternary alloys have been developed in the last three years with the addition of Ag, Ga, and Sn [73,74] to the Ti-Mo system, and Al [82-84], Ga [81, 85], Ge [82, 85], In [82], Pd [99, 100], Si [95], Sn [82, 102, 103], Ta [93, 103-105], and Zr [90, 105] to the Ti-Nb alloys. In this work, we will focus on Ti-Nb over the Ti-Mo systems for two primary reasons. Ti-Mo alloys are in general susceptible to ω phase embrittlement [73, 78]. More importantly, Ti-Nb systems have exhibited higher recoverable strain levels. $Ti_{72}Nb_{22}Zr_6$ currently exhibits the highest total recoverable strain of 4.5% among all Ti alloys other than Ti-Ni [90]. This is superior to the best recoverable strain of 4.0% in the Ti-Mo-Ga system [73]. Moreover, Koster et al. [106] have demonstrated Mo contact allergies in some patients, making Ti-Nb system a more plausible choice.

The development of TiNb SMAs has received little attention in the past, even though Baker [79] first reported the SME in $Ti_{78.3}Nb_{21.7}$ in 1971, presumably due to the low transformation strain. Only recently in 2004, did Kim *et al*. [89] performed a systematic study on the shape memory and superelastic properties of the Ti-Nb system. However, the study of the shape memory behavior of the Ti-Nb system is still at its infancy and holds great promise, especially for the biomedical industry due to its potential for high biocompatibility, corrosion resistance, superior workability, and relatively low Young's modulus.

The most immediate advantage of Ti-Nb SMAs over Ti-Ni is the biocompatibility of all constituents [107-109]. It was reported [107, 109-111] that the surface oxide layer provides Ti-Nb a better corrosion and wear resistance than that of Ti-Ni and Ti since both Ti and Nb can form protective surface oxides. Lee *et al.* [111] demonstrated that should the oxide layer be compromised and particles are set free into the human body, Nb will be spontaneously passivated due to its

low anodic current potential. In addition, Ti-Nb alloys are very easy to process as compared to Ti-Ni alloys and can be cold rolled at room temperature to 99% reduction in thickness without any intermediate annealing steps, even in the as-cast form [83, 92, 95]. They also possess good machinability [112] and the sensitivity of their transformation temperatures to compositional change is considerably less than that of Ti-Ni, with a change of 40 °C/at.% Nb compared to 150 °C/at.% Ni in Ti-Ni [89]. Fatigue behavior of Ti-Nb SMAs in the superelastic regime has not been studied so far.

In addition to the significant new opportunities and superior characteristics of the Ti-Nb SMAs, there are few issues that must be addressed in order to make them viable. Three major ones are: 1) relatively low transformation strains on the order of 3-5% as compared to that of Ti-Ni alloys (6-8%), 2) low critical stress for plastic deformation, both of which limit the maximum recoverable strain achievable in Ti-Nb alloys, and 3) a lack of information on material impact on cell adhesion and viability and on material corrosion and fatigue in response to dynamic physiological loading conditions. Even though cyclic superelastic response of these alloys is not known, low critical stress for plastic deformation would cause poor cyclic recoverability. As superelasticity has a vital importance in biomedical applications, it is then essential to improve these properties.

The major known problem of the new Ti-Nb SMAs is low critical shear stress for dislocation slip which negatively affects superelastic strain and is likely to cause poor fatigue response. There are five approaches to tackle with this problem: alloying, coherent precipitation, strain hardening, grain size refinement (nanocrystallization) and texture strengthening. We will utilize all of these approaches in order to improve the shape memory, superelastic, and basic mechanical properties of the Ti-Nb shape memory alloy in this study.

It is confirmed recently that critical shear stress for dislocation slip in TiNb SMAs can be improved by ternary additions such as Sn, Al, Ta, and Zr [83, 90, 93, 99, 100, 102, 104]. Moreover, these ternary additions, in general, increase

transformation strain levels [80-84, 90, 94, 95, 99, 100, 102-105]. For example, the $Ti_{72}Nb_{22}Zr_6$ alloy has been shown to possess the highest transformation strain (4.5%) among all Ti-Nb alloys [90]. However, the cyclic superelastic responses are still poor because of insufficient increase in yield strength upon alloying [90]. Therefore, further improvement is needed. Similarly, interstitial oxygen addition increases the critical shear stress for dislocation slip and recoverable strain levels without significantly affecting the fracture strain up to 1 at.% oxygen [91]. However, the increase in the recoverable strain levels is not as high as that obtained from Zr addition. Such relative insensitivity of Ti-Nb to oxygen is significant because in Ti-Ni, even small amount of oxygen negatively affects the shape memory response, processability, and reduces the ductility.

Kim *et al.* [92] demonstrated the effectiveness of nano-precipitation in increasing the critical shear stress for dislocation slip in the binary alloys. Cyclic response of this material was better as compared to that of Ti-Nb-Zr alloy, however, the material still suffered from cyclic deterioration of the superelastic strain. The precipitation hardening behavior of ternary alloys has not been studied yet. Similarly, the effect of the amount of cold work has been partially studied demonstrating some improvement in cyclic stability and superelastic strain level.

Texture dependence of transformation strain yield strength was experimentally studied by Kim *et al.* [93] in cold-rolled Ti-Nb-Ta ternary, however, Ta is not as efficient in increasing the transformation strain as Zr and cyclic superelastic response was not studied. It should be emphasized that texture can have a strong effect on yield strength and elastic modulus.

From this discussion, it is clear that in addition to the reduction of the effective modulus, the mechanical and superelastic properties of the Ti-Nb SMAs must be sufficiently improved through work hardening, grain refinement, and crystallographic texture engineering in order to be considered a feasible material for structural implants. In the present work, the severe plastic deformation

technique Equal Channel Angular Extrusion (ECAE) will be used to achieve these requirements.

2.3. Equal Channel Angular Extrusion (ECAE)

ECAE permits the application of a large amount of strain without a reduction in work piece cross section and results in large processed billets. ECAE tool is made out of two intersecting channels of equal cross-sections with the intersecting angle of usually 90°. The rationale behind the selection of ECAE as the main processing technique here is several fold. First, the possibility of repeated extrusions without changing cross-section allows more effective grain refinement in bulk materials than any other known technique [113]. Secondly, the conservation of square cross sections make it possible to apply different rotation sequences after each ECAE pass leading to so-called ECAE routes. Such robustness lets ECAE to control the development of texture [113-115]. Thirdly, we can currently process billets as large as 2" x 2" x 12" and larger cross sections can easily be processed with low extrusion pressures using ECAE tools with sliding wall concepts [116]. For biomedical applications where required parts are relatively small, it could be possible to cut these parts along different directions in these large billets depending on the desired texture. On the other hand, the billet is also large enough for hip implants. Finally, the proposed nanocrystallization technique can be achieved uniformly in one ECAE pass (single step) as compared to multiple rolling reductions which can only produce non-uniform nanocrystallization.

2.4. Low-cycle and functional fatigue in shape memory alloys

As SMAs experiences forward-reverse transformation cycles multiple times, their shape memory and superelastic properties undergo changes caused by defects generated and modified by the transformation. These changes may include an increase or decrease in transformation temperatures, reduction of stress and thermal hysteresis, accumulation of irrecoverable strain, and changes in the

hardening rate of the stress-strain diagram [97, 101, 117-119]. In applications, cyclic functional fatigue is undesirable since it alters the properties of the alloy, causing it to deviate from its desired engineering response. However, functional fatigue can generally be stabilized after a number of transformation cycles, such that further cycles no longer affect properties appreciably, and in many applications, SMA components are subjected to such a stabilization process known as training to improve the predictability of the alloy response.

These transformation-induced changes are caused either by the generation of defects or retained martensite during transformation [101, 117-119]. As the interface between martensite and austenite form and move, defects are generated at the boundary because the lattice mismatch between the two phases, causing dislocations to form to relieve the accumulated internal stress. However, the precise effect of cyclic functional fatigue depends on the method by which the transformation occurs. When a SMA transform from changes in temperature under stress-free conditions, the transformation temperatures generally decrease. As transformation takes place, dislocations are generated at the interface between martensite and austenite. However, since no stress is applied, martensite is formed in the self-accommodated state and the stress field from the generated defects is randomly oriented. This means that no specific martensite variant is favored by the defects and as a result, the defects hinder the phase transformation by acting as obstacles to the movement of the phase front in subsequent transformation cycles. Austenite is stabilized over the martensite and transformation temperatures are decreased.

On the other hand, if thermal-induced transformation occurs under applied stress, or if transformation is stress-induced, transformation cycles will increase the transformation temperatures of the alloy. Dislocations formed during these cycles are oriented and favors specific martensite variants, and thus the energy required to active the transformation of these variants are reduced, and martensite becomes stabilized compared to austenite [120].

In structural implant applications, SMAs are used for their superelasticity. The focal point of present study is therefore the cyclic response of stress-induced phase transformation. Stress-induced phase transformation cycles cause three main changes in the stress-strain response of the alloy: 1) the transformation stress will gradually decrease with the number of cycles due to the increase in transformation temperature; 2) transformation stress hysteresis will be reduced, and 3) irrecoverable strain will be accumulated. These changes are illustrated in Figure 2.10.

The aforementioned changes in the superelastic properties due to low-cycle functional fatigue have largely been explained by the generation of dislocations at the phase boundaries, similar to the explanation used for thermal-induced transformation of SMAs. However, recent studies have revealed that retained martensite play a large role in the changes in superelastic behavior. When the material is loaded again, it no longer requires nucleation of martensite since martensite already exists in the matrix. Instead, the retained martensite simply grows. Since nucleation is reduced or eliminated, the energy barrier for the austenite → martensite transformation is significantly reduced, thus the stressed required to trigger stress-induced transformation is also reduced. It is generally believed that the martensite is retained by dislocations, but other mechanisms [117, 118], such as point defects and precipitates, have also been suggested as possibilities [97, 98, 120-122].

In the present work, we used the effect of superelastic cycling as a tool to reduce the effective modulus of the alloy. At the same time, we showed that the changes in superelastic properties sustained during low-cycle fatigue are in many cases reversible. The recovery kinetic is an order of magnitude faster than expected for simple dislocation recovery. This finding suggests that the functional fatigue of superelasticity in SMAs is much more complicated than the action of dislocations.

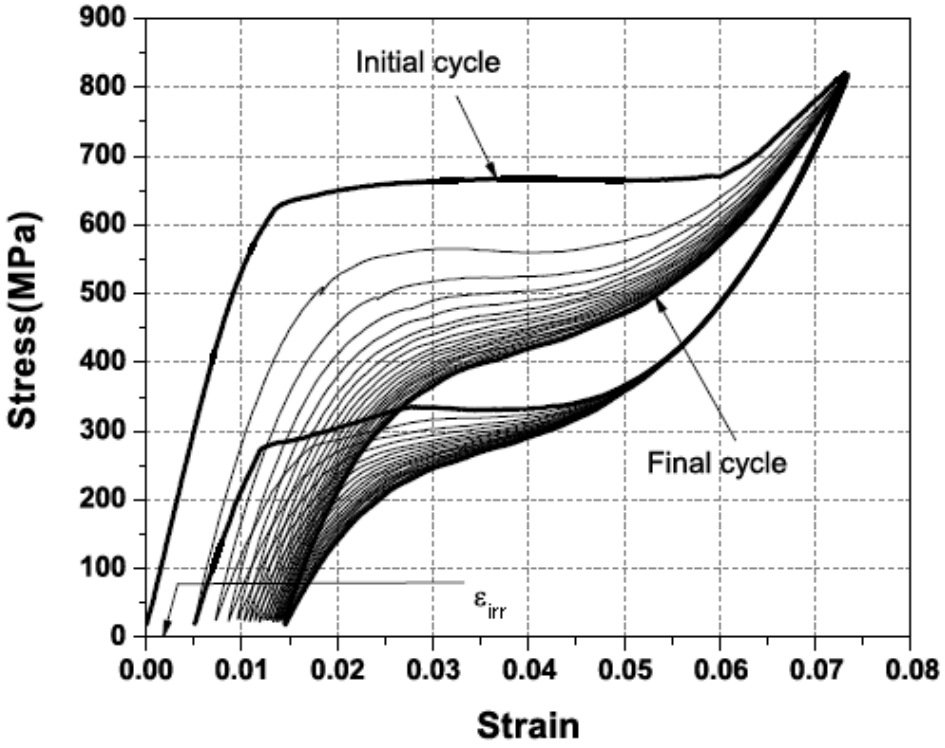

Figure 2.10: Illustration of the cyclic superelastic response of a shape memory alloy. Compared to the first cycle, the transformation stress and stress hysteresis are reduced, but irrecoverable strain has accumulated [123].

3. RESEARCH OBJECTIVES

The chief objective of this dissertation work is to engineer a non-porous, biocompatible shape memory alloy with ultra-low effective modulus based on the Ti-Nb SMA system. This involves several tasks divided into three categories: establishing the biocompatibility and corrosion resistance of the alloy; characterize and improve the shape memory, superelastic, and mechanical response (including fatigue crack growth) of the alloy; characterize the low-cycle functional fatigue of the alloy and using it to achieve the ultra-low effective modulus. These tasks can be further classified into the following topics:

1) Increase the resistance of plastic deformation of the Ti-Nb SMAs through the equal channel angular extrusion (ECAE) technique and post-extrusion heat treatments.
2) Characterize the shape memory and superelastic properties of solution-treated and processed Ti-Nb SMAs. Determine the effect of ECAE and heat treatment on the microstructure of the alloys, and how the changes in microstructure impact the properties.
3) Characterize the effect of superelastic cycling on the Ti-Nb SMAs, and utilize cycling to achieve an effective modulus comparable to that of human bone.
4) Describe the recovery phenomenon that occurs in cycled Ti-Nb SMAs whereby the effect of superelastic cycling is reversed when specimen is allowed to rest in a stress-free condition at room temperature.
5) Characterize the effect of ternary zirconium addition on the shape memory and superelastic properties.
6) Characterize the fatigue crack growth response of the Ti-Nb SMAs.
7) Characterize the biocompatibility and corrosion resistance of the Ti-Nb SMAs.

4. EXPERIMENTAL METHODS

4.1. Alloy selection and preparation

Two Ti-Nb based shape memory alloy compositions were used for the studies in this dissertation: a binary $Ti_{74}N_{26}$ (at.%) and a ternary $Ti_{72}Nb_{22}Zr_6$ (at.%) alloy. These compositions were chosen based on results reported in literature [Kim 90, 92] to show good superelastic behavior at room temperature after appropriate thermo-mechanical treatments. The alloys were fabricated from elements of 99.99% purity by vacuum arc melting in rectangular billets of 0.75'' x 0.75'' x 5'' in dimension. The billets were then solution treated at 1000 °C for 1 hour and water quenched.

The compositions of the solution-treated alloys were checked with wave-disperse spectroscopy (WDS) on a CAMECA electron microprobe. The instrument was calibrated against pure titanium, niobium, and zirconium standards. The surface of the specimen were mechanically ground with silicon carbide abrasive paper, polished with a diamond suspension, and finished with a final step with 0.05 μm colloidal silica. At least 6 measurements were taken over the surface of each polished sample. The measured compositions are reasonably close to the desired composition, as shown in Table 4.1. The standard deviation of the measurements is relatively small, which suggest that the specimens are homogeneous compositionally.

Phase homogeneity of the specimens was checked with X-ray diffraction (XRD) of the solution-treated specimens after similar polishing procedures as used for WDS investigations. Specimens were examined with a Bruker D8 Discover XRD system equipped with a conventional Bragg-Bretano diffractometer operating with Cu-kα radiation at 40 kV. Scans were conducted in the 2θ range of 20°-80° with a step size of 0.01° and a scan time of up to 3 seconds per step. A sample XRD pattern is shown in Figure 4.1, and illustrates the presence of the bcc austenite and absence of any other phases.

Table 4.1: Composition of the $Ti_{74}Nb_{26}$ and $Ti_{72}Nb_{22}Zr_6$ SMAs as determined by WDS.

		Nominal	Measured	Standard Deviation
Binary	Ti	74	73.92	0.29
	Nb	26	26.08	0.29
Ternary	Ti	72	71.68	0.51
	Nb	22	22.01	0.57
	Zr	6	6.31	0.09

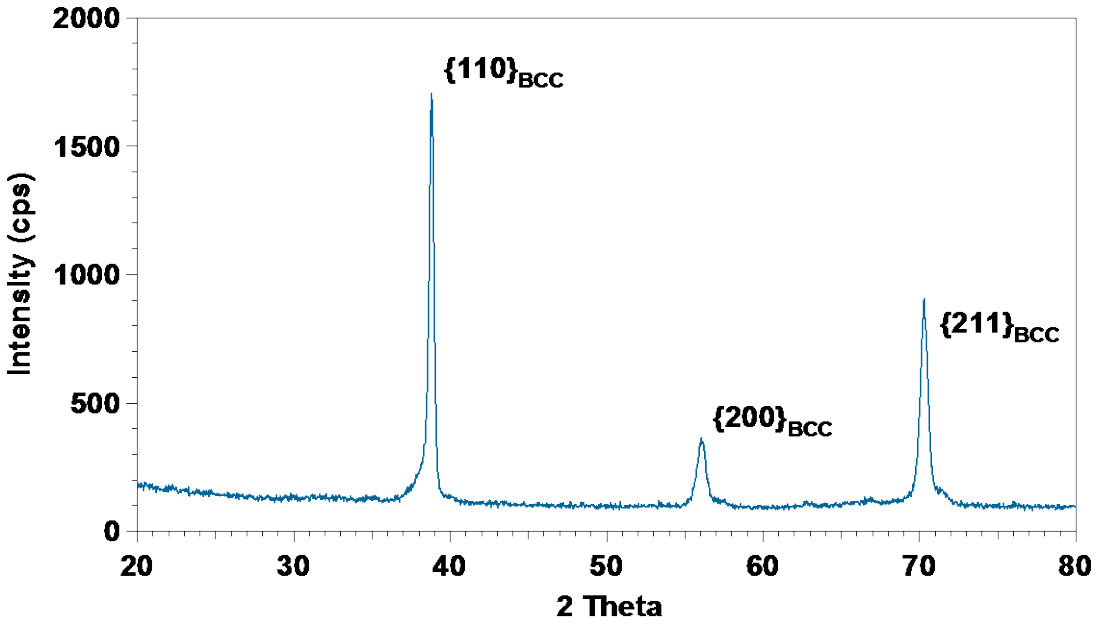

Figure 4.1: X-ray diffraction image of a $Ti_{74}Nb_{26}$ shape memory alloy in the austenite state.

4.2 Equal Channel Angular Extrusion

Equal channel angular extrusion of the Ti-Nb billets were carried out with a 250-ton MTS hydraulic press with a custom extrusion tool constructed from Inconel 718, a precipitation hardened nickel-chromium alloy. The tool is an L-shaped channel with a sharp 90° angle with a square cross-section of 0.75". Because of the low strength and superb ductility of the Ti-Nb and Ti-Nb-Zr alloys in the solution-treated state, the extrusion could be easily carried out at room temperature. An initial extrusion at the rate of 0.1 in s^{-1} was found to be too fast and caused the fracture of the billet, but decreasing the extrusion rate to 0.01 in s^{-1} allowed the extrusions to proceed without incident. In all extrusion with a rate of 0.01 in s^{-1}, the extrusion load stayed well below the load limit of the press, and no cracks or shear localization were observed in any of the billets. The extrusions were carried out without the application of back pressure.

The binary $Ti_{74}Nb_{26}$ alloy was processed using two different ECAE routes: route 1A (one extrusion pass) at room temperature, and route $4B_c$ (four extrusion passes with clockwise 90° rotation of the billet about the extrusion axis before passes 2 and 4, and a counterclockwise 90° rotation of the billet about the extrusion axis before pass 3) at room temperature. The ternary $Ti_{72}Nb_{22}Zr_6$ alloy was extruded only via route 1A at room temperature.

These extrusion routes were chosen to study various effects of extrusion on the microstructure and texture of the alloy. Route 1A at room temperature is a direct comparison of the simplest ECAE process with the solution treated state. Route $4B_c$ at room temperature is an attempt to further reduce the grain size of extruded material and enhance the strength of extrusion texture.

4.3 Post-extrusion heat treatments

It was found that shape memory and superelastic behavior did not appear in specimens extruded at room temperature without further heat treatments. This is likely due to the high dislocation density and the nanocrystalline grain sizes of the

as-processed billets, which limited the ability of martensite to propagate and grow, and thus suppressing phase transformation. It was then necessary to introduce a short intermediate temperature annealing process to allow some microstructure recovery. Various heat treatments with temperatures between 400 °C to 800 °C and durations between 5 minutes to 1 hour were carried out on the as-extruded specimens, and all specimens were water-quenched. In many cases, these heat treatments do not produce a material with useful shape memory properties, and these were not pursued further. Table 4.2 summarizes all the post-extrusion annealing heat treatments studied that showed promising shape memory properties.

Based on the work by Kim *et al.* [92], the strength of specimens could be further increased by a low-temperature heat treatment designed to generate hexagonal ω precipitates within the matrix. This has been shown to improve the superelastic response of the alloy. Following this, we applied an additional precipitation heat treatment at 300 °C for 1 hour on the annealed specimens A610 and C610.

Table 4.2: Selected combinations of ECAE routes and post-extrusion heat treatments, as well as the shorthand notation of these processing routes used in this work.

Mechanical Process	Heat Treatment	Notation
ECAE 1A	600°C 10 Minutes	A610
	600°C 1 Hour	A61H
ECAE 4Bc	600°C 10 Minutes	C610
	600°C 5 Minutes	C65
	500°C 10 Minutes	C510

4.4 Determination of transformation temperatures

Differential Scanning Calorimetry (DSC), the conventional method for determining the transformation temperatures of shape memory alloys cannot be applied to Ti-Nb shape memory alloys as no peaks are visible as shown in Figure 4.2. This is believed to be caused by a small transformation enthalpy (ΔH), and a large difference between M_f and M_s.

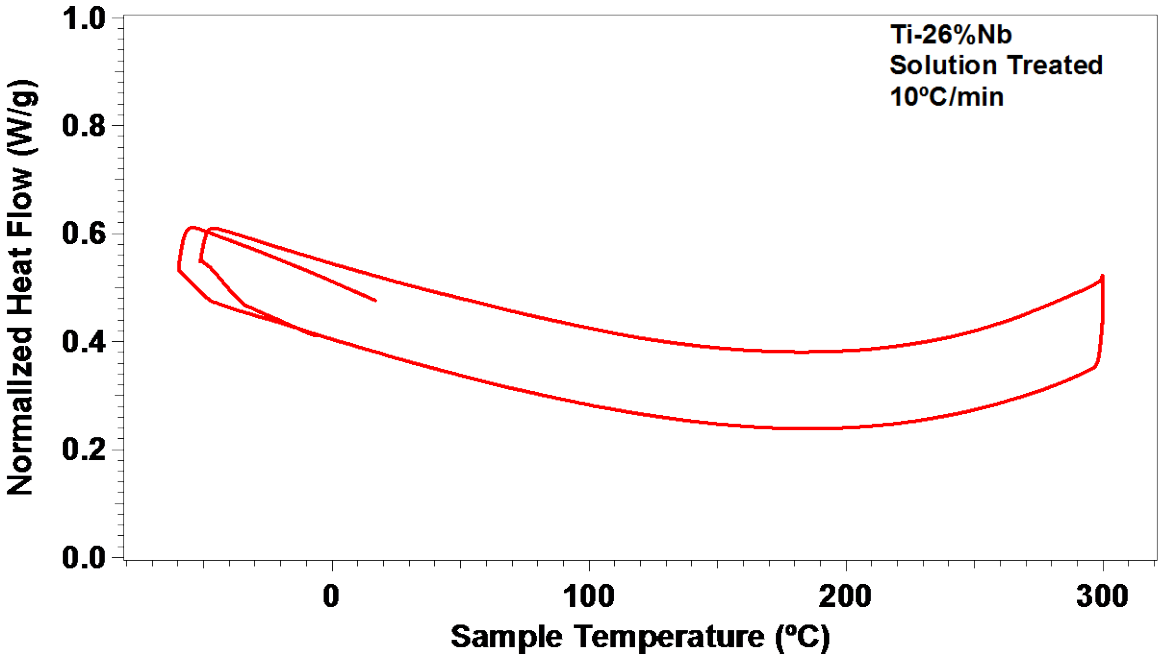

Figure 4.2: Differential scanning calorimetry data for the solution treated $Ti_{74}Nb_{26}$ shape memory alloy. No peaks corresponding to transformation are observed, although it is shown later that transformation does indeed occur in this material.

Instead, we evaluate the transformation temperatures of the alloy indirectly through constant-stress heating cooling experiments demonstrated in Figure 4.3. A series of such heating-cooling experiments at various stress levels are usually

conducted as shown in Figure 4.4a. The analysis of the strain vs. temperature responses from these experiments and determination of transformation temperatures at each stress level lead to the construction of the stress-temperature phase diagrams in Figure 4.4b. Using the stress-temperature relationships in Figure 4.4b, transformation temperatures at stress-free condition can be extrapolated. For this purpose, a tensile sample of the material of interest in loaded to a constant stress level, and cycled thermally through the range of transformation temperatures. When the stress level is high enough such that detwinned martensite could be obtained, it is possible to graphically determine the transformation temperatures. By repeating this procedure at several different stress level, one can find the slope $d\sigma/dT$, and extrapolate it to $\sigma = 0$ where the temperature can be taken as the stress-free transformation temperatures. The Clausius-Clapeyron relationship is mathematically stated as follows (equation 4-1):

$$\frac{d\sigma}{dT} = \frac{dS}{\varepsilon_0} \qquad \text{(equation 4-1)}$$

Where dS is the entropy of transformation and ε_0 is the transformation strain between austenite and martensite.

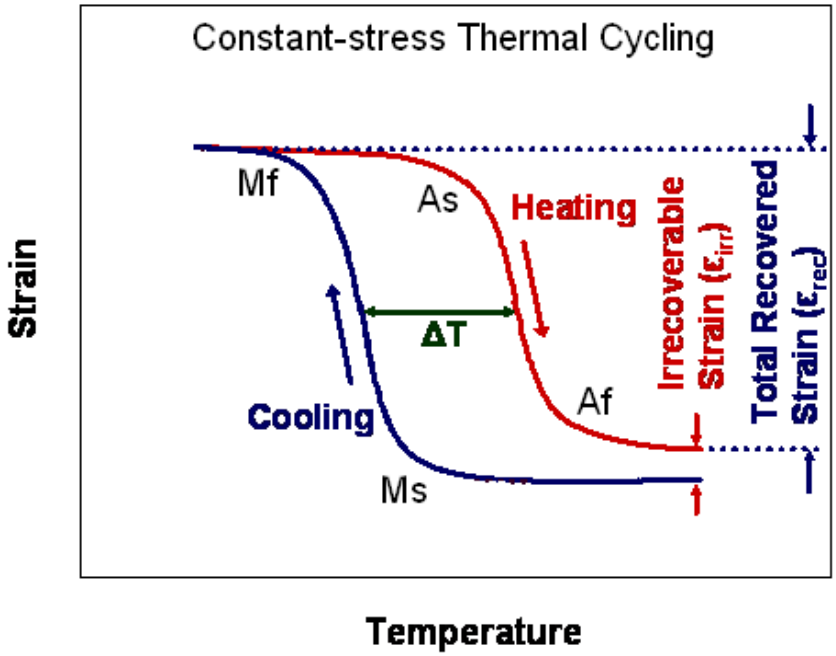

Figure 4.3: a) Representative strain vs. temperature response of an SMA in constant-stress thermal cycling experiments. Important shape memory characteristics are also shown, such as transformation temperatures, irrecoverable strain (ε_{irr}), total recovered strain (ε_{rec}), and transformation thermal hysteresis (σT).

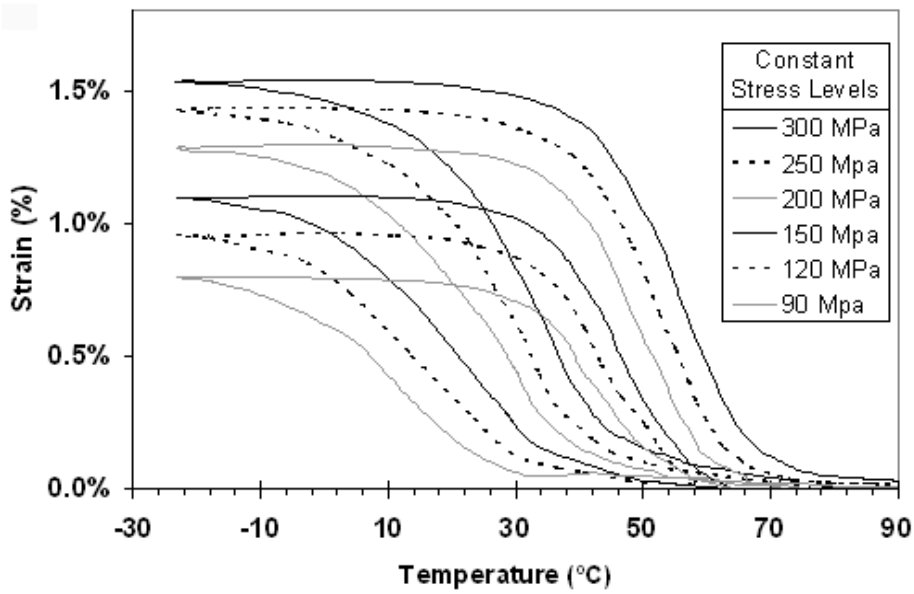

(a)

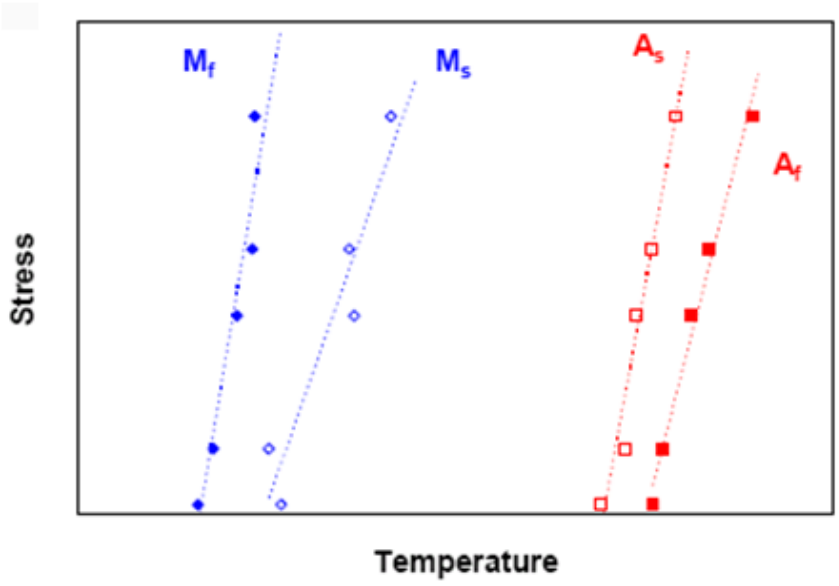

(b)

Figure 4.4: Construction of stress vs. temperature phase diagram (b) for an SMA using constant stress thermal cycling experiments (a). The lines for each transformation temperature in (b) can be extrapolated down to zero stress to determine the stress-free transformation temperatures [123].

4.5 Determination of shape memory properties

Constant-stress thermal cycling experiments shown in Figure 4.3 and Figure 4.4 are also used to determine the evolution of recoverable strain (ε_{rec}), irrecoverable strain (ε_{irr}), and temperature hysteresis (ΔT). Dog-shaped tension specimens Figure 4.5 with a gage cross-section dimension of 3 mm x 1 mm were heated to approximately 100 °C under no stress. The stress on the specimen was then increased at intervals of 50 MPa or 25 MPa. After each increase in load, the specimen is cooled to approximate -60 °C, and then heated back up to 100 °C before the next load increase. This way, the stress is always applied in the austenite state to avoid martensite reorientation during loading. Strain was measured by an extensometer attached directly to the gage section of the tensile specimen.

For all specimens where transformation strain was observed at multiple stress levels, the transformation strain and cumulative irrecoverable strain as a function of applied stress level generates a plot similar to Figure 4.6. In this figure, ε_{rec} increases initially with increasing stress, but eventually reaches a maximum before decreasing rapidly. At the same time, ε_{irr} is not usually detected up to a certain applied stress level, and then increases monotonically with increasing stress.

This set of experiments was conducted on specimens of every processing and heat treatment conditions included the solution-treated sample and as-extruded specimens. Transformation strain is not observed for as-extruded samples without further heat treatment, and thus their transformation temperature could not be determined. Precipitation-hardened specimens do not show transformation strain until a very high stress level (over 400 MPa) was applied, but generally fracture during the heating-cooling cycles of the next stress interval. Nevertheless, they do show good superelastic response.

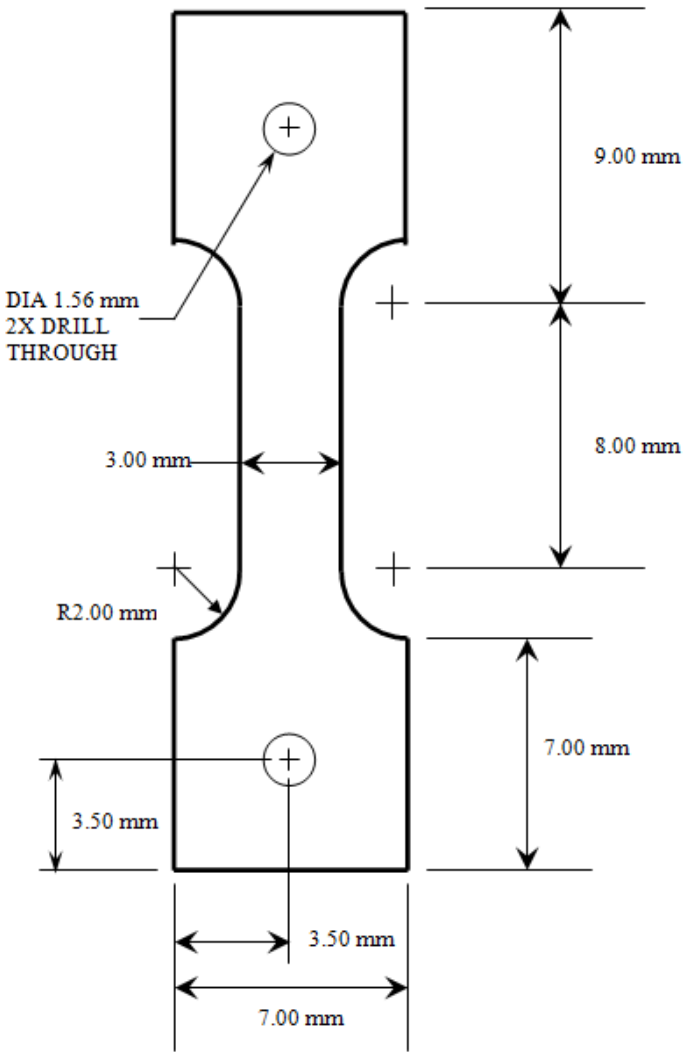

Figure 4.5: Dimensions of the tension specimen used in all tensile experiments in this work. These specimens are generally 1 mm thick.

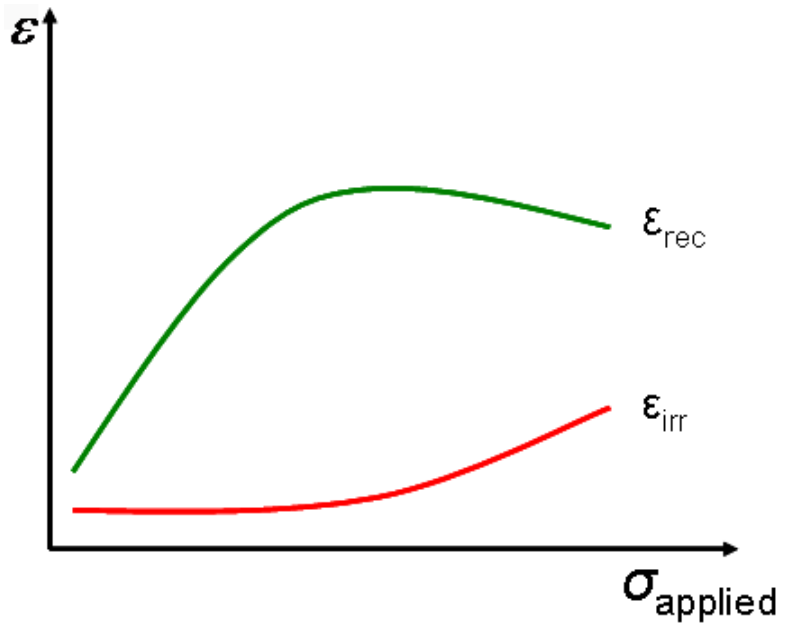

Figure 4.6: ε_{rec} and ε_{irr} as a function of applied stress. The curves are constructed using the data extracted from constant-stress thermal cycling experiments in Figure 4.4.

4.6 Characterization of superelastic response

4.6.1. Incremental superelastic response

Superelastic properties can be evaluated from the loading-unloading experiments shown in Figure 4.7. Tension specimens, identical to those used for the heating cooling experiments described the previous section (see Figure 4.5) were used. Specimens were loaded at a constant temperature to a certain strain levels, unloaded, and then loaded again to a higher level of strain. This process continues until significant irrecoverable strain is detected after unloading, which generally occurred at 2.5% to 3% applied strain levels. All superelastic experiments were conducted under strain controlled mode at a strain rate of $5x10^{-4}$

s^{-1}, and strain was measured with the same extensometer used for the constant stress heating cooling experiments.

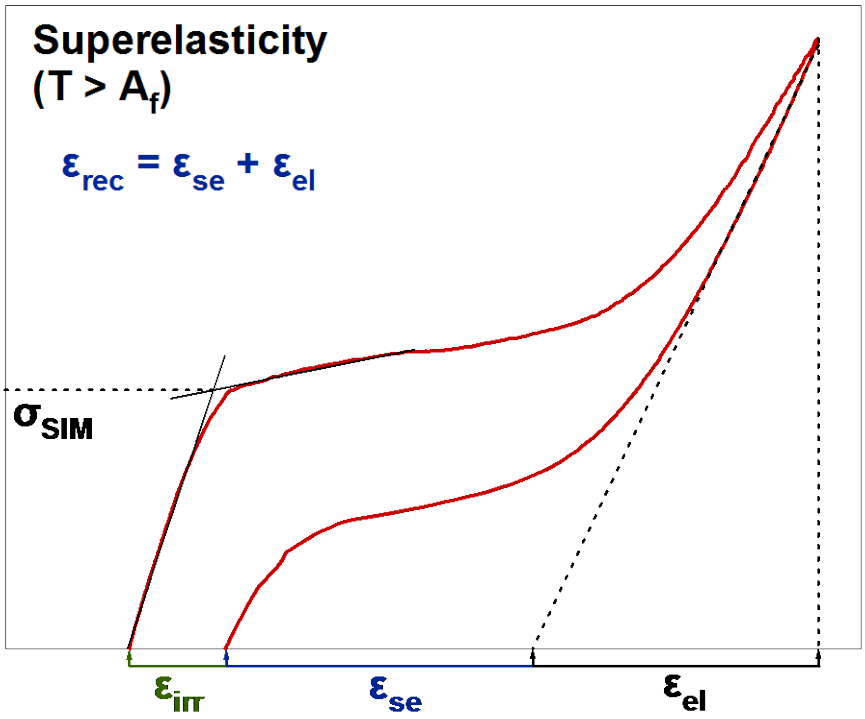

Figure 4.7: Superelastic properties from a typical experiment. σ_{SIM} denotes the critical stress for stress-induced martensitic transformation; ε_{irr},, ε_{se}, and ε_{el} represent irrecoverable strain, superelastic shape strain, and elastic recoverable strain, respectively. Total strain recovery (ε_{rec}) in superelasticity is the sum of ε_{se} and ε_{el}.

The temperature at which superelastic experiments are conducted relative to the A_f temperature is important for the superelastic properties. The larger the difference between the test temperature and A_f, the greater the driving force in terms of stress will be required to initiate stress-induced transformation which

results in inferior superelasticity. Above a certain temperature, called M_d, stress induced martensitic transformation becomes impossible because plastic deformation will occur at a lower stress level. In this experiment, the superelastic responses of the alloys were generally evaluated at room temperature. Although the compositions of the specimens are the same, their transformation temperatures shift due to the processing and heat treatment procedures. Therefore, the difference between the experiment temperature and A_f of each sample is not necessarily the same in superelastic experiments. However, since applications involving superelasticity are generally designed to operate at a fixed temperature regardless of the transformation temperature of the alloy, the important objective is to engineering the alloy to perform at a pre-determined temperature, not the other way around. Nevertheless, a small number of superelastic experiments were carried out at other temperatures to evaluate the temperature-dependence of superelastic behavior.

Important superelastic properties, shown in Figure 4.7, are primarily irrecoverable strain (ε_{irr}), recoverable strain (ε_{rec}), and critical stress for stress-induced transformation (σ_{SIM}). Recoverable strain includes elastic recovery and recoverable shape change from the stress-induced martensitic transformation and possibly also martensite detwinning. With increasing applied strain, both ε_{rec} and ε_{irr} tend to increase. Similar to the shape memory behavior, ε_{rec} reaches a maximum at some strain level while ε_{irr} increases monotonically with applied strain.

4.6.2. Cyclic superelastic response and low-cycle fatigue

Several specimens were also subjected to a constant-strain, constant-temperature cyclic superelastic experiments. Here, the specimens are loaded to 1% or 1.5% strain 1000 or 1500 times at room temperature to evaluate the low-cycle functional fatigue properties of the alloys. The transformation stress (σ_{SIM}), stress

hysteresis ($\Delta\sigma$), and irrecoverable strain (ε_{irr}) as a function of number of superelastic cycles are summarized.

4.7 Microstructure and crystallography texture

To evaluate the microstructural features of the specimens and the effect of processing conditions on the microstructure, optical microscopy and transmission electron microscopy were conducted on various specimens. Specimen for optical microscopy and crystallographic texture measurement were mechanically grinded and polished to 0.05 micron colloidal silica and etched with a solution of (by volume) 90% H_2O, 7% HNO_3, and 3% HF. Optical micrographs were acquired with a Keyence optical microscope. Transmission electron microscopy (TEM) samples were mechanically ground down to a thickness of less than 100 microns, and electropolished using a conventional twin-jet electropolisher in a (by volume) 60% methanol, 34% butanol, and 6% perchloric acid solution at -20 °C. TEM images were taken using a Philips CM200 electron microscope operating at 200kV.

To evaluate the structure and volume fraction of martensite and austenite, several x-ray diffraction measurements were conducted with a Bruker AXS Discover D8 X-ray diffraction system operating with Cu-Kα radiation at 40 keV and a wavelength of 1.5406 Å. Simple 2-θ scans with a stepsize of 0.01° and a scan time of up to 3 seconds per step were conducted to determine the precise lattice parameters of the austenite.

Crystallographic texture measurements were conducted with a fitted Eulerian Cradle assembly within the XRD system (Figure 4.8). A flat specimens is polished and mounted to the center of the stage, which then tilts and rotates at fixed 2θ values that corresponds to the locations for peaks observed from a simple 2θ scan. The raw file containing the intensity of various peaks as a function of tilt and rotation angles was then converted to pole figures and inverse pole figures with the preferred orientation package – Los Alamos (popLA) software.

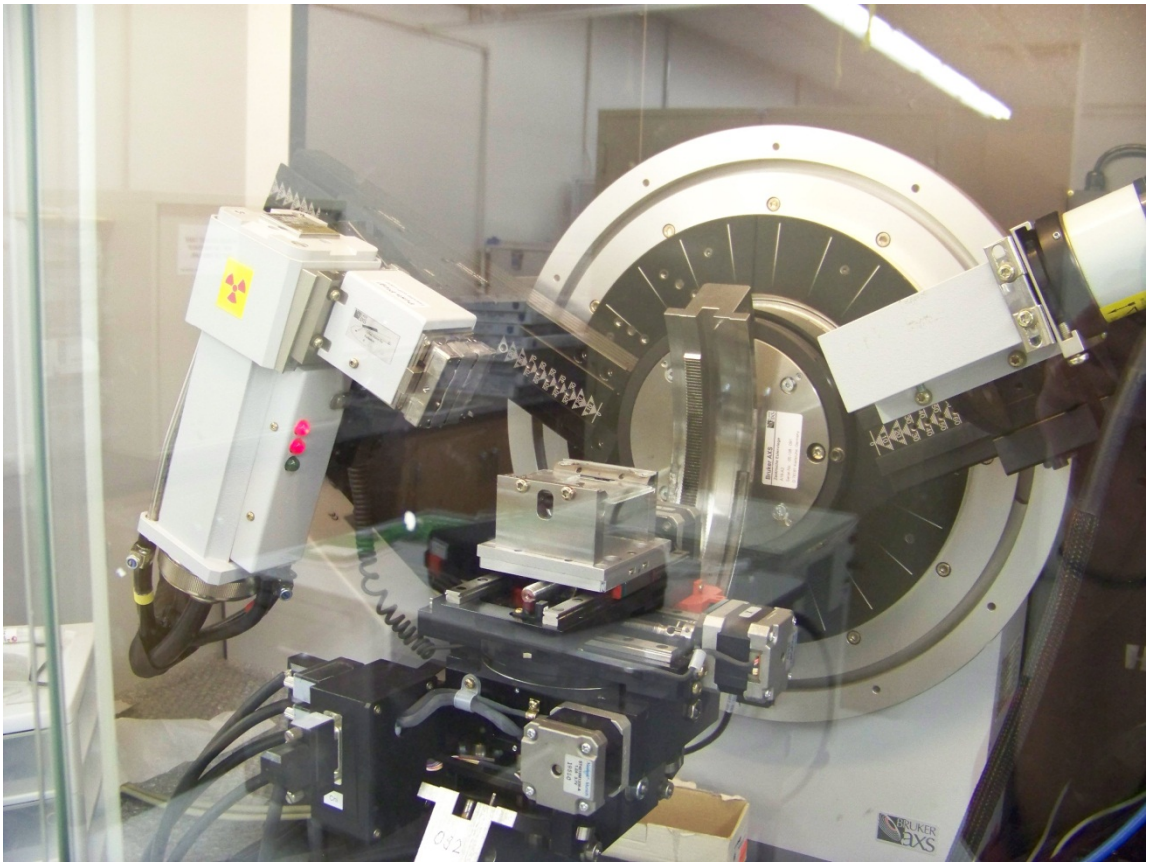

Figure 4.8: the Eulerian Cradle system used for texture measurement.

In-situ XRD experiments under stress were carried out with a Deben Microtest Stress Stage (Figure 4.9). Tension specimens with the geometry shown in Figure 4-5 were mounted to the stage and attached to the XRD assembly, and 2θ scans were taken at various applied stress levels at room temperature to study the evolution of stress-induced martensitic transformation, including the intensity of martensite peaks and austenite peaks and the shifts in austenite peaks under applied stress.

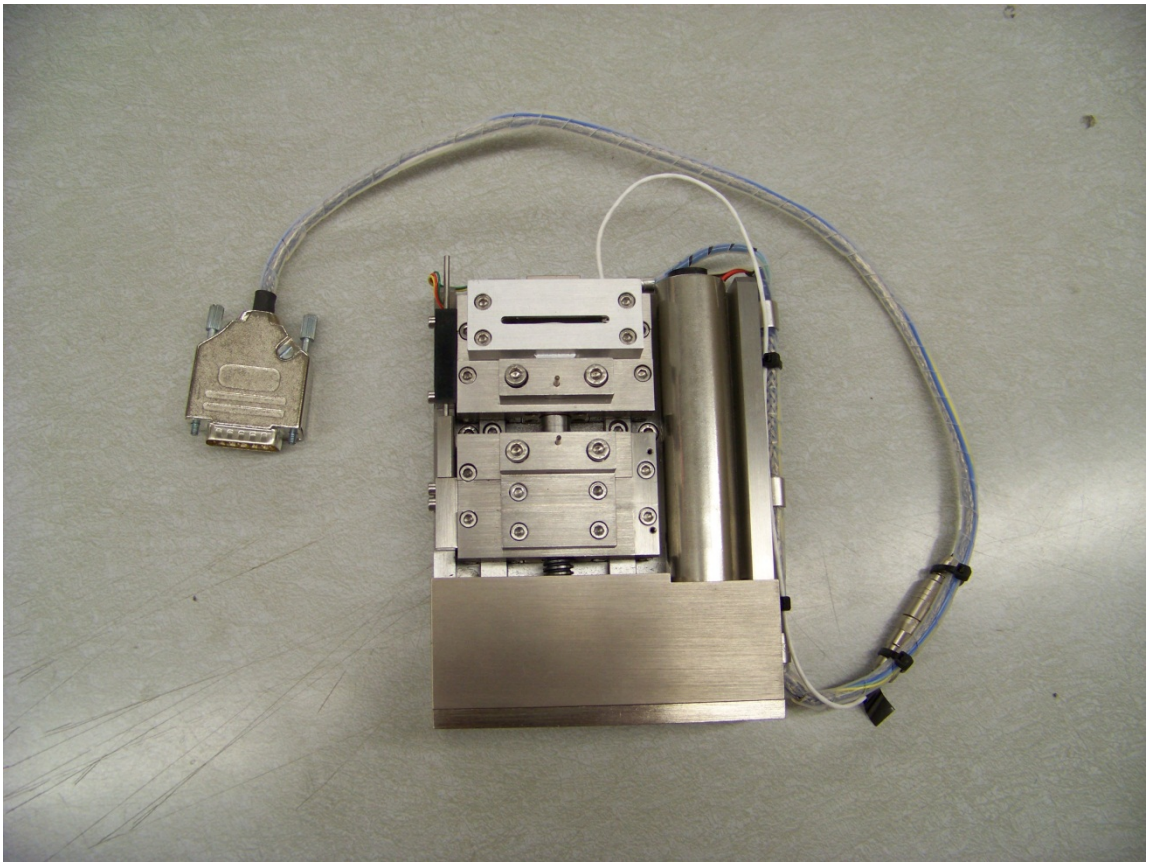

Figure 4.9: the Deben stress stage used for in-situ XRD experiments.

4.8 Cytotoxicity, ion leaching, and corrosion resistance experiments

In order to evaluate the biocompatibility and corrosion resistance of the Ti-Nb shape memory alloy, cytotoxicity, ion release, and potentiodynamic corrosion resistance experiments were conducted. The cytotoxicity and ion release experiments were primarily performed by our collaborators in the project. Please refer to a separate dissertation [108] for a detailed discussion of experimental methods and results on this part of the work. The focus of the present work will be on the mechanical properties of the material, and thus will not delve into these issues. However, we will discuss some of the results of these experiments in Section 9.

Potentiodynamic tests were performed at 37 ºC on $Ni_{50.8}Ti_{49.2}$, $Ti_{74}Nb_{26}$, and commercial pure Ti samples submerged in 1M NaCl or in Hank's Balanced Salt Solution (HBSS; 8 g NaCl, 0.4 g KCl, 0.14 g $CaCl_2$, 0.06 g $MgSO_4$, 0.06 g NaH_2PO_4, 0.35 g $NaHCO_3$, 1 g glucose, 0.6 g KH_2PO_4, 0.1 g $MgCl_2$ per liter de-ionized water). An Ag/AgCl electrode was used as a reference with a Pt counter electrode. The potentiodynamic measurements were performed using a conventional Bank PGS 95 potentiostat after 5 min immersion in the appropriate solution. Each potential scan was conducted from -1000 mV to at least 1000 mV at a 4 mV/s scan rate. Two specimens per sample type were analyzed per immersion solution.

Secondary ion mass spectrometry (SIMS) depth profile studies were conducted on the Ni-Ti and Ti-Nb specimens used in the cytotoxicity/ion release experiments in order to evaluate whether cell death and ion leachant measures were correlated with the alterations in alloy surface composition. One side of each cytotoxicity specimen was kept in the "as-tested" condition. The other side, which was mechanically ground to remove the surface layer and re-polished, served as a control. After rinsing with acetone and ethanol, composition depth profiling was carried out under vacuum in a Cameca IMS 4f Ion Microprobe with an oxygen probe beam operating at 150 nA and a nominal sputtering rate of 1 nm/s. Ti and Ni signals were measured for the Ni-Ti specimens, and Ti and Nb signals were determined for the TiNb samples. Given the presence of calcium and phosphate in the cell culture media and the known association of calcium phosphate with TiO_2 layers [124], the signal intensities of calcium and phosphorus were also recorded for each sample. Various signal ratios were then calculated with sputtering time. For instance, the ratio of the measured Nb and Ti signals was determined for both the freshly polished and as-tested surfaces of each TiNb sample. The associated ratio was then calculated for each Ti-Nb sample. As anticipated, the ratio between the titanium composition of the as-polished and as-tested in both Ti-Nb and Ni-Ti reached a steady value (arbitrarily set to 1) at longer sputtering times, consistent

with the surface oxide layers having been passed and more uniform internal compositions having been reached.

4.9 Fatigue crack growth

Fatigue crack growth experiment was carried out to evaluate the fatigue resistance and construct the Paris Law relationship of the alloy. Disk-shaped compact tension (CT) specimens were electro-discharge machined from the bars such that the pre-notch was aligned in the radial direction, mechanically ground through 1200-grit paper to remove the machining and annealing oxides, and polished for a consistent finish. Fatigue crack propagation tests were carried out on an electro servo-hydraulic mechanical test system in general accordance with ASTM Standard E 647 [125], at a positive load ratio, R =Kmin/Kmax = 0.1, at 50 Hz (sine wave) frequency in ambient air, a 1 M NaCl solution, and in a Hank's Balanced Salt Solution (HBSS; 8 g NaCl, 0.4 g KCl, 0.14 g $CaCl_2$, 0.06 g $MgSO_4$, 0.06 g NaH_2PO_4, 0.35 g $NaHCO_3$, 1 g glucose, 0.6 g KH_2PO_4, 0.1 g $MgCl_2$ per liter de-ionized water). Crack lengths were continuously monitored via a back-face strain gauge on each sample. Most tests were conducted in load control mode to generate an increasing growth rate and stress intensity range with crack advance. Fatigue threshold K_{th} values were operationally defined as the stress intensity range at which growth rates did not exceed 10−10 m/cycle [125].

5. EFFECT OF THERMO-MECHANICAL PROCESSING

It has been reported that the strength of the $Ti_{74}Nb_{26}$ SMA is very low in the solution treated state [89, 92], and the lack of strength results in the appearance of large irrecoverable strains during shape memory and superelastic cycles. Furthermore, plasticity often takes place before the material could fully transform from austenite to martensite, thus decreasing the magnitude of transformation strain as well. Therefore, we seek to improve the mechanical strength of the $Ti_{74}Nb_{24}$ SMA through the combination of equal channel angular extrusion (ECAE) and post-extrusion heat treatments. Through these steps, we hope to reduce irrecoverable strain of the material, while simultaneously increasing its transformation strain.

5.1 Microstructure

Transmission electron microscopy (TEM) and selected area diffraction (SAD) patterns (Figure 5.1) for the A610 and C613 specimens are shown in Figures 5.1a and 5.1b, respectively. The microstructure of A610, shown in Figure 5.1a, has recovered sufficiently to form grains ~20 μm in size and clearly discernible dislocation networks. On the other hand, grain sizes in C610 are the range of 200 nm, and large dislocation density remains (Figure 5.1b). Grains in C613 are also equiaxed, and surrounded by very high dislocation densities. In contrast, the grain size of the solution treated specimen (Figure 5.2) is much larger at 300-400 μm.

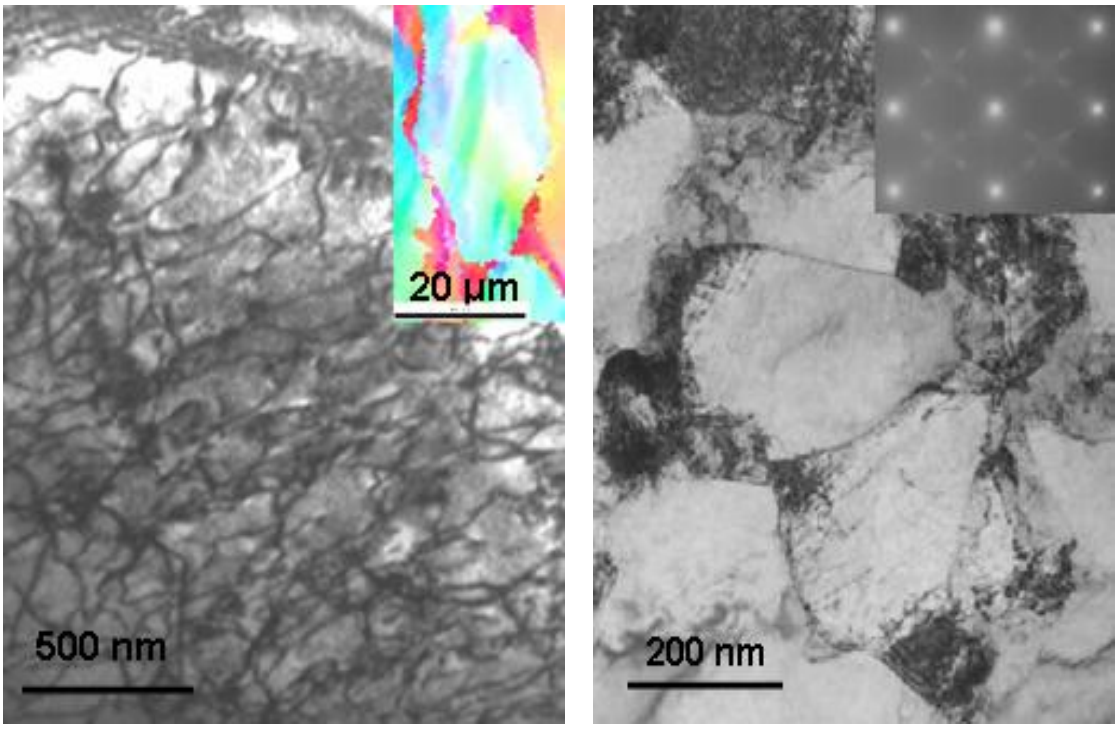

(a) (b)

Figure 5.1: Bright-field TEM images of (a) A610 and (b) C613 samples. The EBSD map in the inset of (a) reveals a grain size of about 20 microns. The sample C613 contains ω precipitates as shown in the SAD inset, which demonstrates extra spots between the main reflections from the cubic matrix.

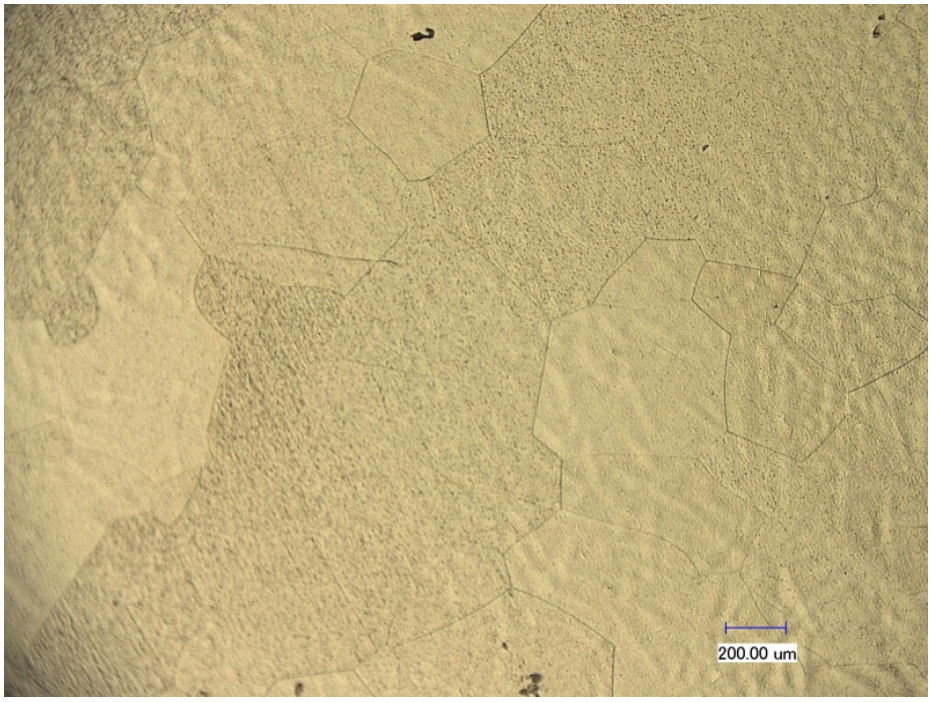

Figure 5.2: Optical microscopy image of the solution-treated $Ti_{74}Nb_{26}$ specimen, with grain size 300-500 μm.

5.2 Crystallographic texture

In shape memory alloys, transformation strain levels are orientation-dependent and are therefore governed by crystallographic texture in polycrystals. Crystallographic texture of all specimens was measured through XRD in order to determine their effects on the transformation strain levels. In particular, the pole figure and inverse pole figure of the A610 case was also measured with electron back-scatter diffraction (EBSD) to double check the results. The pole figure and inverse pole figures of A610 from EBSD is shown in Figure 5.3 with the extrusion direction parallel labeled as the <010> axis, while the inverse pole figure representations of texture from X-ray diffraction (XRD) are shown in Figure 5.4 for all specimens. The inverse pole figure of the extrusion direction for A610 measured by two different methods yields a good match. From the energy

minimization theory [126], we have calculated tensile theoretical transformation strain for the $Ti_{74}Nb_{26}$ SMA as a function of orientation, shown in Figure 5.5.

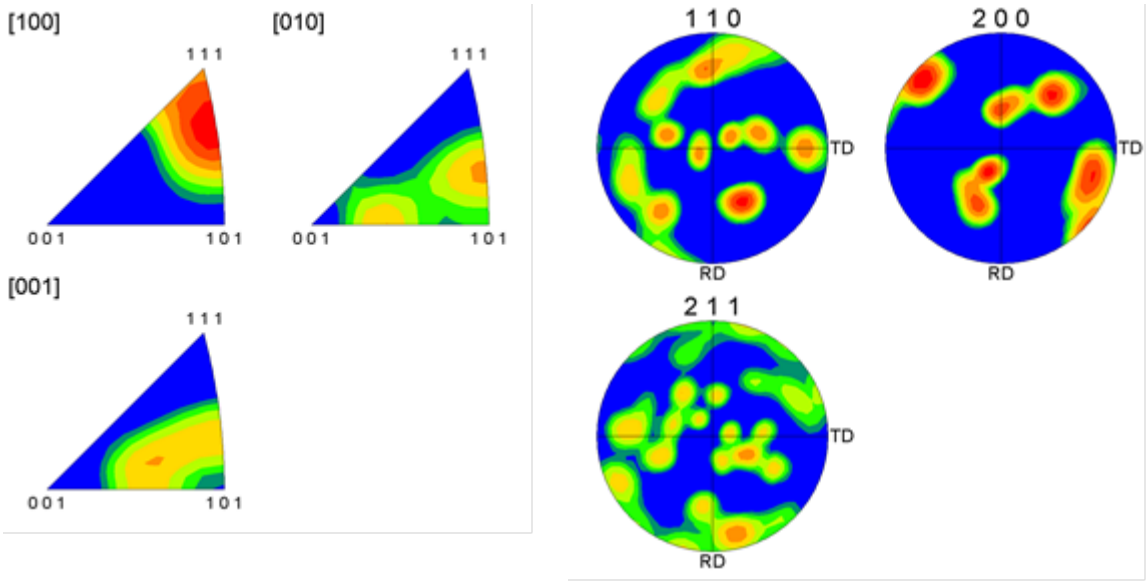

(a) (b)

Figure 5.3: Experimental a) inverse pole figure and b) pole figure of the $Ti_{74}Nb_{26}$ shape memory alloy for the A610 specimen as determined by electron back-scatter diffraction (EBSD). The [010] direction is parallel to the transverse direction.

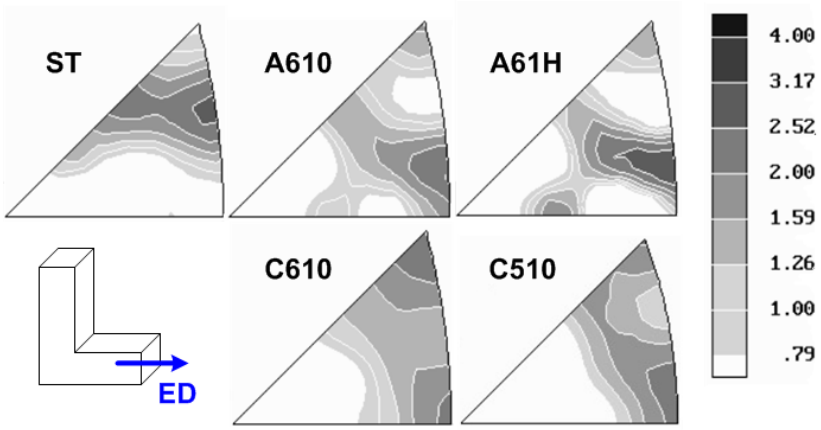

Figure 5.4: Experimental inverse pole figure of the $Ti_{74}Nb_{26}$ shape memory alloy for various processing conditions in the extrusion (tensile) direction as determined by X-ray diffraction. The inverse pole figure of A610 is very similar to that obtained from EBSD in Figure 5.3.

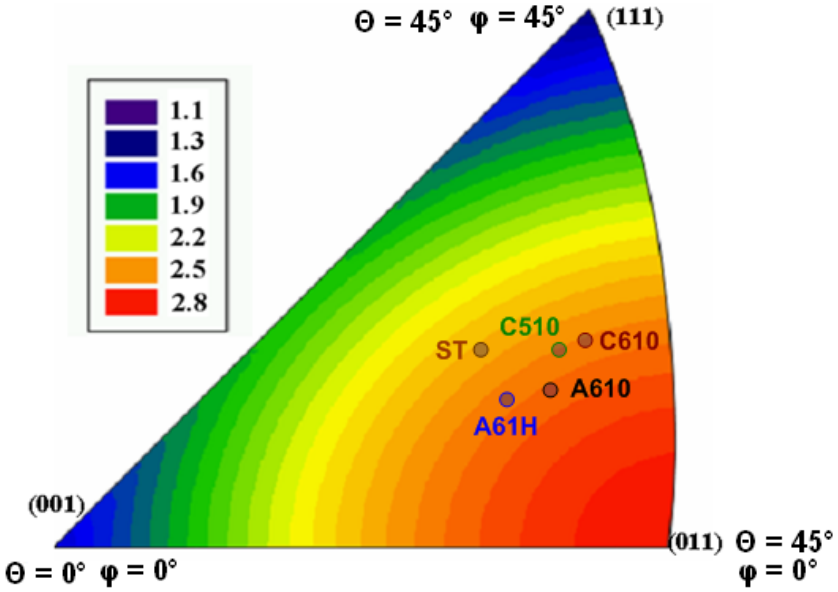

Figure 5.5. Theoretical transformation strain as a function of orientation calculated via the Energy Minimization method. The average orientation of various specimens is shown on the stereographic triangle.

We then performed texture measurements and determined a theoretical transformation strain (ε_{tr}) level for each polycrystalline sample using a weighted average orientation method. Following the Sachs condition, we assumed that grains within the material act as uncorrelated single crystals, and no geometric compatibility was enforced at the grain boundaries. Under stress, each grain achieves its maximum possible ε_{tr} allowed by its orientation with respect to the loading direction. From the measured texture of the polycrystalline sample, an "average orientation" of all grains was found by performing a weighted average based on intensity at various Euler angle pairs. The theoretical ε_{tr} of this average orientation was then taken as the theoretical ε_{tr} of the sample. This method is equivalent to orientation averaging method used previously by other authors [127, 128].

Average orientation was calculated using inverse pole figure data of the extrusion direction produced from Preferred Orientation Package – Los Alamos (popLA). The Euler angles were defined by the Kocks convention, and each pair of (θ, φ) angles represented one grain while the intensity of that angle pair represented the number of grains with this orientation. A weighted average of all (θ, φ) angle pairs was then taken. Because of cubic symmetry of the material, only the range of θ = 0 - 45° and φ = 0 - 45° was required. The location of the average orientation can be plotted on a stereographic inverse triangle and then matched with the theoretical calculation of the property of interest (in this case ε_{tr}) of that orientation (Figure 5.5). The Sachs condition means the polycrystalline theoretical ε_{tr} found by this method is essentially an "upper bound" value. Experimentally achievable strain will be smaller due to geometric constraint at the grain boundaries [127, 128]. However, since the purpose for the calculation is not to find the exact ε_{tr} of a specimen, but rather to compare among various specimens. Assuming the contribution of grain boundary constraint on ε_{tr} is comparable among all specimens, the method is expected to satisfy its purpose. This is likely a reasonable assumption due to the relative weak texture of all specimens measured.

As evident from Figure 5.5, the variation of polycrystalline theoretical ε_{tr} among all specimens is small, ranging from 2.4% strain for the solution treated specimen to 2.6% for A610. This means the major differences in experimentally observed ε_{tr} among specimens is likely to be mainly a function of microstructure, not texture.

5.3. Strength and ductility

The direct effect of ECAE on the room temperature mechanical properties of $Ti_{74}Nb_{26}$ SMA is illustrated in Figure 5.6. It is clear that ECAE significantly increased the yield strength of alloy. Yield strength increased from 300 MPa in the solution treated condition to over 750 MPa in each of the ECAE specimens. On the other hand, it is interesting that the ECAE processing route does not appear to significantly affect the yield strength. Tensile elongation to failure decreased from 24% in solution treated state to about 8% in as-processed 1A at room temperature, and 9.5% in as-processed 4Bc at room temperature. It is not clear why further extrusion passes after route 1A no longer increase the yield strength. Likewise, neither solution treated nor the as-extruded specimens show superelasticity at room temperature.

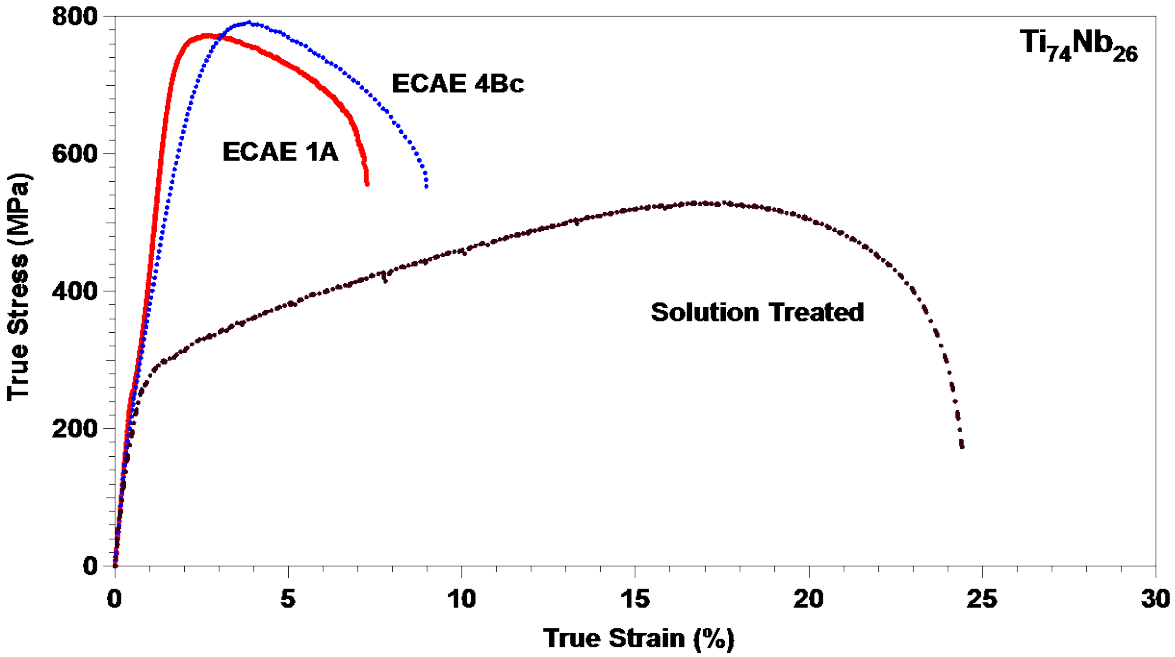

Figure 5.6. Tensile properties of $Ti_{74}Nb_{26}$ SMAs under different processing conditions

5.4. Transformation temperatures

Because differential scanning calorimetry cannot reveal exothermic and endothermic transformation peaks as seen Figure 4.2, constant-stress heating-cooling experiments were used to determine the transformation temperatures of the specimens via extrapolation through the Clausius-Clapeyron relationship (Equation 4.1).

In the as-processed condition, no transformation was observed during constant-stress heating-cooling experiments at any stress level to a temperature as low as -80°C, which is the lower temperature limit on the experimental setup. On the other hand, transformation strain was observed in the solution-treated treated specimen as shown in Figure 5.7. When applied stress is increased, the transformation temperatures, particularly M_s and $A_{f,}$ increases as well.

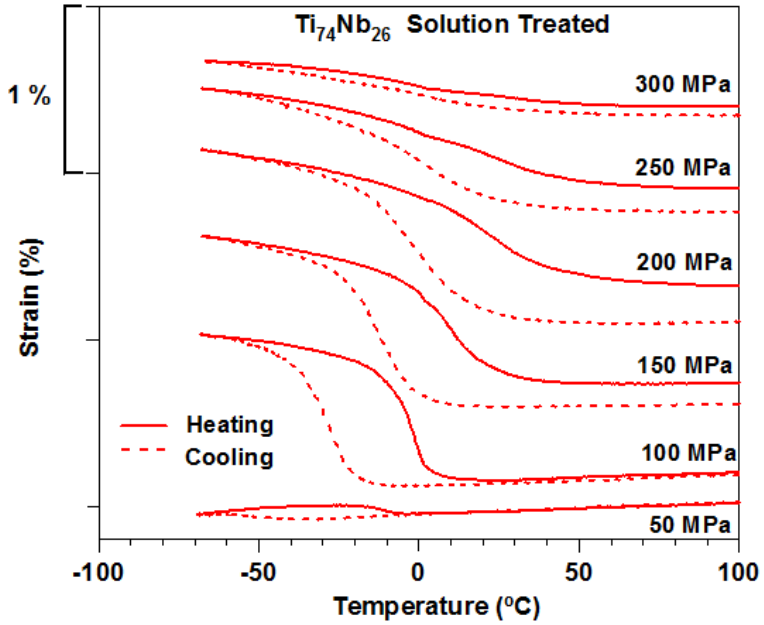

Figure 5.7: Constant-stress heating cooling curves for the solution-treated $TI_{74}Nb_{26}$ shape memory alloy at various stress levels.

Transformation becomes visible in the ECAE 1A specimen when annealed at 500 °C for 10 minutes or longer. Examples of the heating-cooling results at a stress level of 200 MPa are shown in Figure 5.8 for various heat treatments after ECAE route 1A or $4B_c$. The transformation temperatures as a function of applied stress of theses specimens are shown in Figure 5.9.

In polycrystalline SMAs, transformation temperatures are generally lowered by grain refinement and defects such as dislocations [129-131] because they form barriers to the transformation. Therefore, one expects that M_s would be the highest in solution treated specimen since it has the largest grain size, lowest dislocation density, and is devoid of precipitates. While most processed specimens do indeed possess lower M_s than solution treated specimen, this is not the case in A610 and C610.

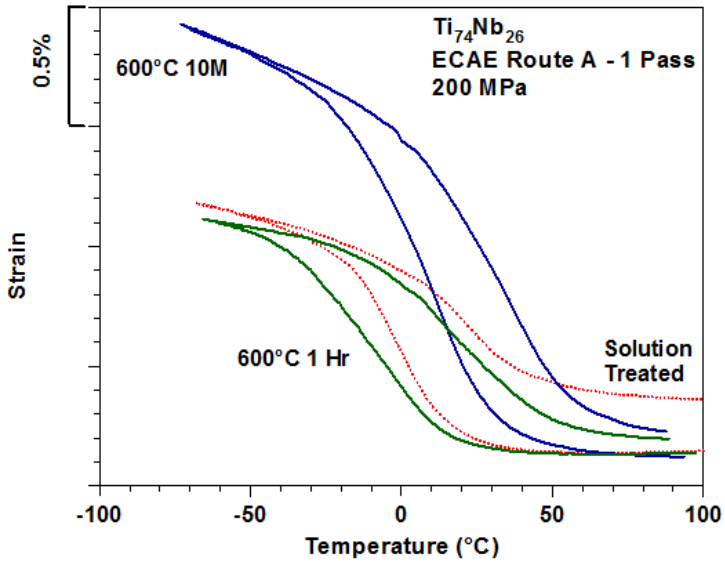

(a)

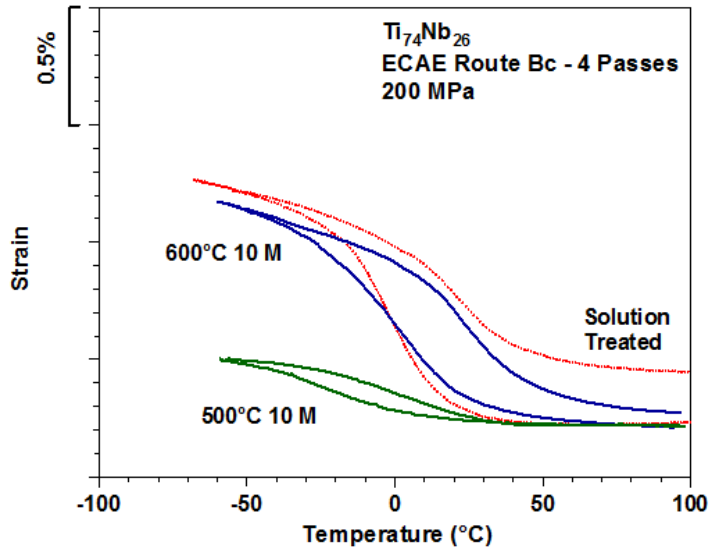

(b)

Figure 5.8: Thermal cycling of $Ti_{74}Nb_{26}$ processed by a) ECAE route 1A and b) ECAE route 4Bc under 200 MPa in tension.

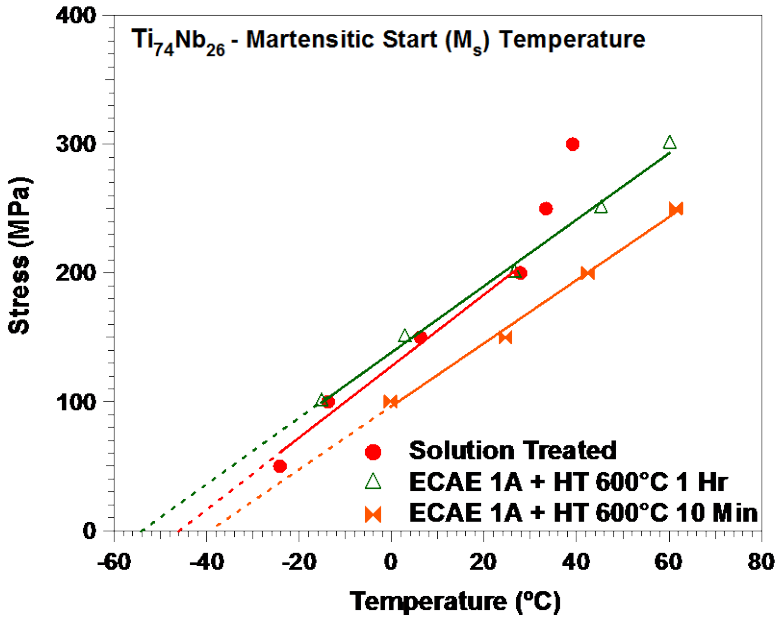

(a)

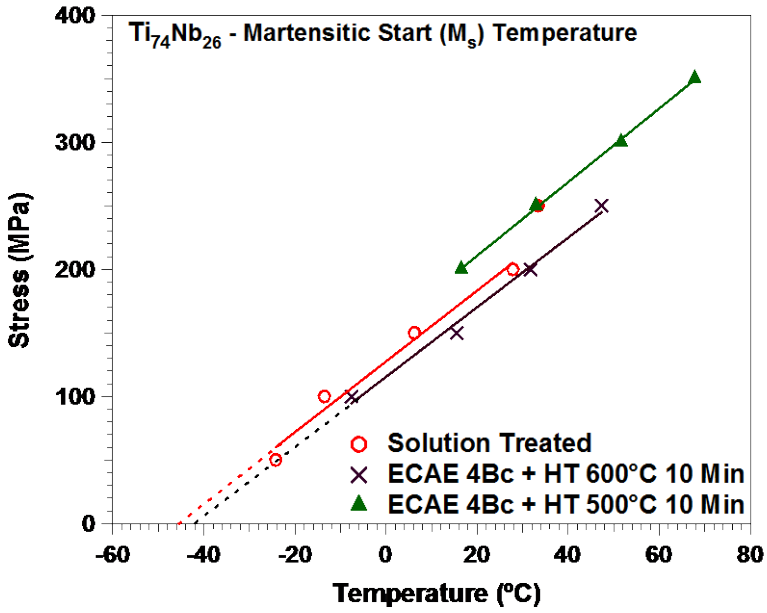

(b)

Figure 5.9: The relationship between martensitic start (M_s) temperature and applied stress levels for a) ECAE 1A specimens, and b) ECAE 4Bc specimens. M_s temperatures were obtained from constant-stress heating cooling experiments in Figure 5.8.

ECAE generates high dislocation density along with a significant reduction of grain size, both of which are expected to suppress martensitic transformation. During the subsequent heat treatment, dislocation density is reduced by recovery and grain size was enlarged through recrystallization. Following a similar path of logic, one would also anticipate that M_s, should also be higher in A61H than A610 since the former possesses larger grains and lower dislocation density simply because of a longer heat treatment. However, the opposite is true, and clearly this explanation based on grain size and dislocation density is insufficient.

Moffat [132, 133] studied the precipitation of ω phase in the same alloy during heat treatment, and found that larger volume fraction of ω precipitates was created by longer heat treatment at the same temperature. This observation was later confirmed by Kim *et al.* [92]. Since ω precipitates are titanium-rich, their appearance increases the niobium concentration in the matrix and reduces the transformation temperatures [92]. This rationalizes the lower M_s in A61H compared to A610.

Combining the effects of grain size, dislocation density, and ω precipitation, the effects of heat treatment on transformation characteristics of $Ti_{74}Nb_{26}$ SMAs can be better understood. ECAE processing creates large dislocation density and refines grain size and reduces Ms temperature. During post-extrusion heat treatment, Ms temperature increase as microstructural recovery and recrystallization occur and the suppressive force of microstructure defects and grain boundaries are gradually weakened. This increase in Ms will continue to a point above the Ms of the solution treated specimen, possibly because at low-to-medium density, defects can act as low-energy heterogeneous nucleation sites for martensite to increase transformation temperature [117-119]. With further heat treatments, titanium-rich ω precipitates form and grow, and M_s again decreases.

5.5. Shape memory properties and transformation strain

Shape memory properties, namely transformation strain (ε_{tr}) and irrecoverable strain (ε_{irr}) were also determined from the constant stress heating-cooling experiments. The progression of ε_{tr} and ε_{irr} as a function of applied stress levels are summarized in Figure 5.10. In both sets of figures, a short duration heat treatment of 10 minutes at 600 °C yielded the highest ε_{tr}. A610 and C610 reach maximum ε_{tr} of about 1.7% and 1.3%, respectively. Not only do ε_{tr} levels of these specimens show marked improvement over that of the solution treated sample, their ε_{irr} is also smaller at most stress levels. Clearly, ECAE processing followed by the appropriate heat treatment improves the shape memory properties of $Ti_{74}Nb_{26}$ alloy over their solution treated counterparts.

We observe from Figure 5.10 that at low stress level, an increase in applied stress is accompanied by a corresponding increase in ε_{tr} regardless of heat treatment. However, at a high enough stress level which depends on the processing conditions, noticeable level of ε_{irr} appears. Finally, a stress level is reached where further increase in stress can no longer increase ε_{tr}, but only ε_{irr}. Compared to the solution treated specimen, maximum (peak) ε_{tr} of ECAE-processed specimens occurs at higher stress levels. Among all specimens, the highest values of ε_{tr} at the peak are consistently observed in the specimen with a 10 minute heat treatment at 600 °C. Unfortunately, ε_{irr} levels are also highest in these specimens.

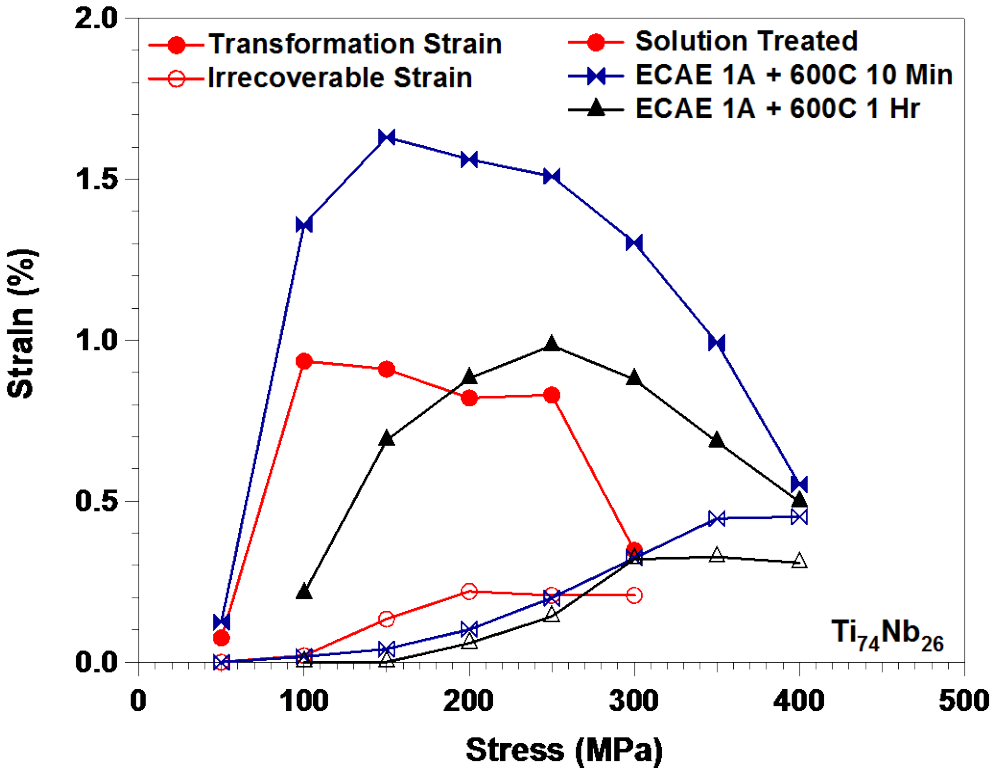

(a)

Figure 5.10: Summary of the dependence of transformation strain and irrecoverable strain on applied stress level from constant-stress thermal cycling experiments shown in Figure 5.8: a) ECAE 1A specimens and b) for ECAE 4Bc specimens.

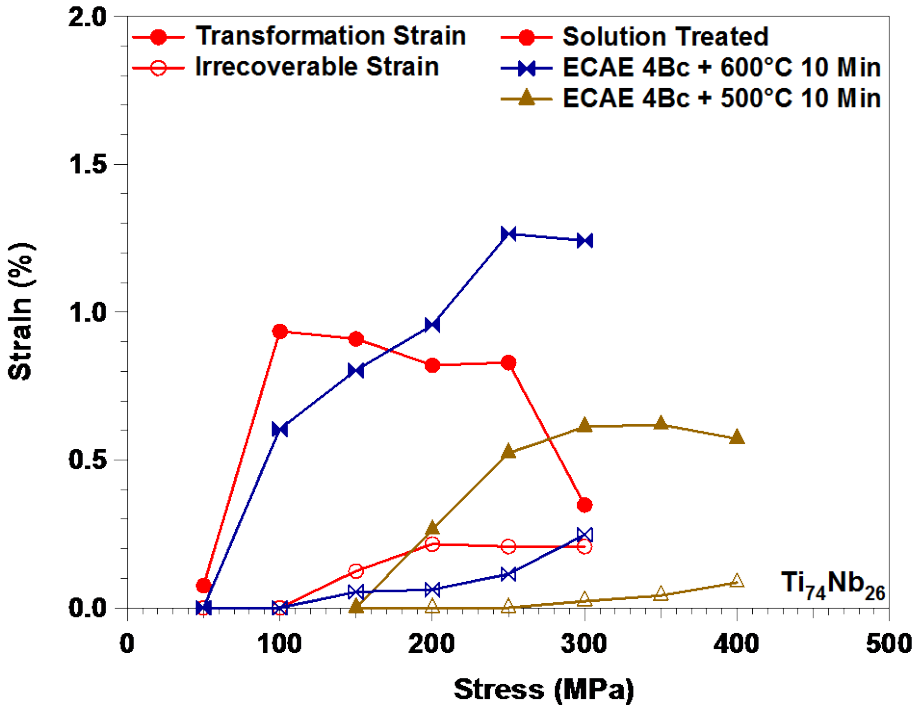

(b)

Figure 5.10 Continued.

This fact that a heat treatment longer than 10 minutes at 600°C and a 10-minute heat treatment at lower temperature than 600 °C both have similar effect on ε_{tr} and ε_{irr} suggests the presence of multiple mechanisms that influence the transformation process. This is further reinforced by trend in the martensitic start (M_s) temperatures for each specimen at varying stress levels shown in Figure 5.9.

However, the explanation used for the trends in M_s temperature cannot fully answer the difference between transformation strains among the specimens. The value of ε_{tr} depends not only on volume fraction of transformation (fraction of austenite transforming into martensite), but also on the degree of martensite reorientation/detwinning and crystallographic texture, both of which are influence by the microstructure. However, it was discussed in Section 5.2 that there were no major differences among the theoretical transformation strains in the specimens

based on crystallographic texture. Table 5.1 shows the comparison between theoretically predicted polycrystalline transformation strains that experimentally predicted ones for various specimens. The differences between the theoretical transformation strains are small. This means the major differences in experimentally observed ε_{tr} among specimens is mainly a function of microstructure, not texture. For the same heat treatment duration of 10 minutes, as noted by the dashed box in Figure 5.11, a higher heat treatment temperature results in ε_{tr} closer to the theoretical maximum. In addition, when both heat treatment temperature and duration are identical, higher ε_{tr} is reached in the single-pass specimen rather than the four-pass specimen. This means the lower ε_{tr} observed in the four-pass specimens is mostly caused by obstacles to transformation from dislocations and grain boundaries – a trend observed in other ECAE processed SMAs [129]. When heat treatment duration is increased to one hour at 600 °C, ε_{tr} deviated further from the theoretical maximum even though more dislocation and grain boundaries were removed through longer recovery and recrystallization. This means ω precipitates have a strong transformation-depressing effect. Compared to the solution treated case, however, both A610 and C610 were able to reach a larger fraction of maximum ε_{tr} while significantly reduce ε_{irr}. ECAE processing also appears to produce a small improvement in texture over the solution treated specimen, in terms of obtaining larger ε_{tr}.

Table 5.1: Calculated polycrystalline theoretical transformation strains and comparison with the experimental observed levels for the $Ti_{74}Nb_{26}$ shape memory alloy processed through various routes.

	ST	A610	A61H	C610	C510
Average φ	24.5	17.2	18	20.9	21.1
Average θ	31.4	35.9	32.9	38.9	36.9
Transformation Strain	2.42	2.6	2.58	2.54	2.54
	2.4	2.6	2.6	2.5	2.5
Max achieved TranStrain	0.935318	1.63115	0.983324	1.265	0.619083
Percent Achieved	38.6495	62.73654	38.113333	49.80315	24.373346

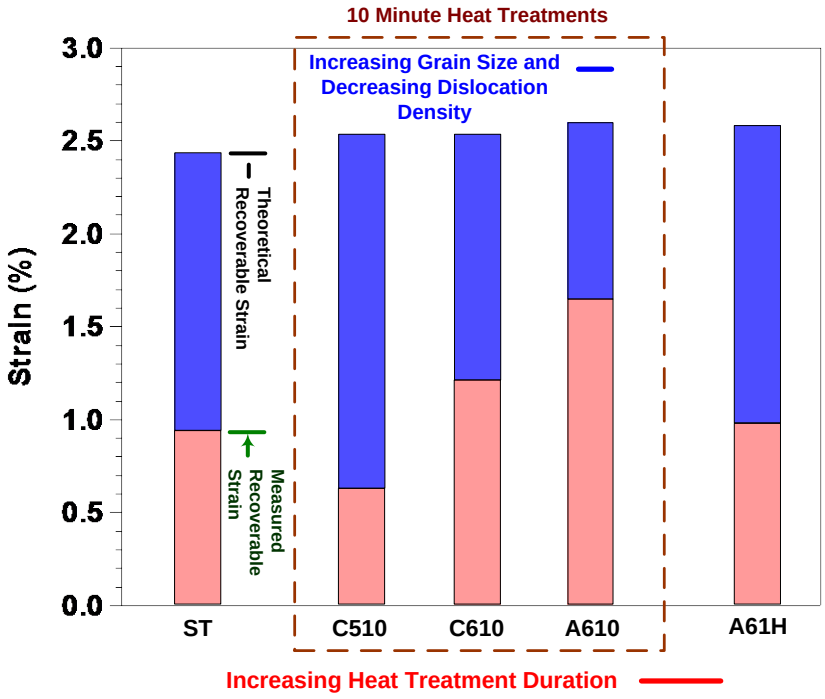

Figure 5.11: The comparison between theoretical recoverable strain and measured recoverable strain for various $Ti_{74}Nb_{26}$ SMA. The boxed bars include all specimens with a 10 minute heat treatments.

5.6. Superelastic properties

From the cooling-heating experiments shown in the previous section, the annealing heat treatment of 10 minutes at 600 °C was chosen for further study. This heat treatment was selected as it showed the largest transformation strains when applied to $Ti_{74}Nb_{26}$ specimens processed by either ECAE route 1A or $4B_c$. In addition, one set of ECAE $4B_c$ specimen heat treated at 600 °C for 10 minutes was further subjected to precipitation heat treatment of 1 hour at 300 °C (C613).

These specimens were loaded in an incremental fashion beginning with 0.5% strain in 0.5% strain increments until a total of 3% strain is reached. The superelastic responses of these three sets are examined and shown in Figure 5.12. A summary of transformation and irrecoverable strains as a function of applied strain is shown in Figure 5.13. Similar to their shape memory responses, the superelastic strain initially increases with increasing applied strain (thus increasing applied stress) until a peak is reached. After this peak, superelastic strain can no longer increase as plastic deformation becomes the dominant mechanism. By finding the applied strain level when the peak is reached, and determining the corresponding stress level at that level of applied strain, it is possible to determine the critical stress level when plastic deformation becomes the dominant deformation mechanism. For each of the three specimens, this calculated stress level is shown in Figure 5.14. Not surprisingly, the strength of A610 is the lowest at approximately 430 MPa while the C610 specimen, with grain size one order of magnitude smaller, has strength of nearly 480 MPa. After precipitation heat treatment, the strength of C613 increases further to 525 MPa.

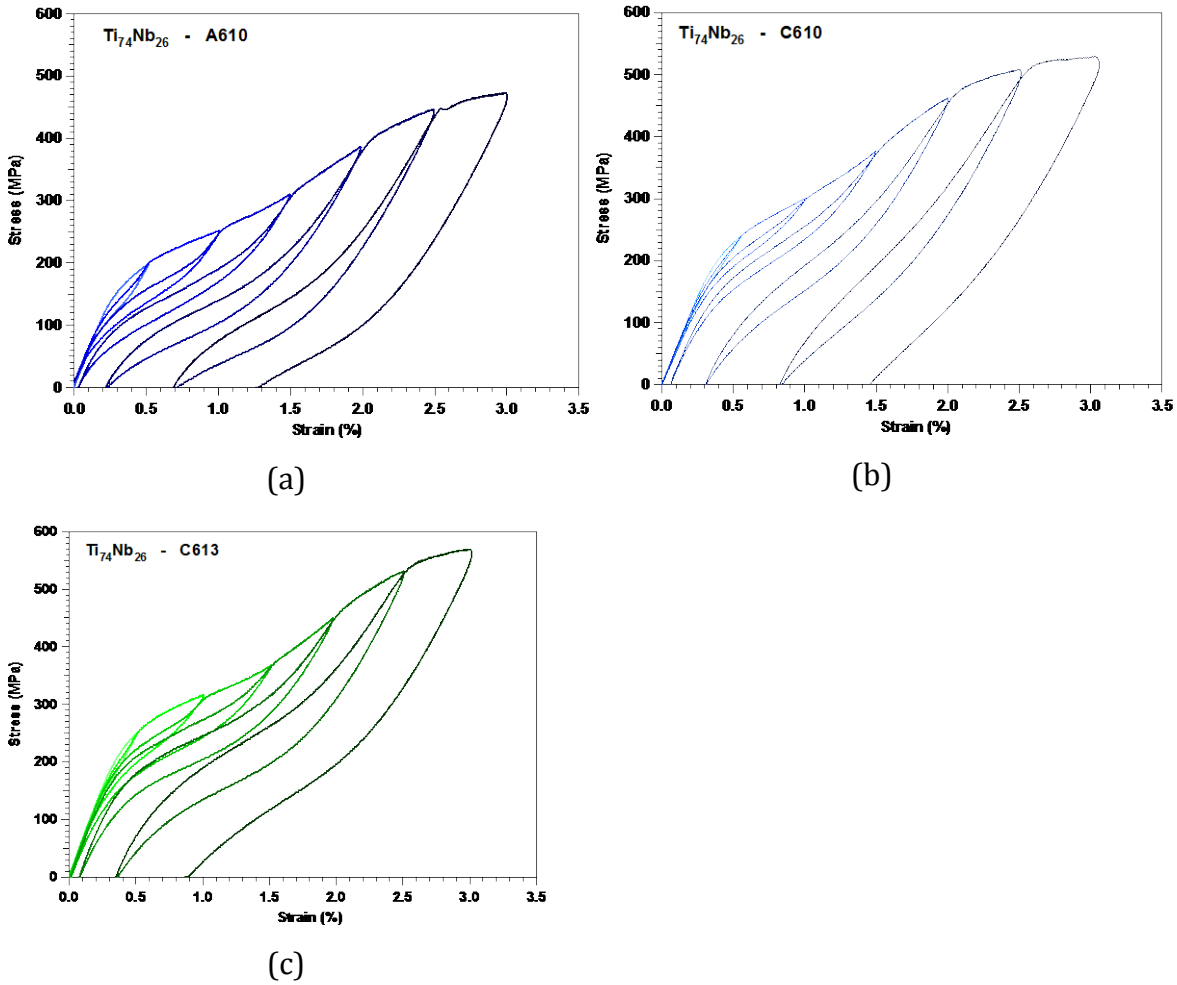

Figure 5.12: Incremental strain superelastic experiments for A610 (a), C610 (b) and C613 (c) up to 3% strain at room temperature

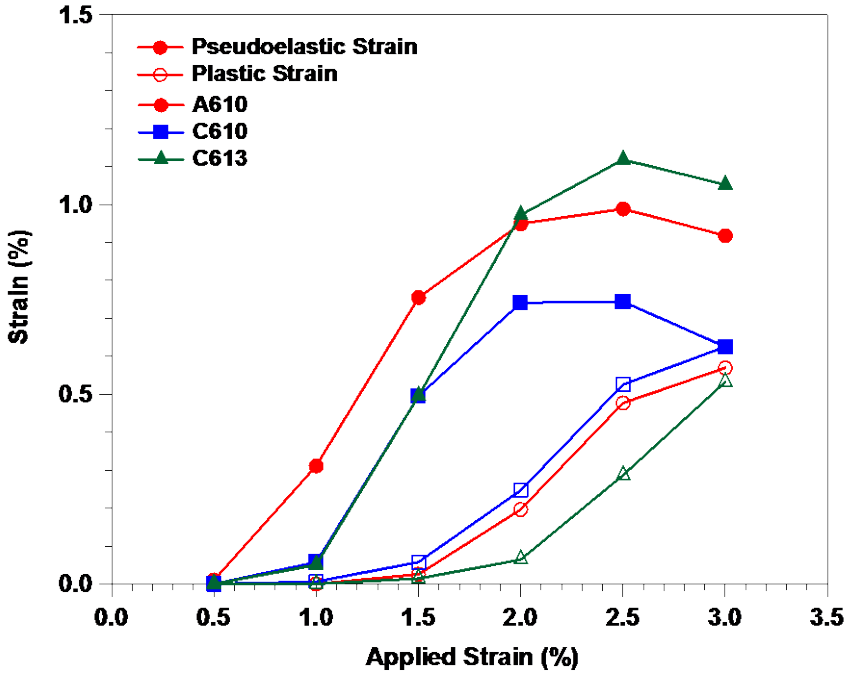

Figure 5.13: Summary of transformation and irrecoverable strains from the incremental superelastic experiments shown in Figure 5.12.

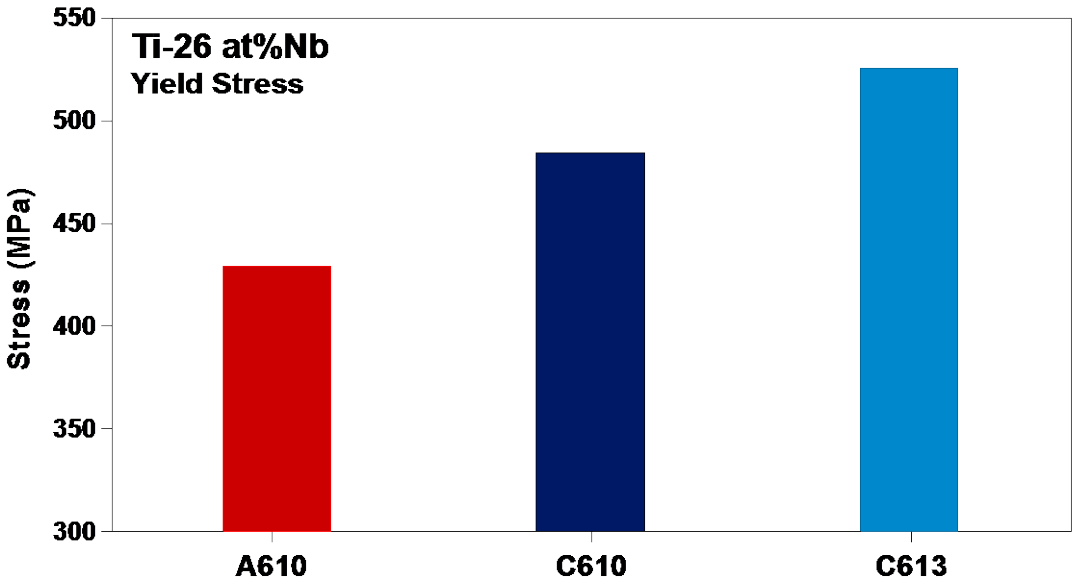

Figure 5.14: Microscopic yield stress calculated from the stress level at the maximum superelastic strains shown in Figure 5.13.

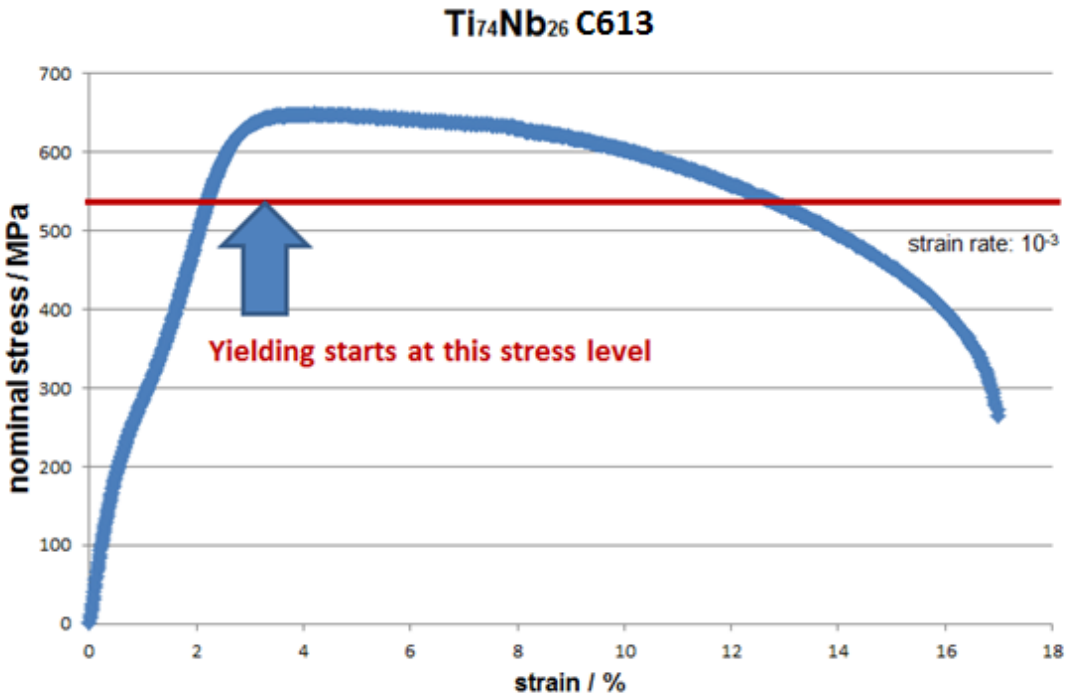

Figure 5.15: Microscopic yield stress calculated from the stress level at the maximum superelastic strains shown in Figure 5.13.

However, it is important to note that this stress level is much lower than the yield point seen in a monotonic stress-strain curve shown in Figure 5.15. Here, for the C613 specimen, the macroscopic yield point occurs at a stress level of over 650 MPa. However, the stress level at which plastic deformation becomes dominant is more than 100 MPa lower. This is likely caused by the phase transformation process itself: during the movement of the transformation phase front, high local stress concentration often occur from the interactions among various martensitic phase fronts, as well as with other microstructural features such as dislocations and precipitates. These stress concentration lead to local yielding that may not be immediately obvious from the stress-strain diagram, but manifests as irrecoverable strain upon unloading. Thus, it is important in the design of superelastic materials

to understand that the actual strength of the SMAs tend to be much lower than what is observed during standard experiments.

Given the results in Figure 5.14, it is perhaps surprising to see that the superelastic response of the A610 specimen compares much more favorably to that of C610, whose strength is about 50 MPa higher. Unfortunately, the same microstructural features, such as smaller grain size and higher dislocation density that increases the strength of the alloy also makes transformation more difficult, and increased the σ_{SIM} of C610 by about 40 MPa. Furthermore, the stress-strain curve hardens more significantly in the C610 specimen compared to A610. This rapid increase in stress level with increase in applied strain quickly nullifies the higher strength of C610. After 3% applied strain, the irrecoverable level of A610 is about 1.3%, while it is close to 1.5% in C610.

Further improvement in strength through precipitation hardening is nevertheless effective. Although stress levels has increased even further in C613, the nearly 80 MPa increase in strength of C613 was able to offset this such that only 0.9% irrecoverable strain was accumulated after 3% applied strain – a clear improvement over either A610 or C610.

Finally, it is likely that crystallographic texture plays little or no effect in the role of yield strength of the material. We have shown in section 5.2 that the effect of crystallographic texture on transformation was negligible due to the weak texture in the annealed specimens. The same argument can be applied for the effect of crystallographic texture on yield strength. Furthermore, the structure of the austenite is body-centered cubic, who has very weak orientation dependence of its Schmid Factor due to the large number of slip modes enabled by the <111> pencil glide type deformation. We plot the average orientations of the A610 and C613 specimens on a stereographic triangle showing the orientation dependence of the Schmid Factor in BCC materials (Figure 5.16), and there is very little difference between the two specimens. This means that once again, microstructure is the key determining factor in the superelastic properties of the $Ti_{74}Nb_{26}$ SMAs.

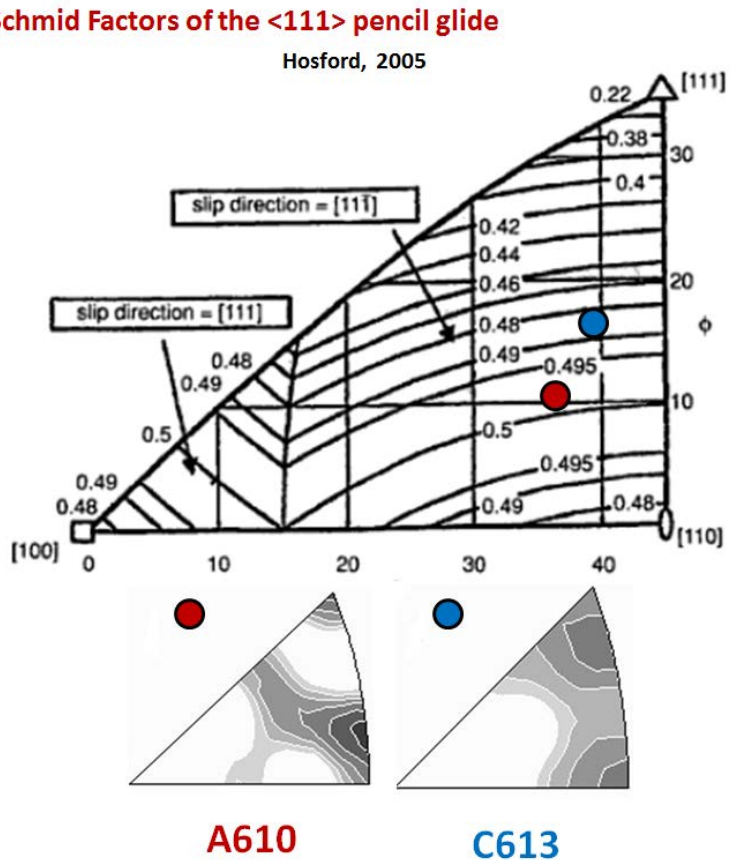

Figure 5.16: Comparison of the Schmid factors of the averaged orientations of A610 and C613, in a similar fashion as Figure 5.5. Because of the various slip modes available to bcc materials, there is little difference between the expected Schmid factors of the two specimens, which suggests that texture has a minimal effect in the yield strength of the two samples [134].

5.7. Superelastic cyclic response

During constant-temperature superelastic cycling, a number of superelastic properties changes, as demonstrated in Figure 5.17. With increasing number of cycles, σ_{SIM} and $\Delta\sigma$ decreased, and ε_{irr} increased in the initial stages of cycling. Figure 5.18 shows a summary of the evolution of σ_{SIM}, $\Delta\sigma$, and ε_{irr} during cycling. In Figure 5.18a, σ_{SIM} of C613 is higher than that of A610, implying that the ω

precipitates, smaller grain size and higher dislocation density of C613 stabilized the austenite relative to martensite and effectively lowered the transformation temperatures of the alloy. The lower the transformation temperature, the higher the σ_{SIM} would be at room temperature. Both precipitates and dislocations hinder the movement of martensite interface during transformation, thus increasing the total energy demand of the transformation and increasing σ_{SIM}. Simultaneously, σ_{SIM} is also affected by the change in chemistry from precipitation. The ω precipitates are rich in titanium [132], so their appearance increases the niobium concentration in the matrix. A higher niobium concentration lowers transformation temperatures [89], which further raises σ_{SIM} in precipitated samples.

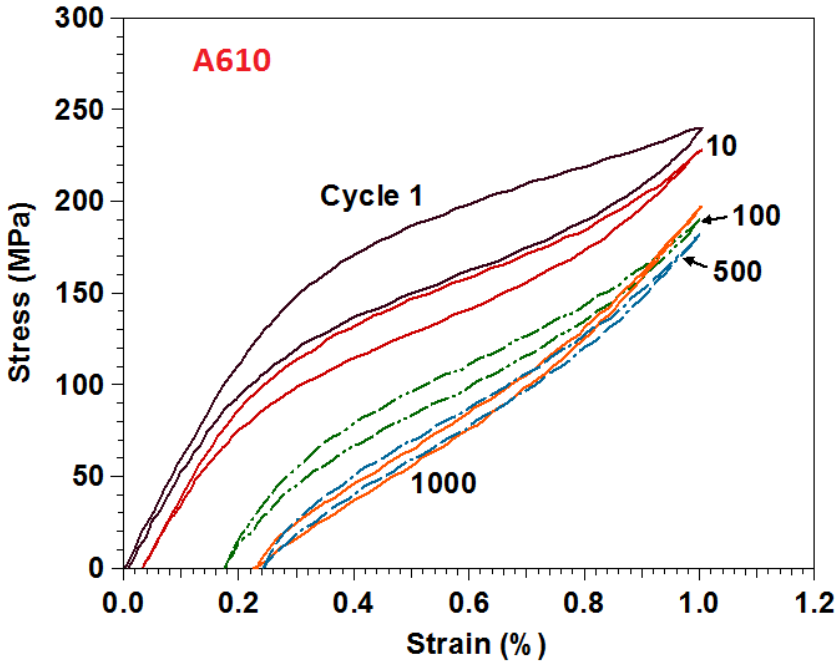

Figure 5.17: Room temperature superelastic cycling behavior of the A610 $Ti_{74}Nb_{26}$ sample.

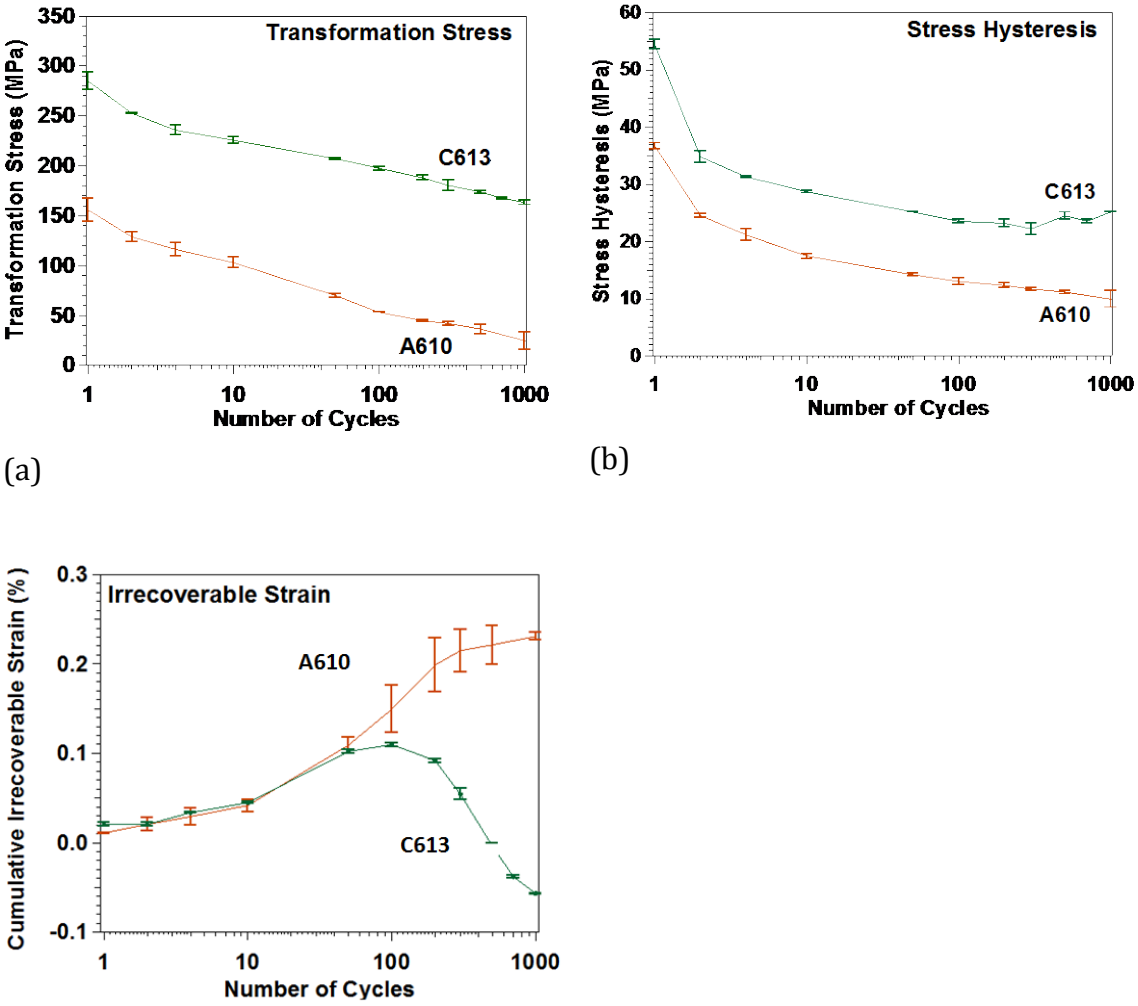

Figure 5.18: The evolution of a) σ_{SIM}, b) $\Delta\sigma$, and c) ε_{irr} as a function of number of cycles on a log scale. Error bars indicate the variations in the measurements on different samples.

Over the course of 1000 superelastic cycles to 1% strain, the σ_{SIM} of both specimens decreased by about 130 MPa. The fall of σ_{SIM} during cycling is in agreement with the results of Tahara *et al.* [101], who studied cold rolled specimens under similar sets of heat treatments yielding microstructures close to those present in the ECAE specimens studied here. The initial $\Delta\sigma$ is also higher in

C613 as shown in Figure 5.18b, and $\Delta\sigma$ of both specimens decreases with increasing number of cycles. $\Delta\sigma$ is a measure of energy dissipation and it is caused by interfacial friction and creation and/or rearrangement of defects during the martensitic transformation. The effect of defect generation and rearrangement is usually high in the first cycle, and becomes less significant with each additional cycle. Therefore, the change in $\Delta\sigma$ is most pronounced in the first few cycles and then $\Delta\sigma$ tends to saturate.

While the trends are similar in σ_{SIM} and $\Delta\sigma$, they are completely different from the evolution of ε_{irr} during cycling as shown in Figure 5.18c. While the cyclic evolution of ε_{irr} of A610 follows the expected trend and increases monotonically, the cumulative ε_{irr} of C613 increases initially, but at some point, begins to decrease. In other words, ε_{irr} incurred during the initial cycles is gradually being recovered and completely eliminated simply by the continued cycling process in the C613 specimens. This behavior appears to depend on the microstructure. In A610, which has smaller dislocation density, larger grains and no precipitates, ε_{irr} reaches higher levels and appears to saturate at a maximum at 1000 cycles, but recovery is not seen. On the other hand, C613, which has large dislocation density, much smaller grains and contains precipitates, shows a smaller maximum value of ε_{irr} that is reached sooner at around 100 cycles before recovery begins. Furthermore, the total recovery in C613 actually exceeds the maximum ε_{irr} accumulated during cycling, so that the final strain was smaller than the initial strain, meaning that the specimen experienced a permanent deformation in a direction opposite to the loading at the end of cycling. This behavior is presented on a stress-strain diagram in Figure 5.19; the reason for this repeatable over-recovery is not yet known.

This evolution of ε_{irr} of C613 during superelastic cycling is counterintuitive. Not only does this mean that the ε_{irr} is actually recoverable, but also that the cycling process, which is the same process that created the ε_{irr} in the first place, also can facilitate its disappearance. To assure that there is no experimental error, this experiment was performed multiple times under several different experimental

setups and strain measurement techniques on specimens processed by ECAE route 4Bc with different heat treatments than that of C613. Although the cycle number at which the maximum ε_{irr} occurred changed depending on the heat treatment, the recovery phenomenon observed in C613 persisted in all these specimens. Tahara *et al.* [101] have shown through in-situ XRD and TEM experiments that a large part ε_{irr} accumulated during superelastic cycling is made up of retained martensite that did not transform back to austenite after unloading.

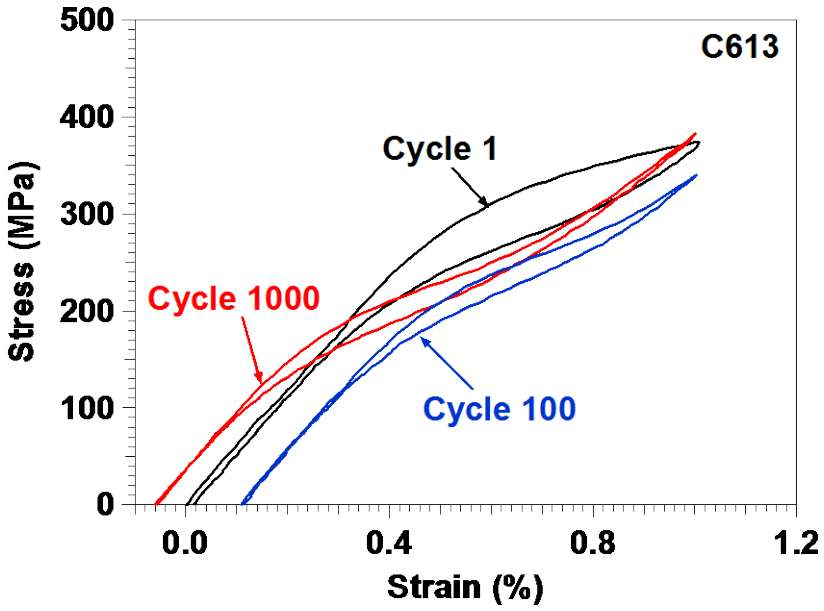

Figure 5.19: The superelastic cycling and room temperature aging effect on C613. ε_{irr} reaches negative levels after 1000 cycles – as summarized in Figure 5.18c.

However, the recovery of ε_{irr} during cycling was not observed in the cold rolled specimens. In the present work, total deformation of specimens is only 1% strain. This applied strain is about 50% of the maximum superelastic strain of the specimens, and the applied stress level reached should be below the macroscopic

yield point of the alloy. It is, therefore, reasonable to assume that most or even all of ε_{irr} in this case is caused by retained martensite, and the strain recovery is caused by the disappearance of the retained martensite during cycling. We confirmed this by heating up a specimen after 1000 superelastic cycles. Figure 5-20 clearly shows significant strain recovery during heating, such that the majority of irrecoverable strain accumulated during cycles was recovered in this process. Furthermore, recovery of the ε_{irr} starts almost immediately upon heating, and it is possible that continued cycling at room temperature would be sufficient. This point will be further discussed in Section 7 on room temperature recovery.

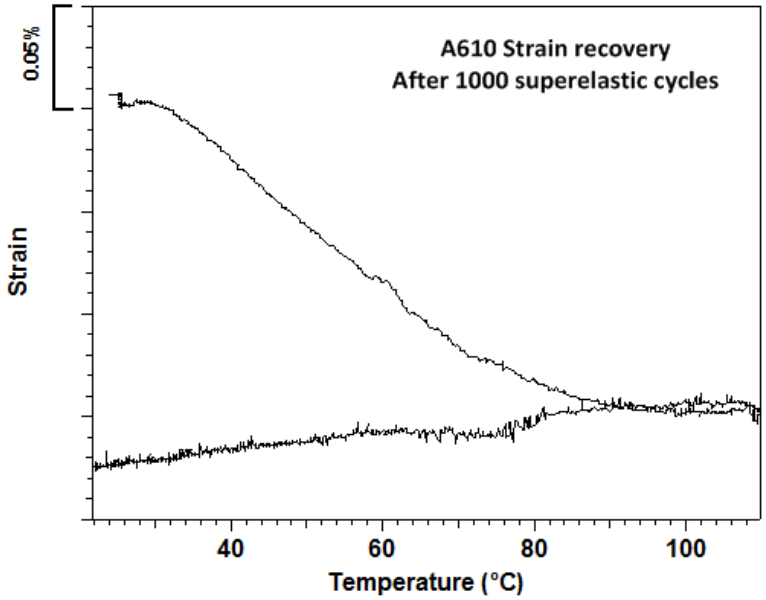

Figure 5.20: Recovery in strain upon heating an A610 specimen that experienced 1000 superelastic cycles at room temperature. Over 80% of irrecoverable strain accumulated during cycling was recovered.

6. REDUCTION OF EFFECTIVE MODULUS

The Ni-Ti shape memory alloy around equiatomic composition, known as nitinol, have been widely used in medical devices such as stents, arterial occluders, and guidewires due to their ability to produce a large, reversible shape change. They have also been frequently mentioned as a possible material for structural implants such as hip and knee replacements. The reason is the low apparent modulus of Ni-Ti, often reported to be around 40 GPa or lower [7]. However, recent neutron diffraction studies and first-principle calculations suggest the true elastic modulus of martensite to be above 100 GPa [42-45]. The reason that a much lower value is obtained from simple mechanical experiments is caused by the combination of elastic deformation and martensite detwinning and reorientation. Strain from the latter two sources is not completely reversible, and is not acceptable for applications.

However, the mechanical behavior of Ni-Ti in the martensite state introduces a new way of reaching a low elastic modulus: instead of depending only the elastic deformation, it is possible to combine elastic deformation with another reversible deformation mode to result in a reduced apparent elastic modulus without actually affecting the true elastic modulus or other mechanical properties of the alloy.

We have created such a method by combining elastic deformation and reversible stress-induced phase transformation in both the Ti-Nb and Ni-Ti shape memory alloys, and achieved an apparent modulus of below 30 GPa. Furthermore, this method enables the alloy to automatically adjust its apparent elastic modulus to the properties of the surrounding bone: when the surrounding bone weakens, the apparent elastic modulus of the material will be reduced in response, and vice versa.

Normally, a relatively high stress level is needed to trigger the stress-induced transformation. This stress level is too high for the natural load state of the

body to trigger the transformation. Through superelastic cycles, it is possible to reduce the transformation stresses to very low levels. The Ti-Nb A610 alloy was cycled 1000 times at room temperature to 1% strain as described in Section 5.7. Figure 5.17 shows the resulting stress-strain curves. It is clear that transformation stress decreases significantly from about 150 MPa to about 20 MPa after 1000 cycles. Figure 6.1 shows the stress-strain behavior of the Ti-Nb alloy before and after cycling compared to other metallic materials – prior to cycling; the elastic modulus of Ti-Nb is about 65 GPa, similar to that of the Ni-Ti in the austenite state, and about 1/3 of value of stainless steel. On the other hand, after 1000 cycles, the effective modulus, or the secant modulus, is further reduced due to the early introduction of stress-induced phase transformation.

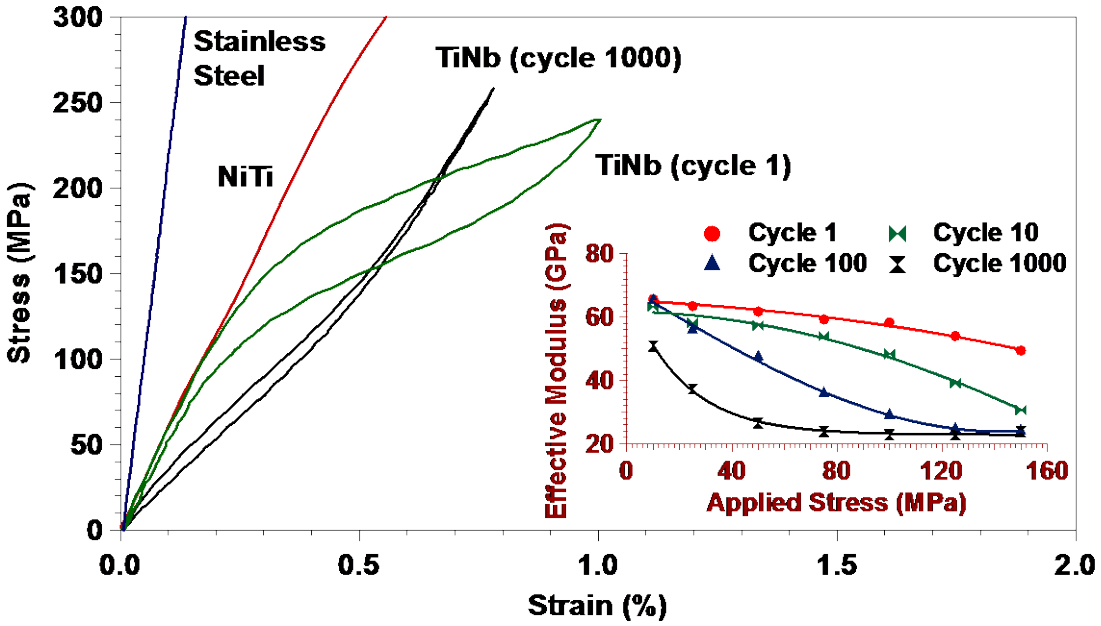

Figure 6.1: Comparison of the stress-strain response of stainless steel, Ni-Ti shape memory alloy, and the $Ti_{74}Nb_{26}$ A610 shape memory alloy before and after 1000 superelastic cycles. The inset shows the effective modulus (secant modulus) of the Ti-Nb SMA after various numbers of superelastic cycles as a function of stress level.

The reduced effective modulus is enabled by the stress-induced phase transformation which takes place at a very low σ_{SIM}. The effect of cycling reduced the σ_{SIM} level at cycle 1000 to about 20 MPa, and at this point, the stress-strain curve deviates from linearity and the slope is gradually reduced. At about 75 MPa, the stress-strain curve of the cycle 1000 specimen reaches an inflection point and the slope begin to increase once again. This means that the effective modulus is not only a function of the number of superelastic cycles, but also a function of the stress level. The inset of Figure 6.1 shows these relationships: as applied stress and number of superelastic cycles increase, the effective modulus drops from the original value of nearly 65 GPa to a minimum of about 22 GPa at about 75 MPa in cycle 1000. We call this method of modulus reduction "cyclic softening".

To support that stress-induced phase transformation was responsible for the non-linear behavior of the stress-strain curve even at low stress levels, in-situ X-ray diffraction experiments were carried out under a load of 100 MPa for a specimen before and after superelastic cycling. Prior to cycling, there is no change in the X-ray peak profile of the specimen as load is applied, other than an expected shift in the austenite peak, as shown in Figure 6.2. However, when the same stress is applied to a specimen after 1000 superelastic cycles, a martensite peak appears, indicating the onset of transformation. This agrees with the stress-strain diagram shown in Figure 5.17, where 100 MPa was enough to trigger transformation after cycling, but not before.

Although the stress-strain diagram is not linear, the strain sustained is nevertheless completely recoverable and should be suitable for implant applications. At the same time, the non-linearity of the stress-strain diagram opens up another function: the ability of the material to automatically adjust its effective modulus based on the mechanical properties of the surrounding bone.

Stress shielding occurs because the implant material carries a larger portion of the load than the surrounding bone, due to the higher elastic modulus of the implant. For implant constructed of conventional metals and alloys, the effect of

stress shielding will naturally intensity as bone resorption and loss leads to further transfer of load to the implant, and accelerates the bone loss process. However, in the cyclically-softened Ti-Nb SMA, if bone loss occurs that leads to the transfer of more loads to the implant, the effective elastic modulus of the implant will be reduced and return the load back to the bone and preventing further degredation. The stress-dependence of the effective modulus allows the implant to adjust its properties based on its operating environment: if a higher than desired level of load is carried by the implant, it will automatically reduce its effective modulus to transfer load back to the surrounding.

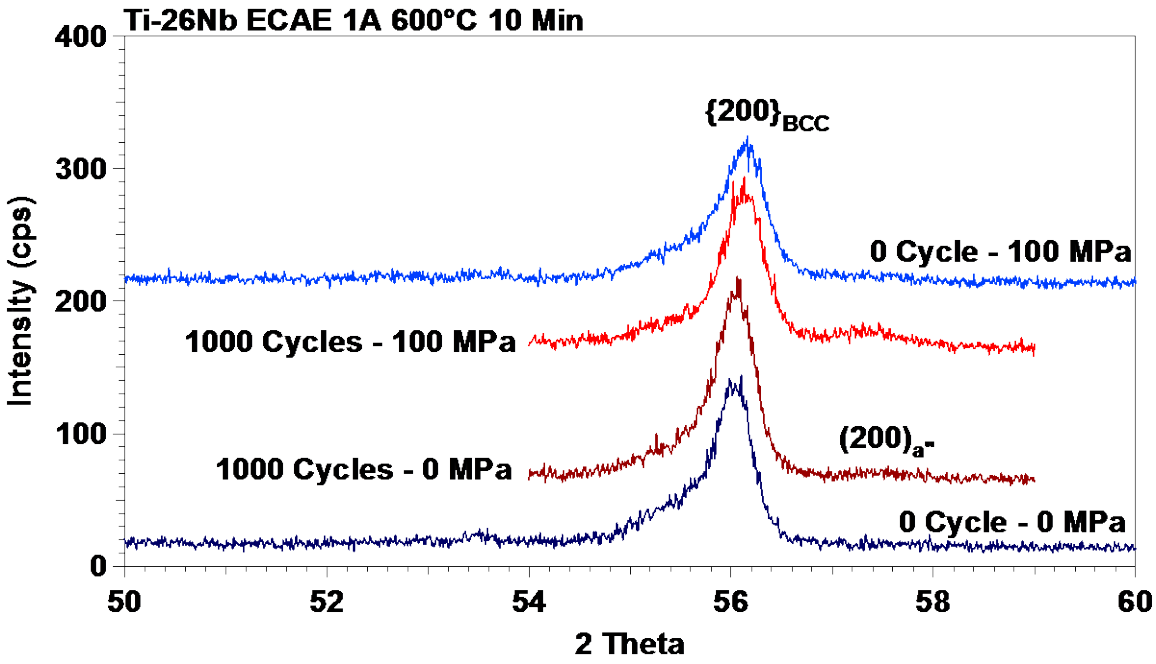

Figure 6.2: X-ray diffraction pattern of the $Ti_{74}Nb_{26}$ A610 specimen before and after 1000 cycles. In both cases, the specimen was loaded to 100 MPa on an in-situ stress stage (see section 4.7). The intensity of the α" martensite peak is higher at under 100 MPa in the specimen cycle 1000 times than the intensity of the un-cycled specimen.

Finally, the stress-induced transformation approach allows the effective modulus of the material to be reduced without affecting other mechanical properties, as shown in Figure 6.3. In metallic materials, the elastic modulus of a material and its ultimate strength are directly correlated: stiffer materials are generally stronger. Thus the act of reducing the elastic modulus is often accompanied by a reduction in ultimate strength, and thus fatigue resistance – both parameters crucial to implants designed for long operating lifetimes. Similarly, the low elastic modulus of porous materials comes at the cost of strength as well. However, the stress-induced transformation approach does not actually change the inherent elastic constant of the material, but rather introduces a second reversible deformation mechanism to reduce the effective modulus. This means that the inherent material properties, such as strength, are not affected – the effective modulus is reduced without compromising other properties.

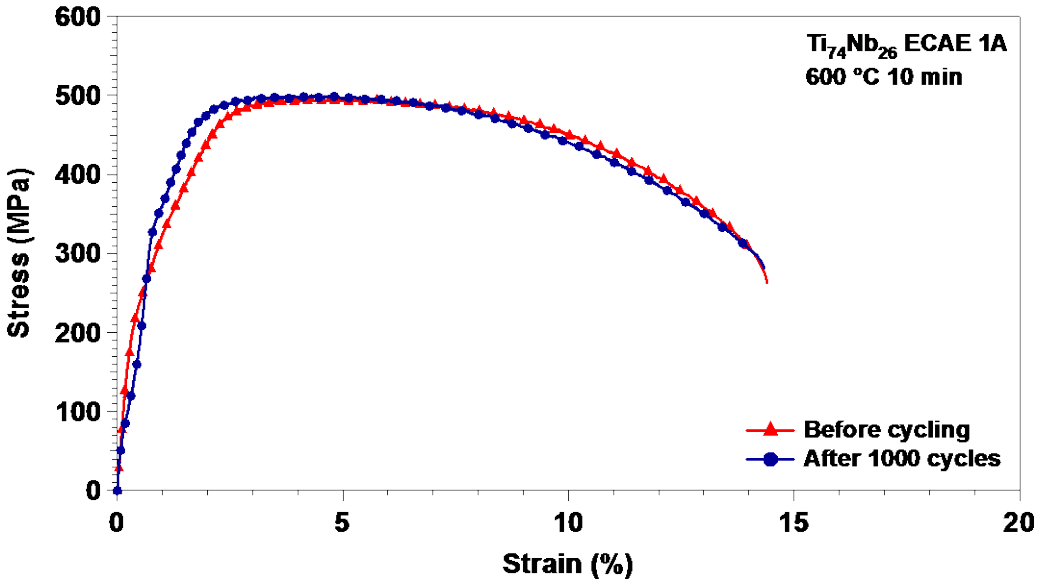

Figure 6.3: Stress-strain diagram of the A610 alloy before and after 1000 superelastic cycles. Although cycling reduces the effective modulus, it does not affect the mechanical properties of the material.

However, stress of bones in the human body from everyday activities is very difficult to measure. Therefore, it is helpful to examine the effective elastic modulus of the material at strain levels expected for the human bone. Yang *et al.* [135] surveyed experiments where strain gages were implanted unto the tibia of patients to determine the strain caused by various activities. We then convert these strains into stress values assuming an elastic modulus of 30 GPa for the bone. These results are shown in Figure 6.4.

Walking produces a load of about 30 MPa, which corresponds to an effective modulus of about 35 GPa for the A610 Ti-Nb alloy cycled 1000 times. On the other hand, jogging produces 40 MPa of stress, reducing the effective modulus of the alloy to below 30 GPa. Therefore, the reduction is relevant to the stress levels that the implant is expected to experience in everyday life.

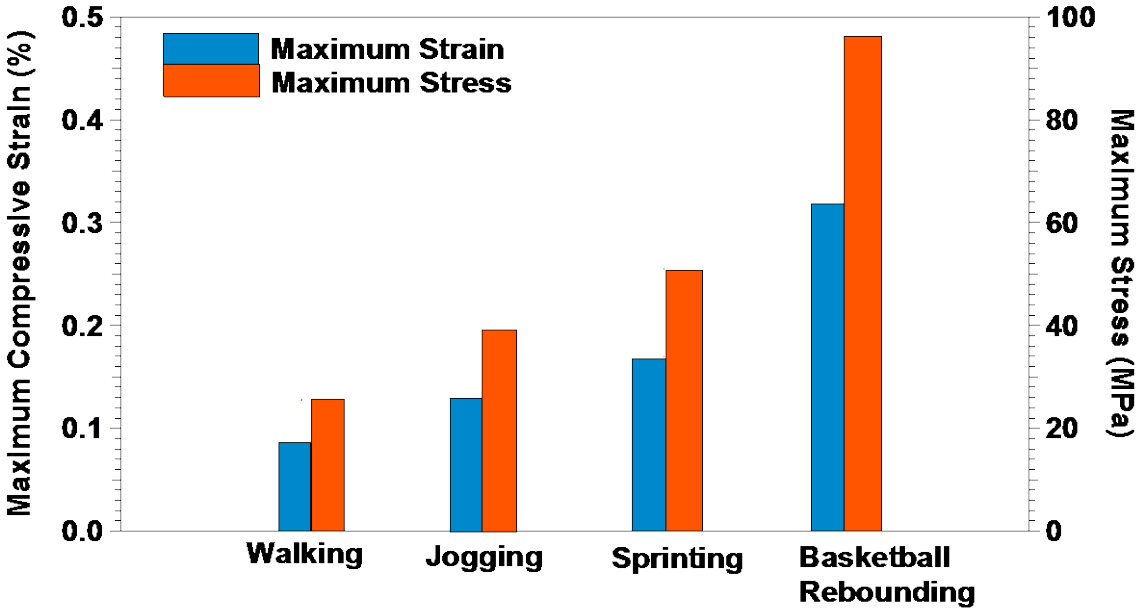

Figure 6.4: Maximum compressive strain and stress experienced by the human tibia from a variety of activities [135].

However, the effectiveness of softening is affected by the initial condition of the alloy. Figure 5.18a shows the relationship between σ_{SIM} and number of cycles in the A610 and C613 specimens. While both experiences reduction in σ_{SIM} of C613 remains above 150 MPa after 1000 cycles. Since the reduction in effective modulus depends on reducing σ_{SIM} to very low levels, the modulus of C613 does not change until the applied stress level exceeds 150 MPa. Such stress level is not expected for an implant, according to Figure 6.4, thus the cyclic softening technique is not effective for C613. It should also be noted that the transformation stress values achieved through cycling is lower than what is normally possible through changing the superelastic temperature relative to the transformation temperature of the material. In the austenite state, the transformation stress is directly proportional to the temperature at which the material is deformed. Thus, if the experiment is carried out at temperatures closer to the austenite finish (A_f) of the material, the transformation stress is naturally lowered, as shown in Figure 6.5. However, there is a limit to this type of reduction, and σ_{SIM} values below 100 MPa are very difficult to achieve by changing the experiment temperature alone. By comparison, for a specimen cycled 1000 times to 1% strain, the minimum achievable transformation stress varies only weakly with testing temperature and remains much lower than the specimen without cycle at all temperatures. This means that cyclic softening is required to achieve the ultra-low elastic modulus of the material.

One practical problem with the cyclic softening technique is the amount of cycles required to achieve the desired level of σ_{SIM}. It is neither economical nor practical to apply 1000 cycles individually to each device, and a simpler method is needed. Luckily, 1000 superelastic cycles to 1% strain can be replaced by 1 cycle at a high strain level (Figure 6.6). When the specimen (A610) was cycled once to 2.5% strain, the transformation stress level was reduced from 150 MPa to about 30 MPa immediately, thus greatly simplifying the cyclic softening process.

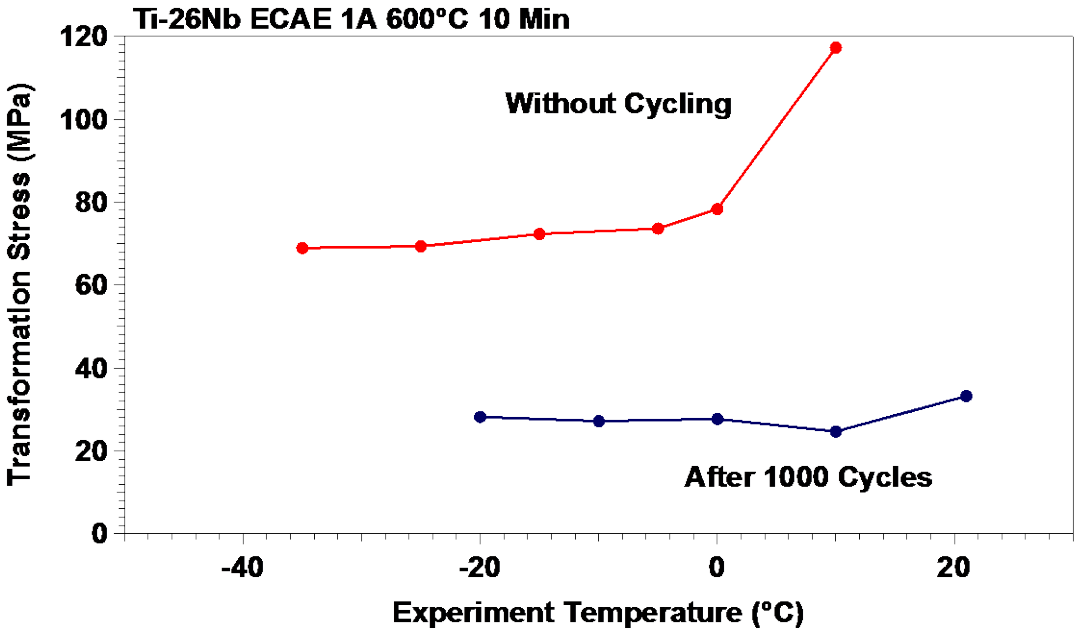

Figure 6.5: The dependence of transformation stress on the testing temperature in the A610 specimen before and after 1000 superelastic cycles.

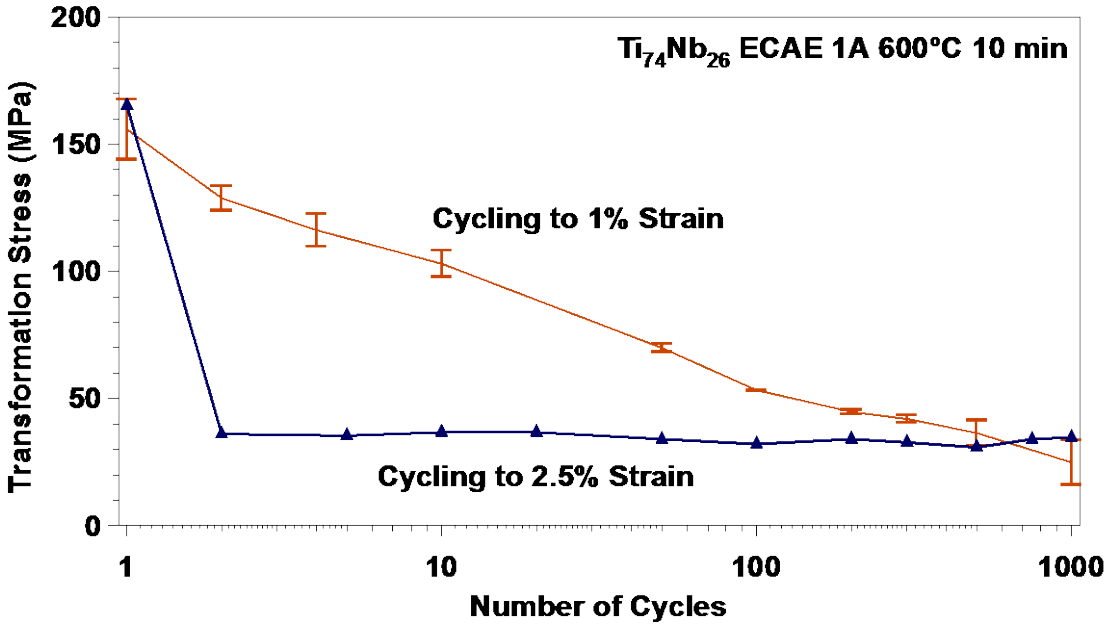

Figure 6.6: the dependence of transformation stress with number of superelastic cycles to 1% or 2.5% strain.

The other main problem with the technique is the lack of stability. We have shown that the cyclically reduced transformation stress is capable of self-recovery at room temperature [97, 98]. If a Ti-Nb SMA experiences no stress for one day at room temperature, 30% of the reduction in transformation stress is recovered, and over 70% was recovered in one week. While implants are expected to experience stress inside the human body consistently, this instability makes it necessary to apply the cycles right before the installation of the implant, which is undesirable. In general, materials are show a greater and faster reduction in transformation stress during cycling also experiences faster recovery. This is a problem that must be solved before this technique can be realistically applied to implant materials. This behavior will be discussed in greater detail in section 7.

In summary, we introduce a stress-induced transformation technique through cyclic softening to create alloys with ultra-low effective elastic modulus below 30 GPa, about half the value of the lowest reported stiffness value of 55 GPa in biomedical alloys, without negatively affecting other mechanical properties of the material. The shape of the stress-strain curve of the material further allows the material to self-adjust to the condition of the surrounding both in order to more effectively combat stress shielding. We believe this technique can be applied to all SMAs showing superelasticity.

7. LOW-TEMPERATURE INSTABILITIES OF THE $Ti_{74}Nb_{26}$ SHAPE MEMORY ALLOY

7.1. Low temperature recovery of low-cycle functional fatigue

It was discussed in section 6 that the cyclic-induced effective modulus reduction faces some instability even at low temperatures. A similar behavior was observed during the room temperature cyclic experiments discussed in section 5. There, it was mentioned that the C613 spontaneous recovers its accumulated irrecoverable strain during superelastic cycling after about 200 cycles, as shown in Figure 5.17c.

This evolution of ε_{irr} of C613 during superelastic cycling is counterintuitive. Not only does this mean that the ε_{irr} is actually recoverable, but also that the cycling process, which is the same process that created the ε_{irr} in the first place, also can facilitate its disappearance. We have also showed that a large amount of the ε_{irr} in the A610 was caused by retained martensite, which could be recovered upon heating to a moderate temperature of 100 °C.

Even though ε_{irr} recovers during cycling for only C613, the trend of ε_{irr} and $\Delta\sigma$ of C613 shows no difference to that of A610, so it is doubtful that the exact same mechanism is responsible for changes in ε_{irr}, σ_{SIM}, and $\Delta\sigma$ during cycling. Nevertheless, the recoverability observed in ε_{irr} raised the question of whether σ_{SIM} and $\Delta\sigma$ can be recoverable at room temperature even though it does not happen during cycling. To test this, specimens were allowed to stay at room temperature under stress-free conditions for up to 10 days, and single-cycle superelasticity experiments were performed at intermediate periods under identical conditions as the initial cycling experiment. Recovery in both σ_{SIM} and $\Delta\sigma$, as demonstrated for C613 in Figure 7.1, takes place for both A610 and C613 during stress-free room temperature aging. The evolution of σ_{SIM} and $\Delta\sigma$ in these experiments are shown in Figure 7.2a. Recovery in $\Delta\sigma$ saturates within less than 100 hours of aging time, but the recovery in σ_{SIM} continues even after up to 220 hours. To better understand

these results, the recovery of σ_{SIM} and $\Delta\sigma$ during aging is plotted as a fraction of their total change from the cycling process in Figure 7.2b. For example, the σ_{SIM} of A610 decreased from 145 MPa to about 20 MPa after 1000 cycles, and after 220 hours of aging at room temperature, the σ_{SIM} returned to about 110 MPa, so that 80% of the decrease during cycling was recovered. Here, the recovery of σ_{SIM} for both specimens has exceeded 80% and has not yet stabilized. In other words, it is expected that σ_{SIM} of both specimens will make a nearly full recovery at longer aging times, but total recovery in $\Delta\sigma$ is saturated, before 50% of the initial $\Delta\sigma$ could be recovered. Whatever mechanism is responsible for the decrease in σ_{SIM} during cycling seems to be almost completely reversible, but the same may not be true for the mechanism responsible for the decrease in $\Delta\sigma$.

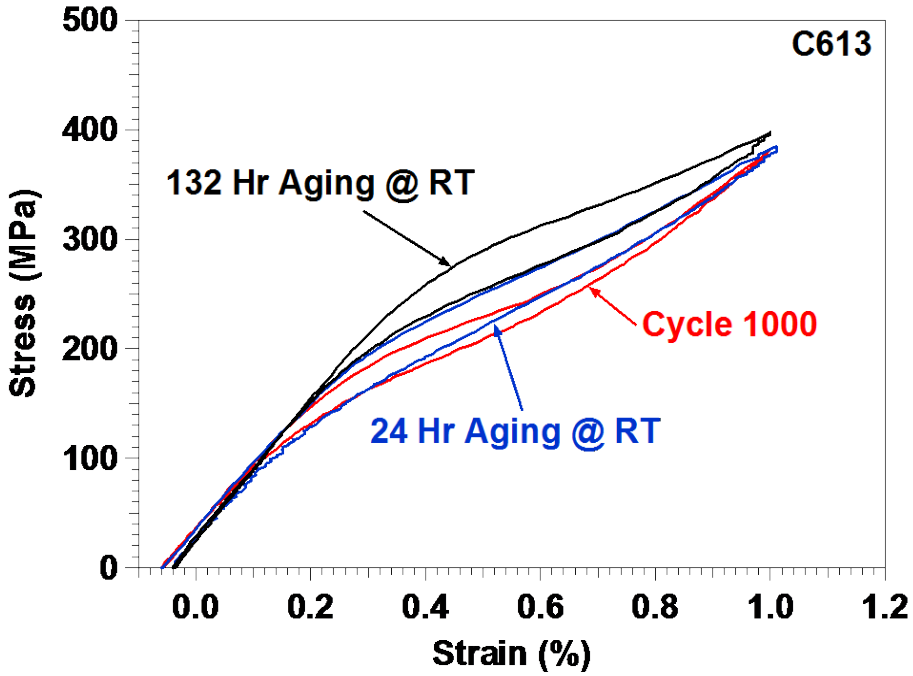

Figure 7.1: Room temperature recovery effect in C613 after superelastic cycling.

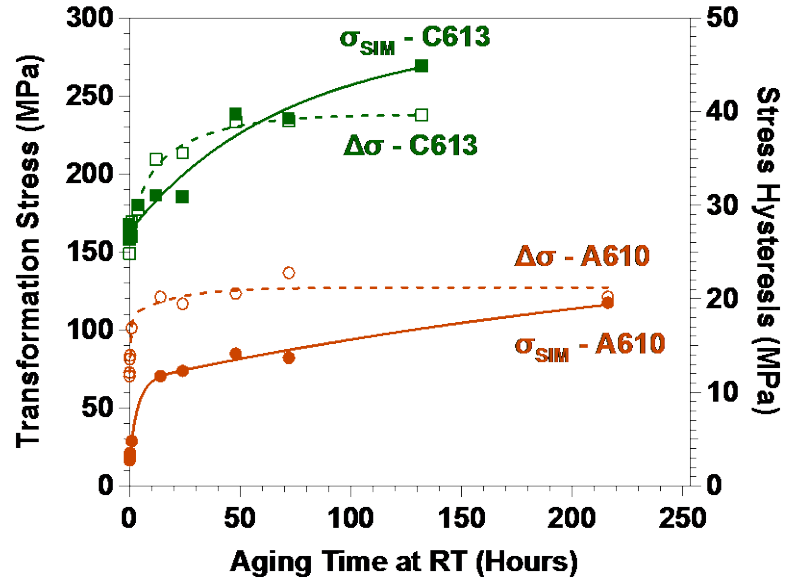

(a)

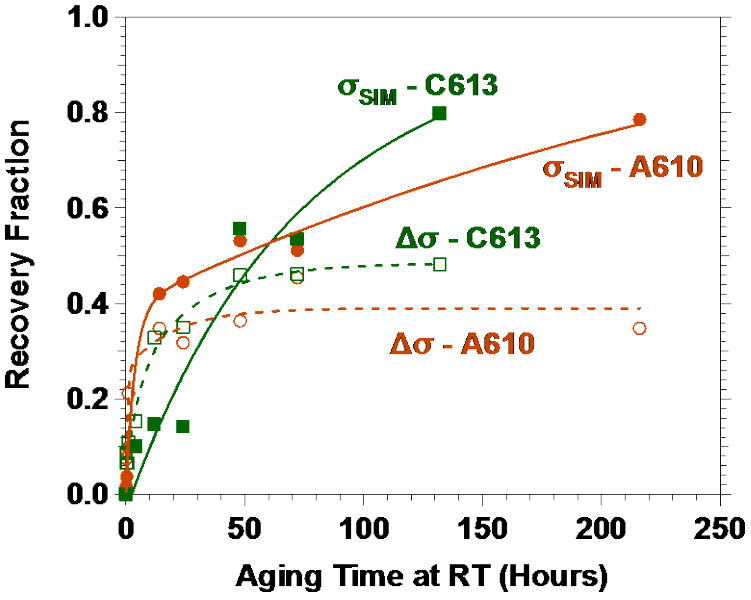

(b)

Figure 7.2: Summary of room temperature recovery effect for a) actual values and b) recovery fraction

Another interesting feature in Figure 7.2b is that the recovery kinetics is different for A610 and C613. The recovery in A610 occurs much more sharply in the initial few hours of aging, but then becomes a more gradual process. On the other hand, the recovery of C613 occurs in a smooth exponential fashion. While the initial microstructure of the respective samples does not have any significant effect on the rate of evolution of σ_{SIM} and $\Delta\sigma$ during the cycling process, they do seem to have an effect during the recovery. In addition to the initial differences in microstructure, the A610 specimens also possess retained martensite at the end of 1000 cycles while retained martensite in C613 has been completely recovered along with ε_{irr} after 1000 cycles. Therefore, the kinetics of recovery in A610 may be somewhat modified by the presence of retained martensite, even though the recovery of σ_{SIM} and $\Delta\sigma$ is not directly caused by the disappearance of retained martensite.

It has been shown that the effects of cycling on the $Ti_{74}Nb_{26}$ alloy are almost completely reversible for the current conditions, provided that the alloy is not plastically deformed at a macroscopic level. Clearly, explanations of the cycling effect based purely on dislocations become unsatisfactory. If only dislocations are responsible for the drop in σ_{SIM}, $\Delta\sigma$, and the buildup of ε_{irr}, then their recovery at room temperature is unexpected. Dislocations are not expected to be very mobile at room temperature since mechanisms for elimination of dislocations require thermally activated climb, which is very difficult at room temperature given the high melting point of the alloy (>2000 °C). Possible explanations based on the rearrangement of dislocations through dislocation glide rather than climb are also inadequate, because ε_{irr} and σ_{SIM} are capable of nearly full recovery, and it is doubtful that the changes in dislocation arrangement caused by superelastic cycling can be reversed through dislocation glide alone, particularly under stress-free conditions at room temperature. Therefore, we believe it is unlikely that dislocations are the primary contributor to the effects of cycling. Rather, they are likely a result of more mobile mechanisms, for example the motion of point defects.

However, it must be clarified that the motion of vacancies from lattice self-diffusion is not considered to be a "mobile point defect" mechanism and is not the likely cause of this recovery process. The kinetics of vacancy movement through self-diffusion is similar to the kinetics of dislocation climb [136] and neither is expected to contribute to recovery at room temperature. Instead, atomic motion through pipe diffusion via dislocations and grain boundary diffusion are expected to be more active. While it is possible that grain boundary diffusion and/or pipe diffusion may still contribute to dislocation climb, they are considered to be different than volumetric lattice diffusion. In Figure 7.2b, the initial recovery process occurs much more quickly in A610 for σ_{SIM}, while the secondary recovery process is slower than that in C613. The smaller grain size and higher dislocation density of C613 make it more susceptible for grain boundary and pipe diffusion, thus possibly contributing to the faster kinetics during secondary recovery in C613. Direct validation of this argument will be challenging, but some indirect evidences for such mechanisms will be the subject of a follow-up study.

The two-stage type recovery trend in Figure 7.2b, and the fact that the dynamic recovery of ε_{irr} occurred only in C613 suggest that more than one mechanism should operate during the recovery process, and that these occur on different time scales. Initially, a fast recovery mechanism dominates, followed by a second mechanism that becomes more important at longer aging times. The kinetics of the initial stage is more rapid in A610, possibly related to the presence of retained martensite in the specimen. Even more interesting is that the recovery in $\Delta\sigma$ seems to end after the first recovery stage and does not appear to be at all affected by the recovery in the second stage. Energy dissipation is very much related to the morphology of the martensite. Large and wide martensite plates result in more energy dissipation thermodynamically than a long and thinner martensite due to the loss of stored elastic energy as the plate widens [137], so the change in $\Delta\sigma$ may be related to the change in the width of martensite plates. Width of the plates may be limited by microstructural features that resist their growth,

such as precipitates, grain boundaries, and possibly point defects and retained martensite. If the growth of the martensite is limited by defects or retained martensite generated during cycling, causing a refinement in the martensite size, then dissipation should also be reduced during cycling. On the other hand, during the first stage of aging, some of these defects or retained martensite is recovered, and $\Delta\sigma$ grows.

Ren and Otsuka [121, 122] have proposed a mechanism based on the short-range order symmetry of point defects known as symmetry-conforming short-range order (SC-SRO) to explain SMA aging behaviors such as martensitic stabilization, rubber-like effect, and two-way shape memory effect. This mechanism acts by the diffusion of point defects, and is a likely explanation for the recovery of σ_{SIM}. As a consequence of the thermoelastic transformation, the first part of the material to transform to martensite during cycling is also the last to revert back to austenite; therefore these parts of the material spend most of the time of cycling in the martensite phase. As such, point defects adapt the symmetry of the martensite in these regions during cycling, thus making it more stable with respect to the austenite and lowering σ_{SIM}. During aging at room temperature after cycling, the material is in the austenite state and the symmetry adapted by the point defects slowly returns to that of the austenite by diffusion, stabilizing it with respect to the martensite and increasing σ_{SIM}. According to Ren and Otsuka [121, 122], the SC-SRO process should, however, not be active for Ni-Ti at room temperature because the melting temperature of Ti-Ni is too high and diffusion proceeds with great difficulty. Using the same argument, recovery should not occur more quickly in Ti-Nb, as this material has an even higher melting point than Ni-Ti. However, the kinetics proposed by Ren and Otsuka concerns mainly the volume self-diffusion in solution treated or well-annealed specimens with fairly large grain sizes and few dislocations [122]. It is again important to note that at room temperature, diffusion rate via grain boundaries and dislocations can be several magnitudes higher than lattice self-diffusion. Therefore, it is very likely that the SC-

SRO remains active in the present specimens at room temperature due to microstructural reasons, and thus, is a possible explanation for the recovery of σ_{SIM} and $\Delta\sigma$ at room temperature.

To determine whether the recovery process is unique to the Ti-Nb SMAs, a similar experiment was performed on a $Ni_{50.8}Ti_{49.2}$ polycrystal. Tension specimens with the same dimensions as the Ti-Nb specimens were solution treated at 1000 °C for 1 hour, water quenched, and then heat treated at 325 °C for 3 minutes. The final stage of this heat treatment was selected following the work of Eucken and Duerig [120] in order to obtain superelasticity in the specimen at room temperature with minimal precipitation (underaged condition). Then, the sample was cycled 1000 times to 4% strain (Figure 7.3). 4% was selected to obtain a similar applied strain to maximum superelastic strain ratio as in the Ti-Nb cases. Then the sample was allowed to age at room temperature without stress for up to 24 hours. No dynamic recovery in ε_{irr} occurred in the Ni-Ti specimen, although recovery in σ_{SIM} and $\Delta\sigma$ similar to that observed in the Ti-Nb specimens was detected (Figure 7.4). It is clear that recovery of the Ni-Ti specimen proceeds much more slowly compared to the Ti-Nb specimens, but also that it resembles the recovery process of A610 more than that of C613. The microstructure of $Ni_{50.8}Ti_{49.2}$ is much closer to A610 than C613 in terms of grain size and dislocation density, and this again suggests that multiple mechanisms are responsible for the recovery, and the relative contribution of the effects of these mechanisms depend on the microstructure of the material.

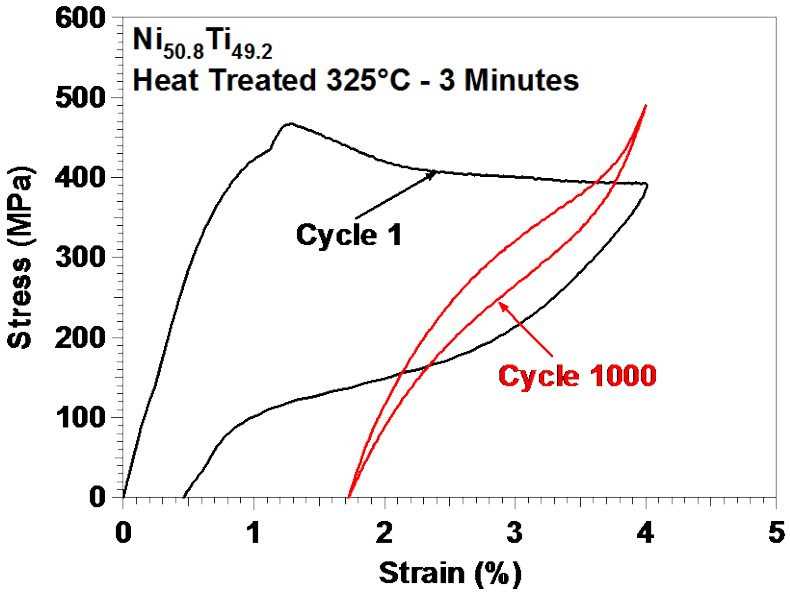

Figure 7.3: Superelastic cyclic response of the $Ni_{50.8}Ti_{49.2}$ shape memory alloy heat treated at 325 °C for 3 minutes.

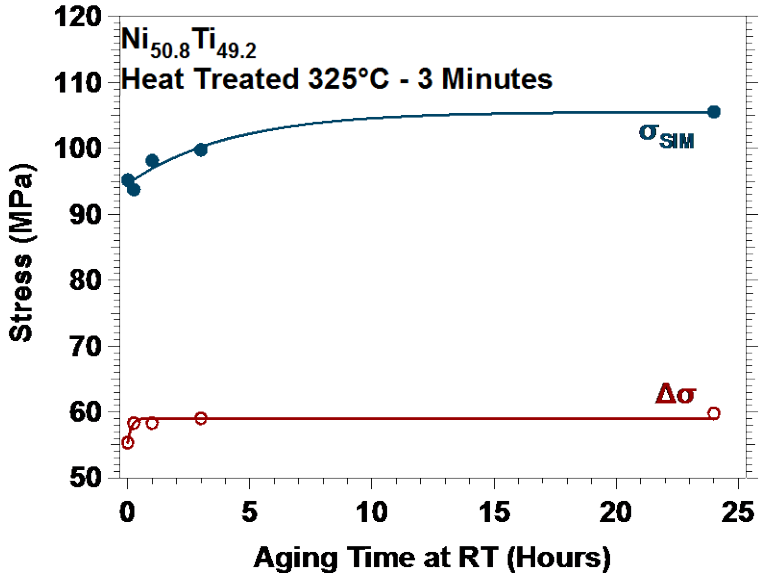

Figure 7.4: Room temperature recovery response of the $Ni_{50.8}Ti_{49.2}$ shape memory alloy heat treated at 325 °C for 3 minutes after 1000 superelastic cycles at room temperature.

The initial microstructure of the $Ni_{50.8}Ti_{49.2}$ specimens should consist of relatively low dislocation density with large grains, so recovery is not anticipated in this condition, but at the end of 1000 superelastic cycles, a sizeable amount of ε_{irr} has been accumulated as seen in Figure 6a. A portion of this ε_{irr} can be attributed to retained martensite, but a large fraction of this strain is likely caused by slip according to Miyazaki *et al.* [117]. As a result of cycling, dislocation density increases in the material [117], and diffusion, thus recovery, becomes easier by dislocation-mediated pipe diffusion. To further confirm this and observe the additional effect of grain boundaries in the recovery process in a Ni-Ti SMA, superelastic cycling and aging experiments were performed on a $Ni_{50.7}Ti_{49.3}$ specimen processed by ECAE at 450°C via route 1A without post-extrusion heat treatment and the results are shown in Figure 7.5 (see [129, 138] for processing and microstructural details). Compared to the solution-treated and underaged $Ni_{50.8}Ti_{49.2}$ specimen, this ECAE-processed Ni-Ti specimen possesses smaller grain size and much higher dislocation density [129, 138] similar to C613, so faster recovery is expected. As seen in Figure 7.5, at the end of 72 hours of room temperature aging, the σ_{SIM} of the ECAE-processed $Ni_{50.7}Ti_{49.3}$ recovered by nearly 50 MPa. On the other hand, σ_{SIM} recovery reached only 10 MPa after 24 hours for the solution-treated, underaged $Ni_{50.8}Ti_{49.2}$ specimen, and an extrapolation suggests that total recovery after 72 hours would still remain far smaller than 50 MPa. Thus, the acceleration of recovery by grain boundaries and dislocations appears to be verified.

While similar room temperature "recovery" has been observed before in Ni-Ti SMAs at time scales on the order of minutes [139], such recovery was caused by the transient temperature change on the specimen as a result of the latent heat of transformation. It was reported for $Ni_{50.6}Ti_{49.4}$ SMA wires that at the end of a few transformation cycles (about 50 cycles), temperature equilibrium is re-established within a few minutes [139], and it is argued that as a result, the recovery in σ_{SIM} and ε_{irr} stops. Unfortunately, these authors did not report the effect of longer static

aging times on σ_{SIM}. In the present case, the increase in σ_{SIM} occurs on a much longer time scale (Figure 7-4), thus, temperature fluctuations are clearly not responsible for the recovery here. Rather, the recovery in the Ni-Ti specimen is believed to be caused by similar mechanisms as the recovery in Ti-Nb.

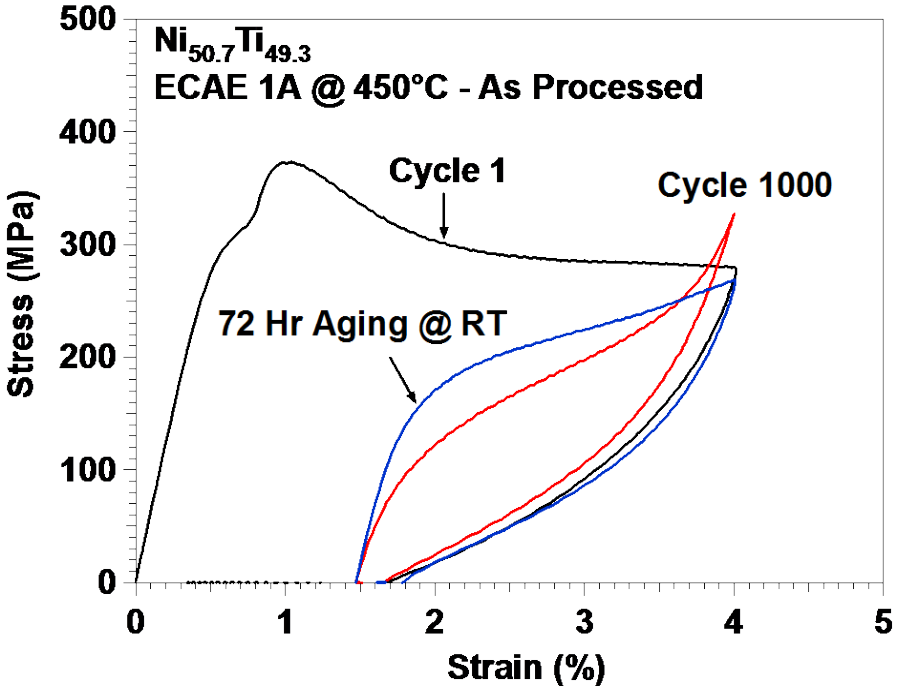

Figure 7.5: Superelastic cyclic response of the $Ni_{50.7}Ti_{49.3}$ shape memory alloy processed by ECAE route 1A at 450 °C.

The nature of the room temperature recovery of σ_{SIM} and $\Delta\sigma$ after superelastic cycling appears to be a universal mechanisms, and not limited to only Ti-Nb and Ni-Ti SMAs. The recovery at room temperature is composed of two separate stages, each driven primarily by a different mechanism. The first stage occurs exclusively on a short time scale on the order of a few hours, and is characterized by a sharp recovery likely caused by the martensite retained after

cycling – possibly from its elimination. The first stage recovery in σ_{SIM} is detected in both A610 and the underaged $Ni_{50.8}Ti_{49.}$ Both materials are believed to contain retained martensite at the end of 1000 cycles, but it should be absent in C613, which has already recovered the retained martensite dynamically during cycling as seen by reduction in ε_{irr} in Figure 5.17c. The second stage occurs at all times, and is a gradual and slow process related to the diffusion of point defects. This stage is accelerated by the presence of small grains and high dislocation density, as shown by the faster recovery kinetics in C613 and ECAE-processed Ni-Ti than A610 and solution-treated and underaged Ni-Ti.

To confirm that retained martensite was involved in the room temperature recovery process, X-ray diffraction experiments were performed on a A610 Ti-Nb specimen before cycling, after 1000 superelastic cycles, and then after 5 days of aging at room temperature. Figure 7.6 shows the x-ray diffraction profile of the 2θ = 68°-74° region of the A610 specimen carried out at room temperature under no stress in its initial state, after 100 superelastic cycles at 2% strain, and after room temperature aging of 5 days. This region was selected because it contains the most visible retained martensite peak after superelastic cycling, following the works of Tahara *et al*. [101]. Here, two peaks are visible: a high intensity austenite peak indexed as (211)β, and a low intensity martensite peak indexed as (202)α''. Initially, the (202)α'' peak is hardly discernible, but after 100 superelastic cycles to 2% strain, it gains visible intensity and signals the presence of retained martensite. After room temperature aging of 5 days, the intensity of the (202)α'' peak has clearly decreased, suggesting that some of the retained martensite has transformed back to austenite during this time. This provides some experimental support for our hypothesis that the initially fast room temperature recovery behavior of A610 is related to the reversion of retained martensite. However, due to the small intensity of the retained martensite peak, it is not clear what magnitude of contribution to room temperature aging effect should be attribute to the isothermal reverse transformation of retained martensite, and whether retained martensite is

the dominate mechanism in the aging behavior. These questions must be addressed with more precise experiments in the future.

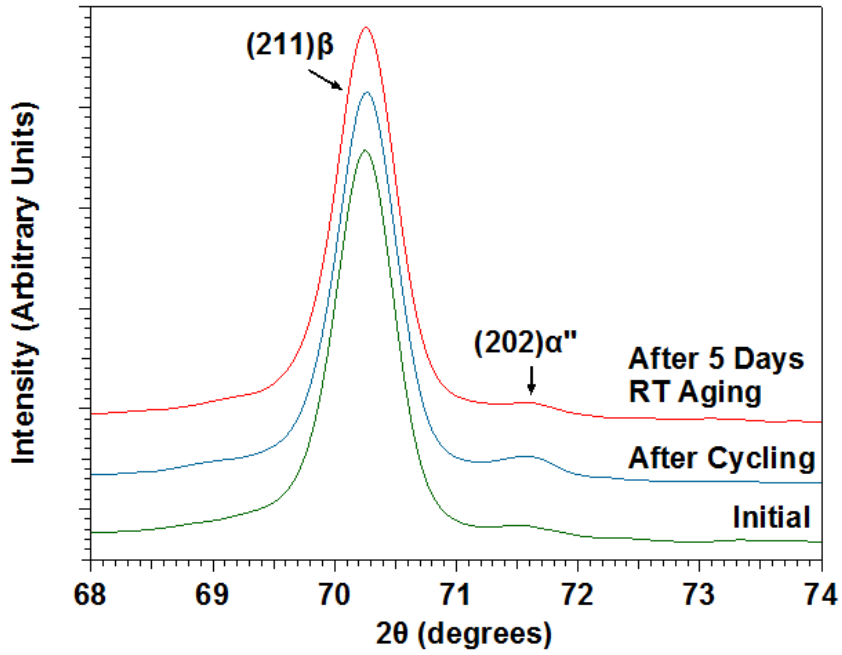

Figure 7.6. Changes to the XRD peak profile of A610 from superelastic cycling and room temperature aging. The martensite peak, not initially discernible, becomes clear after 100 superelastic cycles at 2% strain and indicating the presence of retained martensite after cycling. This is also accompanied by a slight shift in the austenite peak – indicating internal stress after cycling. After 5 days of stress-free aging at room temperature, the intensity of the martensite has decreased, suggesting that a portion of the retained martensite has transformed back to austenite.

Finally, to better understand the kinetics of the recovery phenomenon, the aging experiment was carried out at multiple temperatures between room temperature and 60 °C after 1000 superelastic cycles on A610, and the results for

the recovery of transformation stress, similar to that shown in Figure 7.2b, is presented in Figure 7.7. As expected, the recovery appears to be a thermally activated process, and increasing aging temperature quickly increases the rate at which recovery occurred. Taking the aging time needed for half of the transformation stress lost during cycling to recover for each aging temperature, we construct the Arrhenius-type relationship (Equation 7.1) shown in Figure 7.8.

$$\frac{1}{\tau} \propto e^{\frac{-Q}{RT}} \qquad \text{(Equation 7.1)}$$

where R is the gas constant (8.37 J/molK), T is the temperature in kelvin, τ is the time needed for half recovery, and Q is the activation energy of recovery. The slope of the linear fit corresponds to the activation energy of the recovery process, which was determined to be roughly 10,750 J/mol. This is an order of magnitude lower than empirically determined activation energies for other recovery processes observed in metallurgy, such as recrystallization, which has activation energy of roughly 200,000 J/mol [140]. We were not able to find any known metallurgical processes which similar activation energy, and more experiments would be needed to clarify the exact mechanism of this recovery.

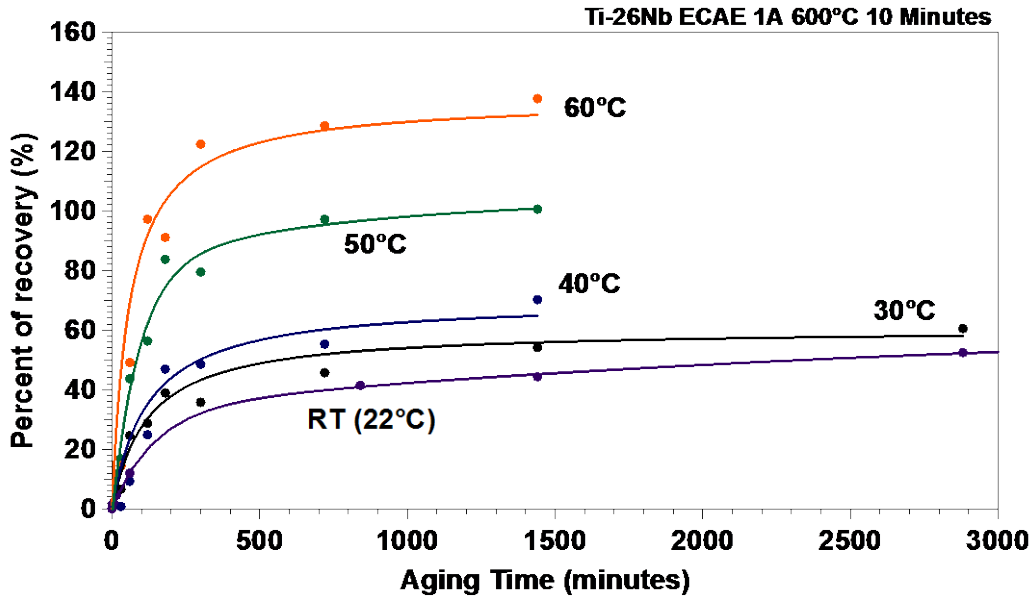

Figure 7.7: Summary of room temperature recovery effect for A610 at various aging temperatures.

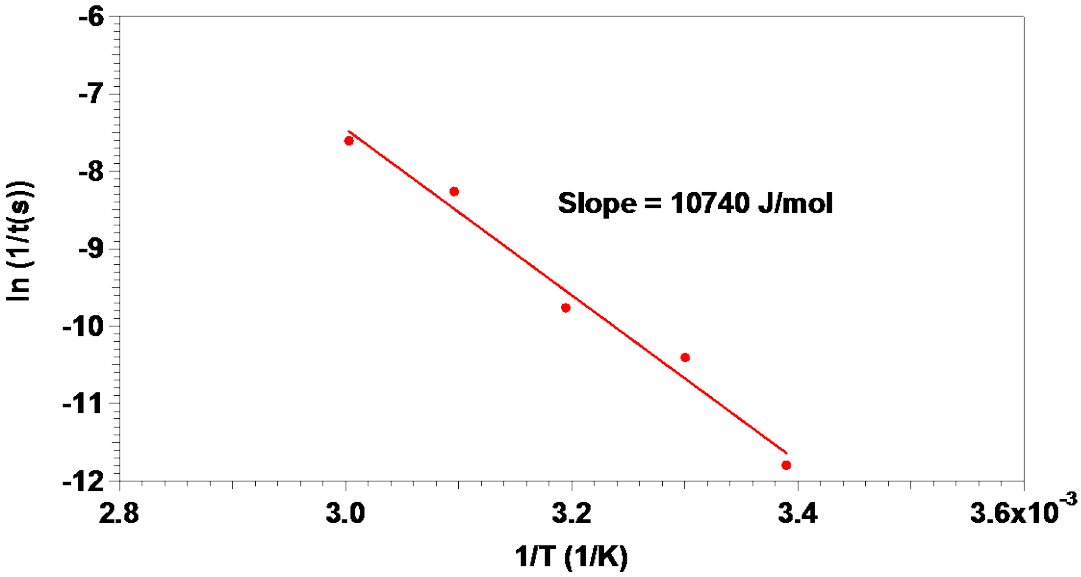

Figure 7.8: Arrhenius relationship generated from time needed for 50% recovery of transformation stresses from data in Figure 7.7. Slope corresponds to the activation energy of the recovery process.

From an application point of view, the observed room temperature recovery can be both beneficial and problematic. Clearly, the increase in σ_{SIM} caused by the recovery increases the effective modulus of the alloy, and is very problematic to the stability of the reduced effective modulus. Since microstructure affects the rate of recovery, it should be possible to optimize the microstructure to retard the recovery process enough such that everyday activity such as walking would be sufficient to maintain the reduced modulus indefinitely. On the other hand, if such a room temperature aging process can be used, then one can effectively reduce the hysteresis of shape memory alloys without changing any of the other properties and improve their efficiency in any application since $\Delta\sigma$ does not completely recover after aging.

7.2. Superelastic memory effect

A phenomenon closely related to the room temperature recovery effect was studied in the course of our studies on the superelastic behavior of $Ti_{74}Nb_{26}$ SMAs. During a study on the superelastic behavior of nickel rich Ni-Ti SMAs, Eucken and Duerig [120] noticed a peculiar behavior: when a specimen was deformed superelastically to a particular strain level and unloaded (the first cycle), then immediately deformed to a higher strain level (the second cycle), the stress level at any given strain value was lower in the second cycle than the first. This is always true beyond the initial elastic region until the strain at which the specimen was unloaded in the first cycle is reached. And only at this strain, the stress of the two cycles is about the same. In other words, the material appears to remember the stress state at the strain when it was unloaded causing a superelastic memory point [120].

Even if the second cycle does not commence immediately after the unloading of the first cycle is completed, the stress difference between the two cycles and superelastic memory point are both maintained. Aging at room temperature for 42 hours after the first cycle does not eliminate this memory point,

nor does it change the differences in stress between the first and second cycles [120]. Thus, the mechanism responsible for the existence of the point is clearly not an anelastic or strain ageing effect. However, if the specimen is heated after the first cycle, the stress difference between the first and second cycle shrinks and is eventually eliminated along with the distinct memory point by increasing heating temperature and duration. The temperature required for such elimination is not high; heating to 150°C for 1 second is enough [120].

This superelastic memory behavior suggests that the process of martensitic transformation generates microstructural "markers" that differentiates regions of the material that have experienced different histories of martensitic transformation. It is the goal of the current study to further characterize the superelastic memory effect in a new SMA, its influence on the stress-strain behavior during superelastic cycling, and to better understand the nature of "markers" that accompanied, if not caused, its existence.

A standard superelastic memory behavior is demonstrated for the $Ti_{74}Nb_{26}$ SMA, for the first time, in scenario 1 of Figure 7.9, similar to Ni-Ti SMAs. The specimen is first deformed to 1% strain, unloaded, then deformed to 1.5%. The maximum superelastic strain in the $Ti_{74}Nb_{26}$ alloys is around 2%, so the partial cycle strains were chosen here to be 1% and 1.5% corresponding to roughly 50% and 75% of the maximum, respectively. Stress level of the 1.5% cycle is lower than that of the 1% cycle up until the memory point at 1% strain – where the first cycle was unloaded. The presence of this behavior gives a distinct two-stage shape to the stress-strain curve of the 1.5% cycle, characterized by a gradual hardening as it approaches the memory point, and followed by a softening immediately past the memory point. In fact, the portion of the 1.5% cycle beyond 1% strain appears to be a continuation of the initial 1% cycle if the specimen was not unloaded.

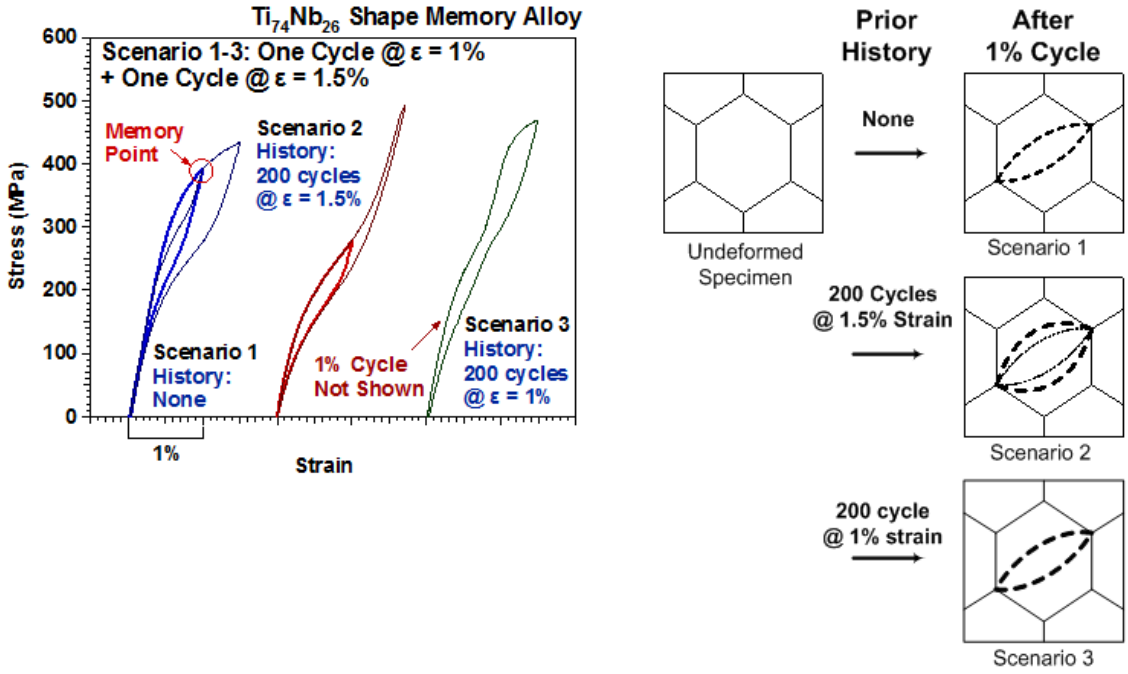

Figure 7.9: Superelastic cycles to 1.5% strain in $Ti_{74}Nb_{26}$ shape memory alloy after three sets of different initial deformation history. (a) shows the stress-strain curves that demonstrate the superelastic memory effect and the influence of deformation history on the appearance of memory point. (b) Schematic representation of relative stability of martensite in various regions of the material prior to the final 1.5% strain superelastic cycle: the lens-shaped regions enclosed by the dashed lines show areas that have already experienced forward and reverse martensitic transformation and, therefore, have an increased martensite stability and oriented internal stress. Thicker lines represent regions that have been transformed multiple times.

The reduction in stress level of the 1.5% cycle before the memory point can be interpreted as a stabilization of martensite in the region of material that experienced transformation in the initial 1% cycle. Martensite stabilization means that the mechanical driving force for the onset of austenite to martensite phase

transformation has increased due likely to a change in the internal stress state. Superelastic cycles generate or rearrange defects in the microstructure, such as dislocations, that give rise to oriented internal stress in regions that have already experienced transformation. Oriented internal stress assists stress-induced martensitic transformation, and also favors particular martensite variants such that its presence creates the two-way shape memory effect (TWSME). Indeed, TWSME was observed in the deformed specimens from our experiments (results not shown), but not in virgin specimens. During unloading, sections of the samples that transformed to martensite revert back to austenite, but the internal stress generated during the forward transformation is retained locally forming a "ghost" region. This is shown by the dotted outlines in the schematics of Figure 7.9. When the specimen is loaded again during the 1.5% cycle, this specific region transforms first. In addition, because of the internal stress generated by the initial 1% cycle, the stress required for transforming a second time is lowered, thus explaining the drop in stress.

Beyond strain of 1%, however, no oriented internal stress exists. Therefore, the stress required for transformation in this portion of the 1.5% cycle remains unaffected. As strain approaches 1%, transformation must make a transition from ghost regions, where martensite was stabilized by internal stress from prior transformation cycles, to regions that have yet to experience transformation (outside the region enclosed by dotted lines in scenario 1 of Figure 7.9). This necessitates a rapid increase in stress up to the memory point at 1% strain. In a martensitic transformation characterized by continuous hardening, as is the case for the $Ti_{74}Nb_{26}$ SMA studied here, the stress-strain curve is smooth and hardening occurs as the applied strain in the 1.5% cycle approach 1% strain. On the other hand, SMAs with a clear plateau region during superelastic deformation, a step-like discontinuity in stress may be seen instead, as is the case for certain Ni-Ti SMAs [120].

Essentially, the superelastic memory point marks the strain boundary between two regions of the material with different levels of martensite stability relative to austenite. Partial superelastic cycles stabilize martensite in one section of the sample relative to other sections. Following this simple explanation, it is possible to predict the behavior of the superelastic stress-strain curve of a sample subjected to various combinations of superelastic cycles to various strain levels. From studies of superelastic cycling behavior, the greatest effects of martensite stabilization occur within the first few cycles, particularly the first cycle [92, 97, 101]. If the specimen is cycled an adequate number of times initially so that the stabilization from an additional cycle becomes negligible, then the drop in stress and memory point should no longer appear. This is demonstrated in scenario 2 of Figure 7.9. Here, the specimen is first cycled to 1.5% strain 200 times. It is then deformed to 1%, unloaded, and deformed to 1.5%. Consequently, memory point and stress drop between the 1% and 1.5% cycles seen in scenario 1 are no longer observed because a strong internal stress field has been created over the entire transforming region of the specimen responsible for the fully reversible 1.5% applied strain (also called 0-1.5% region), upon 200 cycles, enclosed by the bold dotted line in scenario 2 of Figure 7.9b. The additional stabilization in the transforming region from the extra 1% cycle, outlined by the thinner dotted line in the same schematic, becomes negligible. On the other hand, if the specimen is first cycled 200 times to 1%, strong internal stress field in the 0-1% region, shown in scenario 3 of Figure 7.9b, creates a much larger drop in stress in the 1.5% cycle (scenario 3 of Figure 7.9) compared to that of scenario 1 in the same figure.

If the specimen in scenario 1 is deformed to 1.5% once more, the memory point at 1% strain disappears as shown in scenario 4 of Figure 7.10. The reason for this observation can again be attributed to difference in the relative martensite stability between two regions of the sample. After the completion of initial 1.5% cycle, the 0-1% strain region has been cycled twice, and the 1-1.5% strain region once. Since the effect of superelastic deformation is the greatest in the first cycle

when a region is transformed for the first time, the difference in martensite stability is not large enough to maintain a distinct memory point, once the ghost region boundary is expanded with further straining (scenario 4 of Figure 7.10). However, if the specimen is cycled to 1% 200 times instead of only once, the difference in martensite stability becomes large enough so that the memory point could be retained during the second 1.5% strain cycle, as shown in scenario 5 of Figure 7.10.

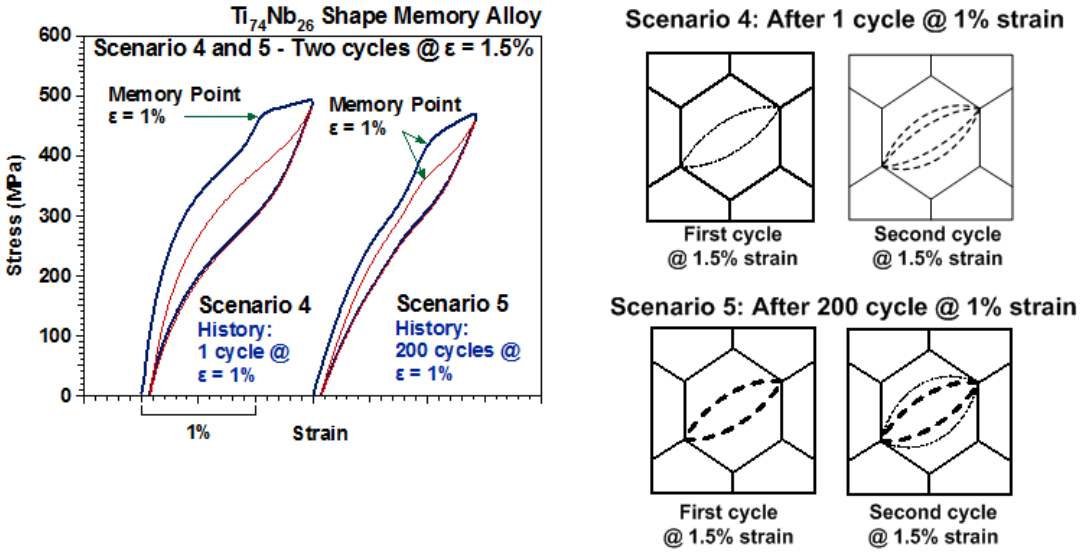

Figure 7.10: (a) Two consecutive superelastic cycles to 1.5% strain after one cycle (scenario 4) and 200 cycles (scenario 5) to 1% strain in the $Ti_{74}Nb_{26}$ shape memory alloy. (b) A schematic demonstrating the martensite stability prior to and after these cycles. The lens-shaped regions enclosed by dashed lines show areas that experienced transformation, and thus, have increased martensite stability. Thicker lines represent regions that transformed multiple times.

Scenario 6 in Figure 7.11 shows two memory points in the stress-strain curve of the $Ti_{26}Nb_{74}$ SMA deformed to 1.6% strain. These memory points are generated by first deforming the specimen once to 1.5% followed by 200 times to 1%. The first memory point indicates a martensite stability differences between the 0-1% strain region and the 1-1.5% strain region, and the second indicates a stability difference between the 1-1.5% region and the 1.5-1.6% region. Multiple memory points can be created along the stress-strain curve using the same procedure. The order at which these regions are stabilized is unimportant because the stability is only affected by the total number of superelastic cycles within each region. However, it is important to note that a cycle from 0-1.5% strain stabilizes both regions of the sample responsible for the 0-1% and 1-1.5% strain intervals, so partial cycle from 1% to 1.5% strain is needed if stabilization is desired only in that section.

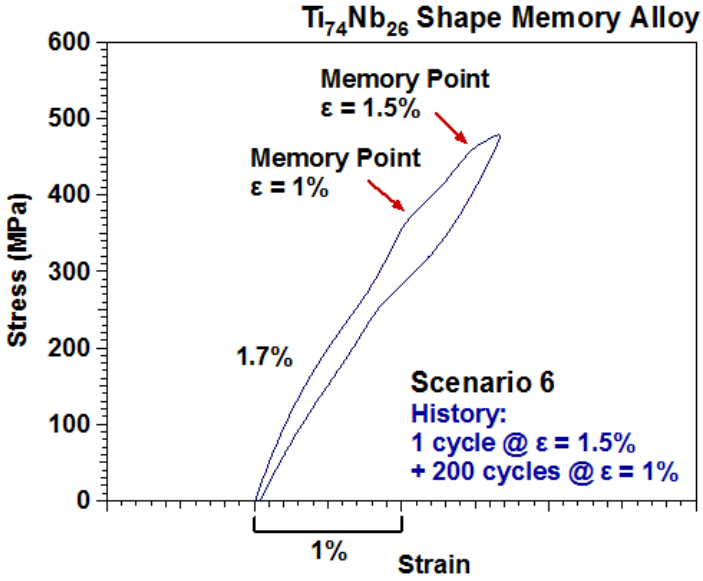

Figure 7.11: Multiple superelastic memory points can be created by forming local regions with different martensite stability through partial superelastic cycling in the $Ti_{74}Nb_{26}$ shape memory alloy.

So far, it has been stated that superelastic cycling causes the creation of localized oriented internal stress, but the mechanisms responsible for this stress have not been discussed. Studies on the superelastic cycling of SMAs suggest that the martensite stabilization, and subsequently the memory point and stress drop, is primarily caused by the creation, and/or rearrangement of dislocations [117-119]. However, Eucken and Duerig [120] questioned this conclusion. They noted that while the drop in stress from cycling is accompanied by the appearance of TWSME, heating the specimen to 150°C recovers the stress drop immediately, but TWSME is retained. This suggests that the two behaviors may not be caused by the same mechanism. TWSME created by deformation cycling is usually attributed to oriented internal stress related to dislocations, so it is expected that heating to 150°C for one second is not enough to erase it. However, it was sufficient to eliminate the memory point and stress drop, so it is likely that a more mobile mechanism is responsible for the martensite stabilization and localized internal stress.

To demonstrate the fast recovery kinetics of the mechanism responsible for the memory point and stress drops, a normal superelastic memory behavior is shown in scenario 7 of Figure 7.12, characterized by the expected stress drop in the 1.5% cycle and memory point following the initial 1% cycle. Surprisingly, if the 1.5% strain cycle is delayed for 3 days by allowing the specimen to rest at room temperature under stress-free conditions, the drop in stress between the two cycles is reduced, as seen in scenario 8 of Figure 7.12. Aging at room temperature is apparently enough to weaken the strength of the internal stress field responsible for the stress drop. As such, we believe that the mechanism responsible for creating the internal stress that causes the martensite stabilization, and associated superelastic memory point and stress drop, is more likely based on the diffusion of point defects – the same mechanisms believed to be responsible for the room temperature recovery of remnant martensite after superelastic cycling discussed in the previous section. It is not clear why reduction in the stress drop from room

temperature aging was not observed by Eucken and Duerig [120], but it is likely due both to the slower recovery kinetics of Ni-Ti SMAs compared to Ti-Nb and the smaller grain size and higher dislocation density in the Ti-Nb SMA studied here.

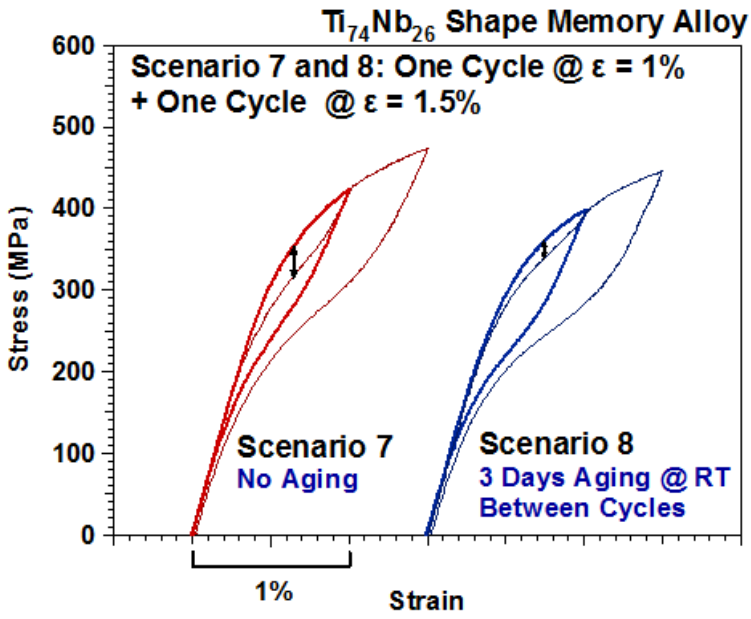

Figure 7.12: Room temperature aging for 3 days weakens the superelastic memory effect in the $Ti_{74}Nb_{26}$ shape memory alloy. The stress drop between two cycles is smaller in scenario 8, where the 1.5% strain cycle is delayed for 3 days, than that in scenario 7 where the 1.5% strain cycle is carried out immediately after the initial 1% cycle, indicating that room temperature aging has restored a portion of stress drop characteristic of the superleastic memory effect.

8. EFFECT OF TERNARY ZIRCONIUM ALLOYING

According to the study of Kim *et al.* [90], ternary alloying of zirconium to the Ti-Nb SMA improves the superelastic properties of the alloy significantly by increasing the transformation strain as well as improving the yielding strength. Therefore, we have added 6 at.% zirconium to the binary Ti-Nb shape memory alloy and studied its mechanical properties, superelastic properties, and superelastic cyclic properties.

Figure 8.1 shows the stress-strain diagram of the as-processed $Ti_{72}Nb_{22}Zr_6$ shape memory alloy processed by ECAE route 1A. Compared to the $Ti_{74}Nb_{26}$ SMA processed by the same ECAE route, the yield strength of the ternary alloy is about 300 MPa higher. Expectedly, the ductility of the ternary alloy is also about 2% lower. Both of these changes are most likely caused by the solution strengthening effect from the larger zirconium atoms.

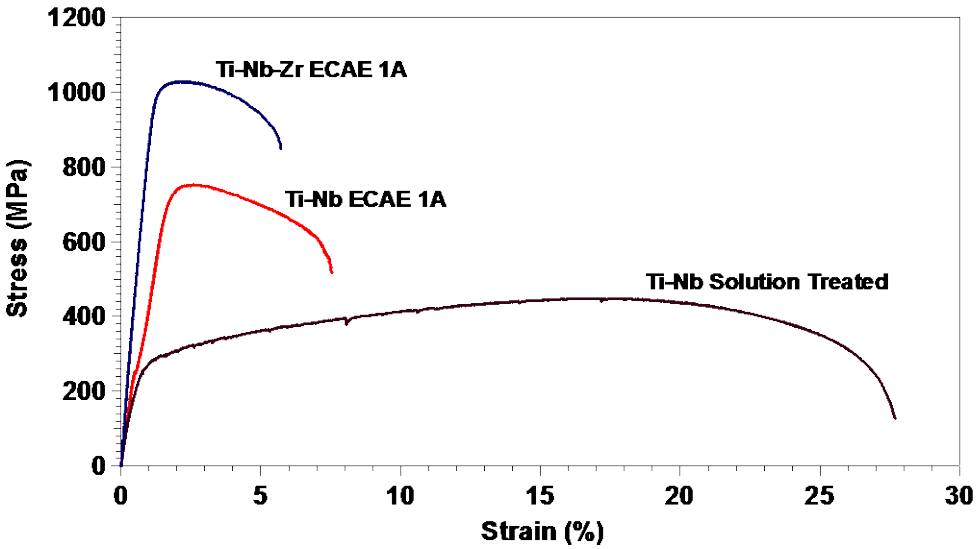

Figure 8.1: Tensile properties of the ternary $Ti_{72}Nb_{22}Zr_6$ shape memory alloy processed by ECAE route 1A compared to $Ti_{74}Nb_{26}$ SMAs under different processing conditions.

The superelastic properties of the $Ti_{72}Nb_{22}Zr_6$ shape memory alloy were evaluated at room temperature in the same fashion as for binary Ti-Nb SMAs as described in section 4.6.1. The ternary SMA was heat treated in an identical way as the A610 binary alloy, and loaded to up to 3% strain in 0.5% intervals at room temperature. Compared to A610 of the binary Ti-Nb alloy (Figure 5.12), the irrecoverable strain levels is much smaller in the ternary alloy, and only 0.5% irrecoverable strain was accumulated after 3% applied strain, as shown in Figure 8.2. In fact, the irrecoverable strain level of the ternary alloy is even lower than the best case (C613) of the binary alloy, which showed about 0.9% irrecoverable strain after 3% applied strain. The reasons for the improved superelastic response are again mostly likely a combination of higher transformation strain levels and resistance to plastic deformation.

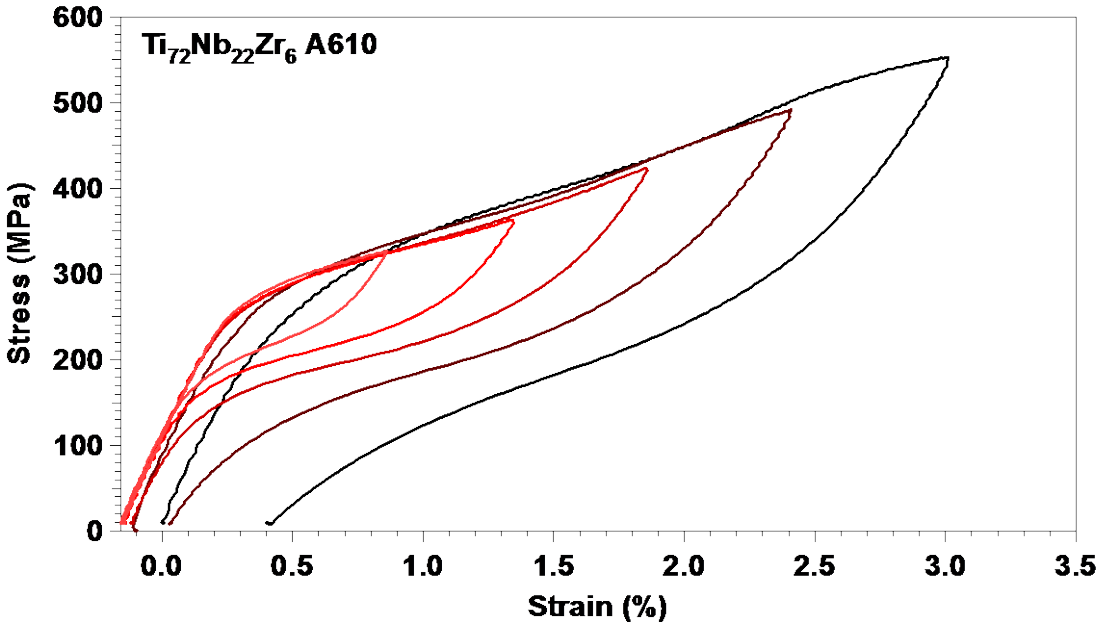

Figure 8.2: Incremental superelastic responses of the $Ti_{72}Nb_{22}Zr_6$ SMA subjected to the same processing conditions as A610 of the binary alloy. Very little irrecoverable strain occurred until the applied strain level of 3% was reached.

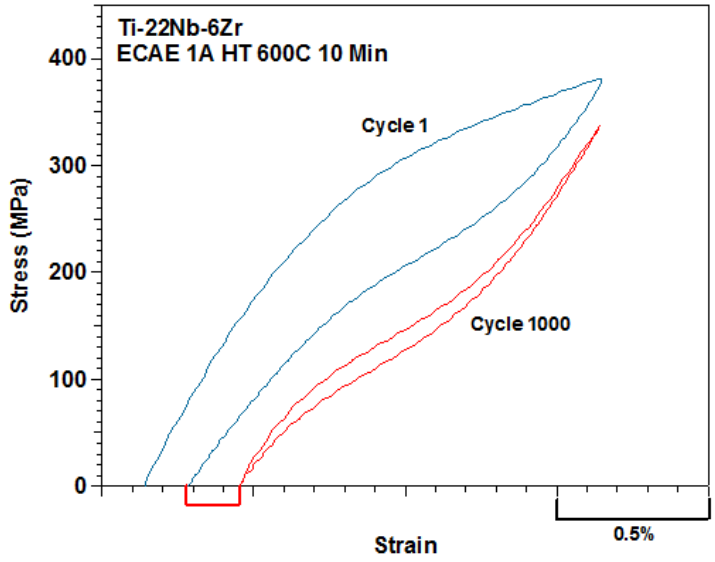

Figure 8.3: Stress-strain response of the $Ti_{72}Nb_{22}Zr_6$ alloy before and after 1000 superelastic cycles at room temperature. The red bracket on the x-axis indicates strain recovery after reheating to 100 °C following the 1000 superelastic cycles.

The superelastic cyclic response of the $Ti_{72}Nb_{22}Zr_6$ SMA is shown in Figure 8.3 and summarized in Figure 8.4 in a similar fashion as Figure 5.18 in section 5-7. Initial transformation stress of the ternary alloy is comparable to that of the binary 1A specimen at about 150 MPa while the total change in transformation stress over 1000 cycles is much smaller. On the other hand, the change in transformation stress over 1000 cycles of the ternary alloy is similar to that for the 4Bc binary specimen. The stress hysteresis levels of the ternary $Ti_{72}Nb_{22}Zr_6$ ECAE 1A specimen heat treated at 600°C is much higher than the binary 1A and 4Bc counterparts, particularly in the first cycle. Three possible reasons contribute to this outcome: it is likely that the effect of solution strengthening also creates an obstacle for the propagation of martensite phase fronts and increase the energy demand for growth of martensite plates. Also, the transformation temperatures of the ternary alloy appear to be lower than either of its binary counterparts,

therefore making it more difficult to induce martensitic transformation by stress at the same temperature. Finally, the very large first-cycle stress hysteresis of the ternary alloy corresponds to its large first-cycle irrecoverable strain shown in Figure 8.2c. Unlike the binary alloys that gradually build up irrecoverable strain over number of cycles, a vast amount of irrecoverable strain occurred after the first cycle in the ternary alloy. It is not clear what portion of this strain is caused by plasticity, but since not all it was recovered after reheating at the end of 1000 cycles, it is reasonable to assume that at least a large fraction was indeed due to slip. Slip results in dissipation of energy, thus explaining the large first cycle stress hysteresis.

The irrecoverable strain level of the ternary $Ti_{72}Nb_{22}Zr_6$ ECAE 1A specimen heat treated at 600°C is comparable to both the 1A and 4Bc binary specimens, but with 2 key differences in their cyclic evolution. First, there is a large buildup in the first cycle for the ternary alloy while buildup is more gradual for the binary specimens. Also, the recovery effect that occurs after 100 cycles, where irrecoverable strain level decreases, is not seen in the ternary specimen. The reason for this is not clear, but if the reduction in irrecoverable strain is explained by dynamic reverse transformation of retained martensite, then it is reasonable for such behavior to be absent in the ternary specimen since transformation temperatures are lower in the ternary specimen.

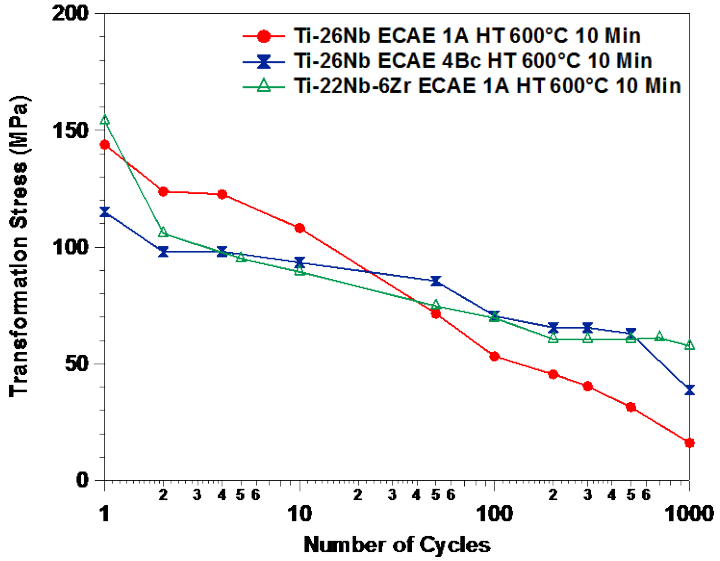

(a)

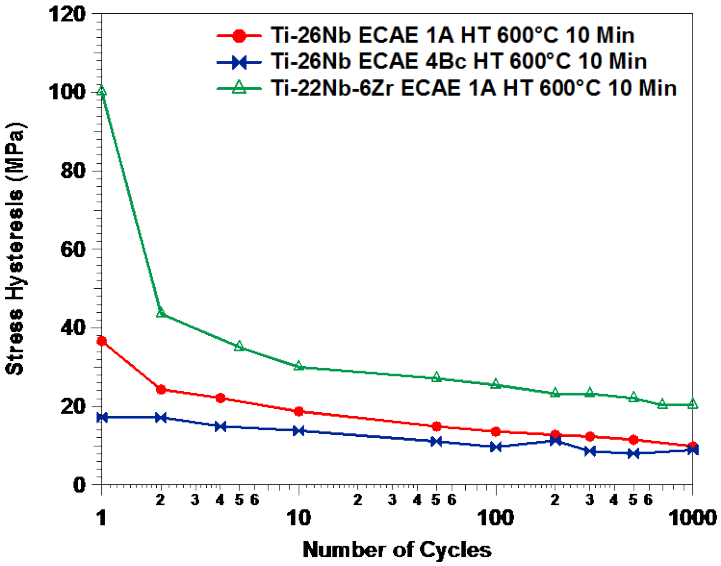

(b)

Figure 8.4. Summary of superelastic cyclic responses of $Ti_{72}Nb_{22}Zr_6$ alloys processed by ECAE route 1A and heat treated for 10 minutes at 600°C compared to similarly heat treated binary $Ti_{74}Nb_{26}$ alloy processed by ECAE route 1A or 4Bc. a) transformation stress, b) stress hysteresis, and c) irrecoverable strain levels.

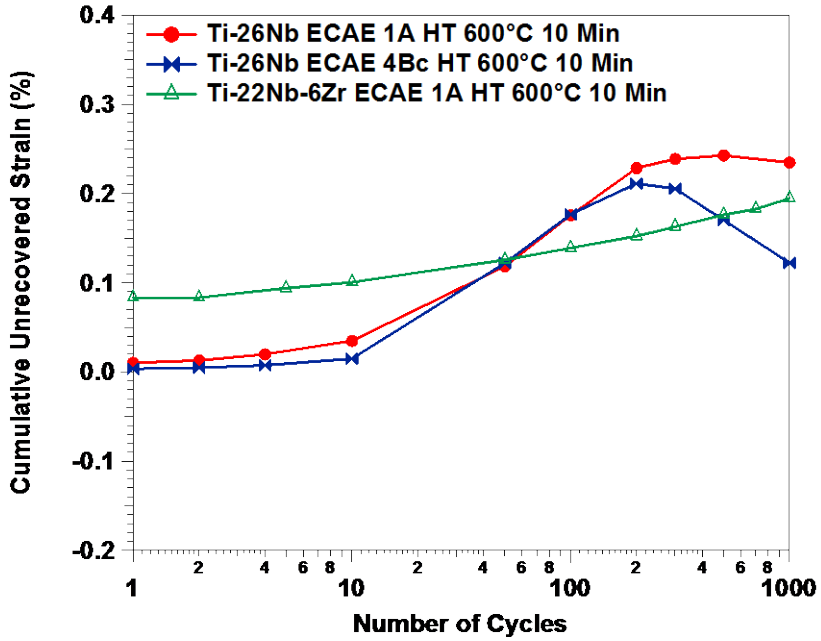

(c)

Figure 8.4 continued.

9. CORROSION RESISTANCE AND BIOCOMPATIBILITY

9.1 Corrosion resistance

To evaluate the corrosion resistance of Ti-26Nb SMAs, potentiodynamic analyses were performed. Figure 9.1 shows the polarization curve of Ti-26Nb immersed in 1M NaCl demonstrated a passive response similar to that of Ti over the potential range examined, consistent with the observations of Wang and Zheng [141]. In contrast, $Ni_{50.8}Ti_{49.2}$ specimens submerged in 1M NaCl showed a breakdown potential at 400 mV relative to the reference electrode. Similar results were observed in the more physiological Hank's Balanced Salt Solution (HBSS) (Figure 9.1b).

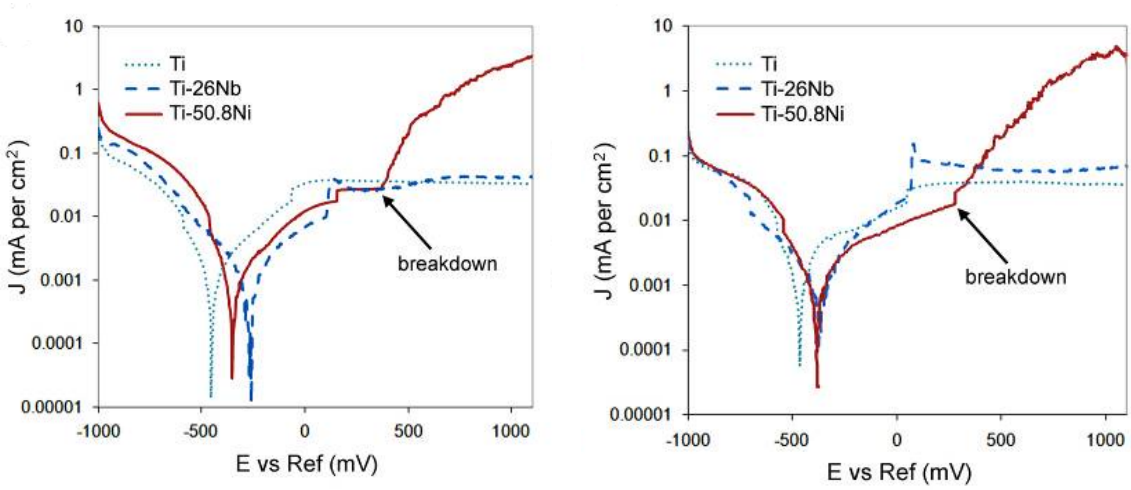

(a) (b)

Figure 9.1: Potentiodynamic corrosion resistance experiments of pure titanium, $Ti_{74}Nb_{26}$, and $Ni_{50.8}Ti_{49.}$ in a) 1M NaCl and b) Hank's Balanced Salt Solution. Breakdown at about +400 mV was observed for the Ni-Ti specimen, but not the others.

The observed Ni-Ti breakdown voltage of +400 mV falls within the 240mV – 1000 mV range reported for Ni-Ti alloys with mechanically polished surfaces [56]. This large variation is related to surface defects such as scratches, residual deformation from polishing, and hard inclusions such as titanium carbides that emerges from the surface. With appropriate surface treatments techniques to thicken the oxide layer, the breakdown voltage could be increased to the 800 mV – 1300 mV under strain-free conditions [56]. However, the corrosion resistance deteriorates rapidly when strain even when 1% strain is applied [142, 143] due to crack formation within surface oxide. Nevertheless, the goal of the present study is not to evaluate the corrosion resistance of Ni-Ti, but rather to compare the corrosion resistance of Ti-Nb to that of Ni-Ti and Ti. From this point of view, bare surfaces of the Ti-Nb SMA does not suffer from breakdown up to 2000 mV, which suggest that the inherent corrosion resistance of Ti-Nb is superior to that of Ni-Ti. It also means that the corrosion resistance of Ti-Nb is less sensitive to surface conditions than that of Ni-Ti, and that Ti-Nb does not require the same level of stringent surface processing as needed for Ni-Ti to maintain excellent corrosion resistance.

Although this is the first direct comparison of the corrosion resistance of Ni-Ti and Ti-Nb SMAs, these results are in agreement with a previous corrosion study comparing Ni-Ti SMAs with Ti-Nb alloys outside of the shape memory composition range. Specifically, Godley *et al.* [110] found that $Ti_{70.3}Nb_{29.1}$ alloys, which do not exhibit shape memory behavior or superelasticity at room temperature, have improved corrosion resistance over $Ti_{50}Ni_{50}$ SMAs in both neutral and acidic solutions. The improved corrosion resistance observed for Ti-Nb SMAs relative to Ni-Ti is also consistent with previous literature [144].

9.2 Cytotoxicity and ion leaching

To study the effect of metal ion release on the viability of cells, cytotoxicity experiments were conducted on NIH/3T3, a cell line derived from embryonic

fibroblasts of mice. As these experiments were the work of our collaborators, experimental details will not be provided in here, and only results will be discussed as they are pertinent to the overall scope of this work, as well as necessary for the introduction of surface composition studies detailed in section 9.3. Interested readers are referred to a separate dissertation [108] for further explanation on cytotoxicity and ion release experiments.

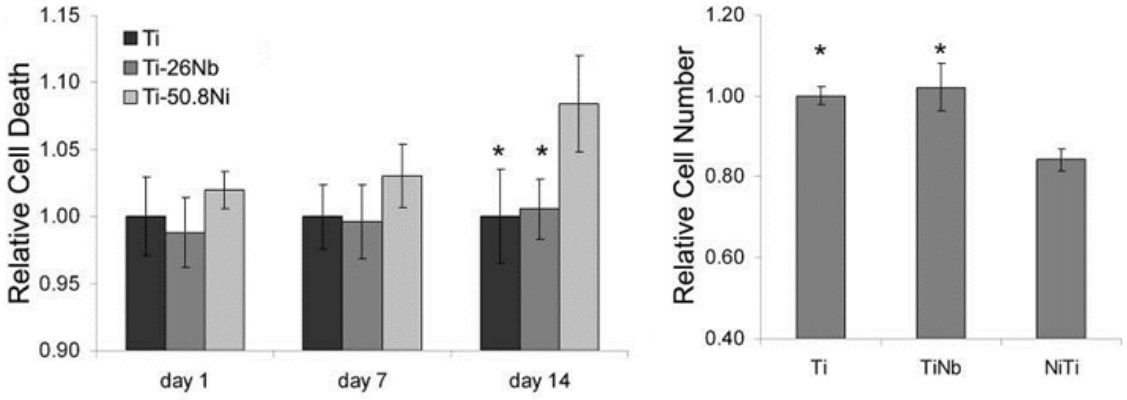

(a) (b)

Figure 9.2: Cytotoxicity experimental results for pure Ti, $Ti_{74}Nb_{26}$, and $Ni_{50.8}Ti_{49.}$ a) The relative death after 1 day, 7 days and 14 days exposure to the metal, and b) shows the relative survival rate of cells after 14 days exposure [101].

Figure 9.2 shows the result to cytotoxicity of pure titanium, $Ti_{74}Nb_{26}$, and $Ni_{50.8}Ti_{49}$. The results indicate that the $Ni_{50.8}Ti_{49}$ SMAs were somewhat more toxic than the $Ti_{74}Nb_{26}$ and pure Ti samples, whereas $Ti_{74}Nb_{26}$ and Ti were similar in their cytocompatibility. Although a number of studies have indicated that Ni-Ti SMAs to be at least as biocompatible as pure Ti [48,, 55, 56, 59] the present data are in agreement with several studies that have demonstrated Ni-Ti SMAs to have

increased toxicity relative to pure Ti [145, 146]. In addition, the current results are consistent with the observations of Wang and Zhang [Wang 2009], who found $Ti_{84}Nb_{16}$ to possess similar cytocompatibility as pure Ti.

The cytotoxicity of the corrosion products varies widely for cells of different organisms [56]. For example, exposure of human blood lymphocytes to bulk Ni-Ti surface treated by autoclaving in steam or water evoked little adverse cellular response, while rat blood lymphocytes exposed to similarly processed Ni-Ti actually showed an improved stimulation in cell proliferation. On the other hand, when exposed to porous Ni-Ti, which has higher surface area, the proliferation of the rat lymphocyte was almost completely suppressed, similar to the effect of pure nickel, while the reduction of human lymphocytes is only about 30%. The cells (NIH/3T3) used in the present study is a mouse fibroblast line, so it is possible that for human cells, the cytotoxicity response may be different. One certainty among the sometimes contradictory findings on the cytotoxicity of Ni-Ti in published literature is that higher nickel release and higher concentration of nickel atoms at the surface of the alloy are correlated with reduced cell viability. Therefore, it is important to concentrate on the specific mechanism of metal release on cytotoxicity; this is the reason that we chose to conduct an indirect contact study. In this case, the results are expected to depend only on the identity and amount of metallic corrosion products and minimize the direct effect of surface features on cell viability since cells do not come in direct contact with the specimen. Since both the Ni-Ti and Ti-Nb specimens were polished to the exact same final finish (0.05 μm), the surface roughness, the surface area of the two specimens are expected to be similar.

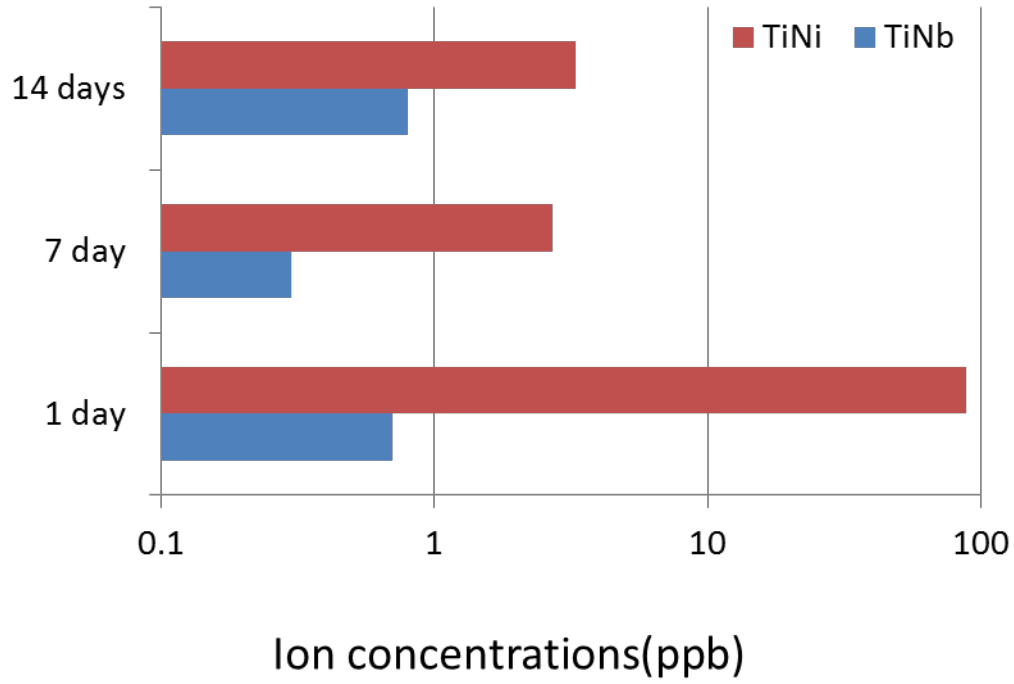

Figure 9.3: Ion release into the cell culture during the cytotoxicity experiment. Nickel ion release is shown for the Ni-Ti alloy, and niobium ion release is shown for Ti-Nb.

Figure 9.3 summarizes the ion released from the cultured $Ti_{74}Nb_{26}$, $Ni_{50.8}Ti_{49}$, and Ti samples. There is an initial burst release of Ni ions from the $Ni_{50.8}Ti_{49}$ alloys at day 1. By day 7, however, the Ni ion levels released from the $Ni_{50.8}Ti_{49}$ SMAs could not be distinguished from the background Ni ion readings for the $Ni_{50.8}Ti_{49}$ and Ti specimens. Despite the decreased day 7 and day 14 Ni ion release, the cytotoxicity measures for the Ni-Ti samples increased significantly between these two time points. The present Ni ion release values for Ni-Ti correlate well with previous literature [147], and, when combined with the cytotoxicity data, suggest that Ni ion exposure has long-term effects on cell viability. This observation

would be consistent with previous work which demonstrates long-term effects on cell viability following acute Ni ion exposure [148].

For the $Ti_{74}Nb_{26}$ specimens, the highest release of Nb ions was approximately a 100-fold lower than the peak release of Ni ions from the $Ni_{50.8}Ti_{49}$ samples. This result indicates an increased resistance to ion leaching in the $Ti_{74}Nb_{26}$ samples, which correlates well with the increased passivity of the $Ti_{74}Nb_{26}$ relative to the $Ni_{50.8}Ti_{49}$ SMAs indicated by the potentiodynamic tests.

While the difference between the ion release level of Ni and Nb are quite dramatic, it highlights not so much the quantity of nickel release in Ni-Ti, but rather the complete lack of ion release of the Ti-Nb alloy. Titanium and niobium are both non-essential to the human body, and long been believed to be biologically safe. However, some recent studies have questioned the biocompatibility of titanium [56, 149-151], and it is possible that such concerns may be valid for niobium as well. It is likely that similar to nickel, any potential toxic effects of titanium and niobium would increase with increased metal leaching or corrosion byproduct. However, we showed that unlike nickel, the amount of titanium and niobium in solution are negligible. It is unlikely that they can cause adverse biological response at such a low concentration.

9.3. Surface depth profile and surface composition after cytotoxicity experiments

To gain further insight into alterations in alloy surface composition following immersion in physiological culture media, secondary ion mass spectrometry (SIMS) data collected from the samples employed in the cytotoxicity studies were compared to freshly polished surfaces. Due to the nature of SIMS analyses, differences in the intensity of signals obtained for disparate ions within a given sample cannot be interpreted as a difference in ion levels. In addition, differences in the intensities of a specific ion cannot be directly compared across specimens. However, trends in ratios of two ion signals with sample depth can be

effectively compared across samples. Therefore, to assess the effect of ion leaching on the sample surface composition, the ratio of the Nb signal to the Ti signal was computed for each Ti-Nb surface. These first ratios also corrected for variations in sputtering beam strength, since both signals were collected simultaneously for a single surface. The average Nb/Ti ratio for the immersed, cytotoxicity samples was than divided by the corresponding average ratio for the polished surfaces. A similar process was pursued for the Ni-Ti specimens.

As shown in Figure 9.4, the ratio was significantly less than 1 for the Ni-Ti samples at initial sputtering times before recovering to the "steady-state" value of 1 at longer sputtering times (i.e. increasingly internal sample regions). The initial Ni/Ti ratio indicates a loss of Ni and/or enrichment in Ti in the buffer-exposed surface layers relative to initial surface layer values. On the other hand, the Nb/Ti ration is initially greater than one, and then fluctuates somewhat before stabilizing. A loss of Ni from Ni-Ti surfaces would be in agreement with observed Ni ion release. In addition, a Nb loss significantly less than that of Ni would again be consistent ion release data.

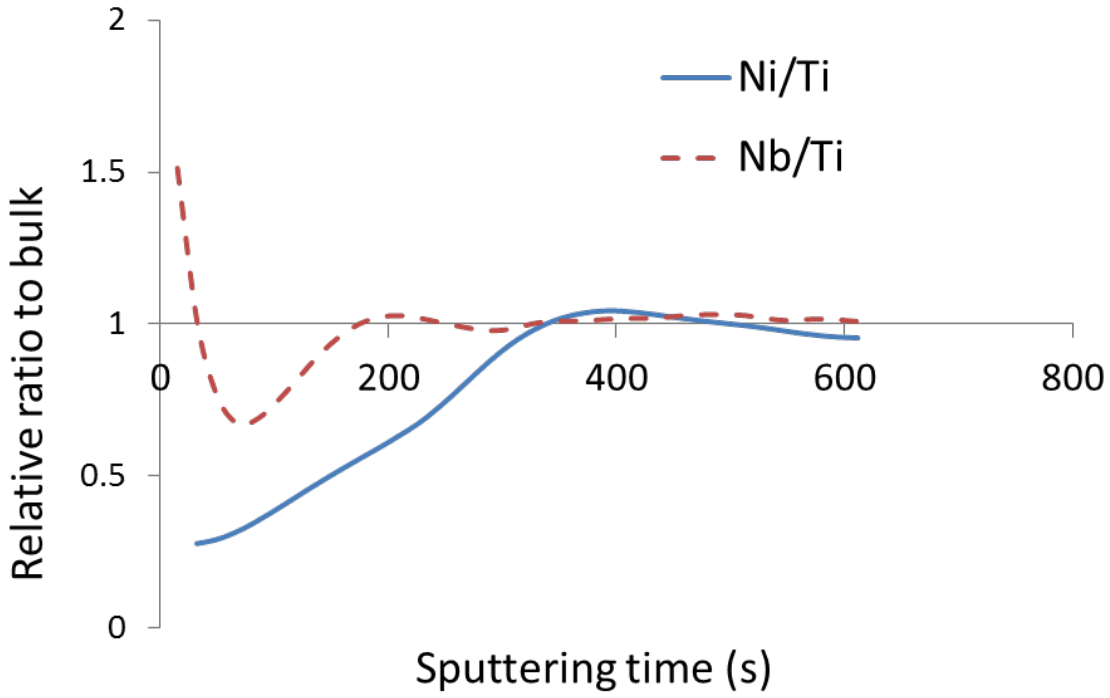

Figure 9.4: The Ni/Ti and Nb/Ti ratios of the Ni-Ti and Ti-Nb specimens after cytotoxicity experiments relative to the bulk composition as a function of sputtering time (thus depth beneath the surface). While the Nb/Ti ratio is higher than 1 near the surface, meaning the surface of Ti-Nb is niobium-rich, the Ni/Ti ratio is less than 1 near the surface, which suggests nickel depletion near the surface of the Ni-Ti SMA.

10. FATIGUE CRACK GROWTH BEHAVIOR

Implants are often expected to have a lifetime of ten years or more, and as a result, they undergo millions of cycles of deformation. Thus in addition to sufficient resistance to plastic deformation, biomedical implant alloys must also possess adequate resistance to fatigue and crack growth.

Using a compact tension (CT) setup, the fatigue crack growth rate was characterized for the $Ti_{74}Nb_{26}$ A610 SMA at ambient conditions as well as in the corrosive environment (Hank's Balanced Salt Solution). The crack growth rate (da/dN) vs. stress intensity range (ΔK) is shown in Figure 10.1. The data follows the classic Paris Law relationship of fatigue crack, which is expressed as follows:

$$da/dN = C\Delta K^m \qquad \text{(Equation 10.1)}$$

where C is a constant and m is the Paris Exponent.

The threshold stress intensity factor (ΔK_{th}) for the Ti-Nb SMA extrapolates to about 2 MPa $m^{1/2}$, which is similar to the values of hot-rolled Ni-Ti SMAs and about 5 times larger than cold-drawn Ni-Ti samples [152], as seen in Figure 10.2. Compared to an ultrafine grained NbZr conventional (non-shape memory) alloy, the crack growth rate of the Ti-Nb SMA is initially much faster at low K values, but experiences a "shoulder" starting about 3.5 MPa $m^{1/2}$. Starting from this point, the crack grows very slowly in the specimen until a K value of 9 MPa $m^{1/2}$ is reached. The crack growth rate of Ti-Nb then becomes identical to that of the Nb-Zr alloy from there on.

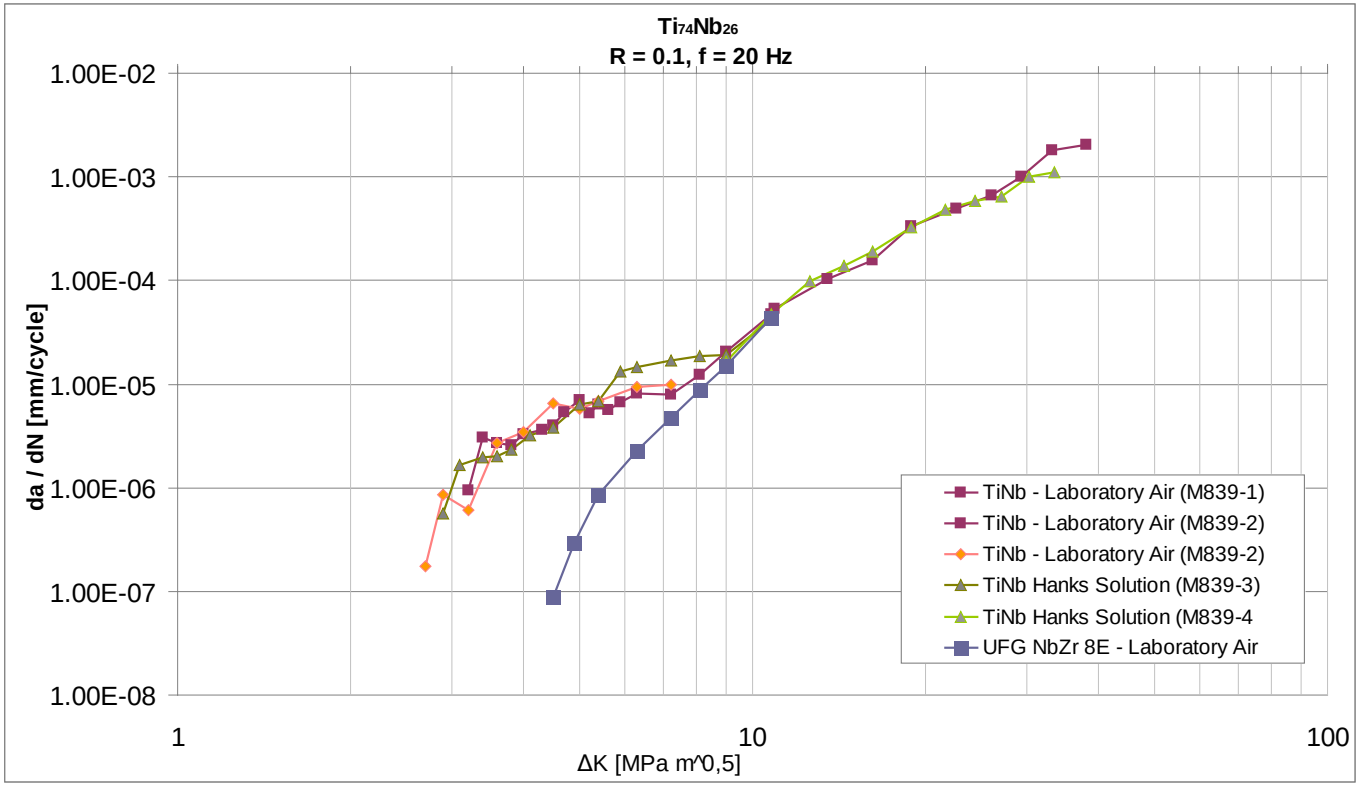

Figure 10.1. Fatigue crack growth plot of the Ti-Nb A610 SMA under ambient conditions and in a corrosive Hank's solution compared to the behavior of an ultrafine grained Nb-Zr alloy.

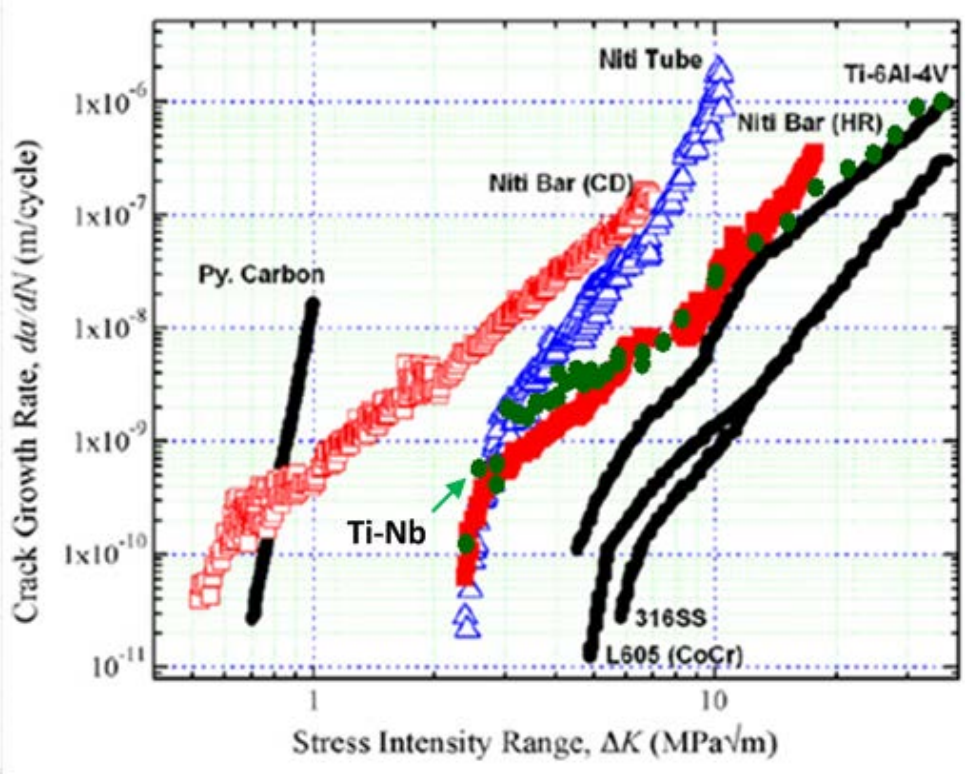

Figure 10.2: Fatigue crack growth plot of the Ni-Ti SMA and various other biomedical alloys under ambient conditions compared to the Ti-Nb A610 alloy [152].

Overall, the Paris-Law profile of $Ti_{74}Nb_{26}$ A610 is comparable to other biomedical alloys at higher ΔK levels. At lower ΔK levels, the growth rate of cracks is about twice as fast in the Ti-Nb A610 shape memory alloy as in conventional biomedical alloys. However, at higher ΔK levels, the crack growth rate of Ti-Nb and other biomedical alloys converge. This means that at high applied stress levels or when the crack length is large, the Ti-Nb SMA behaves identically in fatigue as other biomedical materials. On the other hand, when the stress is low or when crack length is short, the fatigue properties of the Ti-Nb SMA are inferior to that of other biomedical alloys. The same observations can be made for the Ni-Ti shape memory alloys.

The “shoulder” is observed at the low stress intensity range for the Ti-Nb SMA was also observed in the crack growth response of the Ni-Ti SMA [152], and is likely a feature brought about by the superelasticity of SMAs. The reason for this behavior is not clear, but is likely to be caused by the stress-induced transformation. In the region where this transformation is active, stress concentration at the crack tip could be dissipated by phase transformation, causing the rate of crack growth to be relatively insensitive to a change in ΔK. Therefore, stress-induced transformation acts similarly to plastic deformation as a deformation mechanism to dull the crack tip. Overall, the fatigue properties of the Ti-Nb A610 sample and hot rolled Ni-Ti shape memory alloys are similar.

Figure 10.2 shows the Paris Law curve for several Ni-Ti specimens in different conditions, and the fatigue crack growth properties of these specimens depend heavily on processing conditions, and thus microstructure. The hot rolled (HR) Ni-Ti sample shows the best fatigue crack growth behavior, while the cold-drawn (CD) specimen is the worst. The threshold ΔK of the hot rolled Ni-Ti sample is about 4 times larger than that of the CD specimen. It is expected that similar microstructure dependence of fatigue crack growth rate would apply for the Ti-Nb SMA. Since A610 is a heavily deformed sample that was annealed for a short period of time, it is expected that its fatigue crack resistance would be better than the as-ECAE extruded sample, but worse than a solution-treated sample.

Finally, there was no difference in the crack growth rate between specimens tested in open air and those tested in Hank’s Solution, as shown in Figure 10.1. This means that fatigue resistance of the alloy is not affected by the level of corrosion experienced in vivo. Corrosion-fatigue is often cited as a major issue [31, 143] in biomedical alloys, and corrosion often causes the fatigue resistance of the alloy to deteriorate. Ti-Nb does appear to suffer in its fatigue crack resistance under corrosive conditions, making the Ti-Nb SMA an attractive option for biomedical applications. It is most related to the superior corrosion resistance of the Ti-Nb SMA.

11. SUMMARY AND CONCLUSIONS

11.1 Summary

Through the series of experiments conducted in this study, we successfully engineered a $Ti_{74}Nb_{26}$ shape memory alloy with excellent biocompatibility, corrosion resistance, adequate mechanical strength and fatigue resistance, and ultra-low effective elastic modulus enabled by cyclic-induced softening. Low-cycle fatigue caused the critical stress level of stress-induced martensitic transformation to drop below 20 MPa at room temperature, and resulted in an effective modulus as low as 22 GPa. Because of the non-linear nature of the stress-strain curve after cycling, the alloy is also able to spontaneously lower its effective modulus to adjust to any potential resorption in the surrounding bone, transferring more of the load to it. This combination of low effective modulus and self-adjustability makes Ti-Nb a potent candidate biomedical alloy for combating stress shielding in implants.

By using a combination of equal channel angular extrusion and post-extrusion heat treatments, the strength of the $Ti_{74}Nb_{26}$ shape memory was effectively increased 2-3 times over that of the solution-treated specimen. At the same time, shape memory and superelastic strains were doubled. Microstructure appears to play the major role in the determination of mechanical and shape memory properties and reduction in grain size and precipitation hardening were both effective in improving shape memory and superelastic behavior of the alloy. Crystallographic texture, while differing in specimens of various processing conditions, does not appear to have a significant effect on strength or shape memory behavior. Further ternary alloying by 6 at.% zirconium was effective in further improving the superelastic properties of the alloy by increasing both yield strength and transformation strain.

A large obstacle facing the potential application of the low-modulus Ti-Nb SMAs is a recovery phenomenon at low temperature whereby the effect of low-cycle fatigue are reversed, increasing the effective modulus in the process. The

magnitude of this recovery depends on the microstructure of the alloy and appears to be related to the disappearance of retained martensite during cycling. The recovery is thermally activated with a very low activation energy an order of magnitude below that of other known recovery processes such as recrystallization. The cycling and recovery behaviors gave rise to a related phenomenon where the material "memorizes" its loading history during superelastic experiments. This memory can then be erased by low temperature annealing.

The biocompatibility and corrosion resistance of the Ti-Nb SMA are both at least equal to that of the Ni-Ti SMA. Ti-Nb does not suffer from ion leaching that compromises the biocompatibility of the Ni-Ti SMA, and show no significant changes in surface composition after long-term exposure to corrosive media. Finally, the fatigue resistance of the Ti-Nb SMA remains comparable to other biomedical alloys, and does not appear to suffer from fatigue-corrosion under Hank's Solution. This combination of properties allows the Ti-Nb SMAs to be a viable and potentially powerful alloy for biomedical implant applications.

11.2 Conclusions

From the experimental results presented in this work, the following conclusion can be made:

11.2.1 Mechanical properties and Equal channel angular extrusion

1. Equal channel angular extrusion (ECAE) is capable of effectively improving the yield strength of the $Ti_{74}Nb_{26}$ shape memory alloy through work hardening and grain refinement.

2. ECAE is not effective in controlling the crystallographic texture of the $Ti_{74}Nb_{26}$ shape memory alloy due to the weak deformation texture of the bcc unit cell.

3. Comparing to literature result, ECAE does not offer significant benefits over conventional cold rolling above 90% reduction in thickness.

11.2.2 Shape memory and superelastic properties

1. Dislocations play conflicting roles on transformation temperatures: moderate dislocation density increases transformation temperatures, while heavy dislocation density decreases them.

2. Largest transformation strain in the $Ti_{74}Nb_{26}$ shape memory alloy can be obtained in specimens with moderate dislocation density and grain sizes in the 1-10 μm range. Higher dislocation density suppresses transformation and superelastic properties deteriorate.

3. Ternary zirconium addition increases both transformation strain and strength of the alloy.

11.2.3 Reduction of effective modulus

1. Superelastic cycling enables reduction in effective modulus by reducing the transformation stress σ_{SIM} levels.

2. Precipitate-free specimens with moderate dislocation densities allows for the lowest σ_{SIM} to be achieved after cycling.

3. Effective modulus decreases with increasing applied stress and increasing number of superelastic cycles. Effective modulus as low as 22 GPa was achieved in the $Ti_{74}Nb_{26}$ SMA.

4. Since effective modulus decreases with increasing applied stress, this allows the material to automatically reduce its modulus when load exceeds its desired level, thus transferring load to its surrounding.

11.2.4 Room temperature recovery effects

1. Recovery at room temperature in σ_{SIM} and $\Delta\sigma$ occurs in all Ti-Nb and Ti-Nb-Zr specimens after superelastic cycling, and is most likely a universal phenomenon to SMAs.

2. The recovery is related to retained martensite and is not likely dislocation-driven, but possibly related to accelerated diffusion process at grain boundaries or through dislocations.

3. Activation energy for recovery is lower than that of any know recovery mechanism in metallurgy.

11.2.5 Corrosion resistance and biocompatibility

1. Superb biocompatibility of the Ti-Nb SMA is related to the reluctance of niobium ions to break free from the alloy surface.

11.2.6 Fatigue crack resistance

1. Threshold stress intensity factor of the Ti-Nb SMA is comparable to other biomedical alloys, thus it is expected that it is suitable for application.

2. Corrosion-fatigue does not compromise fatigue resistance of the Ti-Nb SMA.

REFERENCES

[1] Maier B, New York Times, December 16, 2010, online, http://www.nytimes.com/2010/12/17/business/17hip.html.

[2] Maier B, New York Times, December 27, 2011, online, http://www.nytimes.com/2011/12/28/business/the-high-cost-of-failing-artificial-hips.html.

[3] Maier B, New York Times, June 25, 2011, online, http://www.nytimes.com/2011/06/26/health/26innovate.html.

[4] Langton DJ, Jameson SS, Joyce TJ, Hallab NJ, Natu S, Nargol AVF, J Bone Joint Surg Br, 2010;92B:38.

[5] Long M, Rack HJ, Biomaterials, 1998;19:1621.

[6] Rack HJ, Qazi JI, Mater Sci Eng C 2006;26:1269.

[7] Geetha M, Singh AK, Asokamani R, Gogia AK, Prog Mater Sci 2009;54:397.

[8] Nasab MB, Hassan MR, Trends Biomater Artif Organs 2010;24:69.

[9] Bobyn JD, Mortimer ES, Glassman AH, Engh CA, Miller JE, Brookes CM, Clin Orthop Relat R 1992;274:79.

[10] Glassman AH, Bobyn JD, Tanzer M, Clin Orthop Relat R 2006;453:64.

[11] Engh CA, Young AM, Engh CA, Hopper RH, Clin Orthop Relat R 2003;417:157.

[12] Harris WH, Clin Orthop Relat R 1992;274:121.

[13] Huiskes R, Weinans H, van Rietbergen B, Clin Orthop Relat R 1992;274:124.

[14] Race A, Miller MA, Izant TH, Mann KA, J Biomech 2011;44:2345.

[15] Wik TS, Foss OA, Havik S, Person L, Aamodt A, Witso E, Acta Orthop 2010;81:765.

[16] Venesmaa PK, Kroger HP, Jurvelin J, Miettinen HJ, Suomalainen OT, Alhava EM, Acta Orthop Scand 2003;74:31.

[17] Wolff J, Das gesetz der transformation der knochen, reprint. Berlin: Pro Business; 2010.

[18] Niinomi M, Nakai M, Int J Biomater, 2011;2011:836587.
[19] McAuley JP, Culpepper WJ, Engh CA, Clin Orthop Relat R 1998;355:182.
[20] McAuley JP, Sychterz CJ, Engh CA, Clin Orthop Relat R 2000;371:146.
[21] Christofolini I, Juszczyk M, Taddei F, Field RE, Rushton N, Viceconti M, P I Mech Eng 2009;223:27.
[22] Batchelor AW, Service characteristics of biomedical materials and implants, , London: Imperial College Press; 2004.
[23] Scott, DF, Jaffe WL, J Arthroplasty 1996;11:319.
[24] American Academy of Orthopedic Surgeons, 2010, online, http://orthoinfo.aaos.org/topic.cfm?topic=A00355.
[25] Khachin V, Rev de Phys App 1989;24:733.
[26] Kaufman L, Prog Metal Phys 1958;7:165.
[27] Nishiyama Z, Martensitic transformations, New York: Academic Press; 1978.
[28] Shimizu K, Tadaki T, Shape memory effect: mechanism, in: Funakubo H (Ed), Shape memory alloys, New York: Gordon and Breach; 1987.
[29] Cahn, RW, Acta Metall Mater 1953;1:49.
[30] Christian JW, Theory of structural transformation in solids, New York: John Wiley; 1983.
[31] Christian JW, Mahajan S, Prog Mater Sci1995;39:1.
[32] Mackenzie JK, Bowles JS, Acta Metall Mater 1957;5:137.
[33] Otsuka K, Ren X, Prog Mater Sci 2005;50:511.
[34] Sehitoglu H, Karaman I, Anderson R, Zhang X, Gall K, Maier HJ, Chumlyakov Y, Acta Mater 2000;48:3311.
[35] Wechsler MS, Lieberman DS, Read TA, T Am I Met Eng 1953;197:1503.
[36] Saburi T, Wayman C, Acta Metall Mater 1979;27:979.
[37] Aaronson H, Laughlin D, Sekerka R, Wayman C, Proceedings of the International Conference on Solid-Solid Phase Transformations, Warrendale: AIME; 1981.
[38] Madangopal K, Acta Mater 1997;45:5347.

[39] Otsuka K, Mater Sci Forum, 1990;56-58:393.

[40] Grummon D, JOM 2003;55:24.

[41] Kumar PK, Lagoudas D, Introduction to shape memory alloys, in: Lagoudas D, (Ed), Shape memory alloys: modeling and engineering applications, New York : Springer; 2008.

[42] Liu Y, Xiang H, J Alloy Compd 1998;270:154.

[43] Rajagopal S, Little AL, Bourke MAM, Vaidyanathan R, App Phys Lett 2005;86:081901.

[44] Wagner MFX, Windl W, Acta Mater 2008;56:6322.

[45] Qiu S, Clausen B, Padula SA, Noebe RD, Vaidyanathan R, Acta Mater 2011;59:5055.

[46] Peltonen L Contact Dermatitis 1979;5:27.

[47] Hildebrand H, Veron C, Martin P, Biomaterials 1989;10:545.

[48] Putters JLM, Kaulesar Sukul DMKS, De Zeeuw GR, Bijma A, Besselink PA, Eur Surg Res 1992;24:378.

[49] Laing, PG, Ferguson, AB, Hodges, ES, J Biomed Maters Res 1967;1:135.

[50] Wataha JC, O'Dell NL, Singh BB, Ghazi M, Whitford GM, Lockwood, P.E., J Biomed Maters Res 2001;58:537.

[51] Coogan TP, Latta DM, Snow ET, Costa M, Crit Rev Toxicol 1989;19:341.

[52] Hartwig A, Krüger I, Beyersmann D, Toxicol Lett 1994;72:353.

[53] Takahashi S, Takeda E, Kubota Y, Okayasu Y, Radiat Res 2000;154:686.

[54] Heintz C, Riepe G, Birken L, Kaiser E, Chakfé N, Morlock M, Delling G, Imig H, J Endovasc Ther 2001;8:248.

[55] Shabalovskaya SA, Int Mater Rev 2001;46:233.

[56] Shabalovskaya SA, Bio-Med Mater Eng 2002;12:69.

[57] Castleman LS, Motzkin SM, Alicandri FP, Bonawit VL, Johnson AA, J Biomed Mater Res 1979;10:695.

[58] Ryhänen J, Minim Invasiv Ther 2000;9:99.

[59] Es-Souni Mohammed, Es-Souni Martha, Fischer-Brandies H, Anal Bioanal Chem 2005;381:557.
[60] Hassel AW, Minim Invasiv Ther 2004;13:240.
[61] Shevchenko N, Pham MT, Maitz MF, Appl Surf Sci 2004;235:126.
[62] Ditlea S, Sci Am 2002;287:60.
[63] Shih CC, Lin SJ, Chen YL, Su YY, Lai ST, Wu GJ, Kwok CF, Chung KH, J Biomed Mater Res 2000;52:395.
[64] Shih CC, Shih CM, Chen YL, Su YY, Shih JS, Kwok CF, Lin SF, J Biomed Mater Res 2001;57:200.
[65] Duda SH, Pusich B, Richter G, Landwehr P, Oliva VL, Tielbeek A, Wiesinger B, Hak JB, Tielemans H, Ziemer G, Cristea E, Lansky A, Beregi JP, Circulation 2002;106:1505.
[66] Nakanishi T, Kondoh C, Kishikawa T, Satomi G, Nakazawa M, Imai Y, Momma K, Heart Vessels 1994;9:40.
[67] Knirsch W, Haas NA, Lewin MAG. Uhlemann F, Catheter Cardio Inte 2003;58:116.
[68] Wataha JC, Lockwood PE, Marek M, Ghazi M, J Biomed Mater Res 1999;45:251.
[69]Jacobs TS, Won J, Gravereauz EC, Faries PL, Morrissey N, Teodorescu VJ, Hollier LD, Marin ML, J Vasc Surg 2003;37:16.
[70] Palmaz JC, Bailey S, Marton D, Sprague E, J Vasc Surg 2002;36:1031.
[71] Riepe G, Heintz C, Kairser E, Chakfé N, Morlock M, Delling G, Imig H, Eur J Vasc Surg 2002;24:117.
[72] Perry SB, J Am Coll Cardio 1993;21:A261.
[73] Kim HY, Ohmatsu Y, Kim JI, Inamura T, Hosoda H, Miyazaki S, Mater Trans 2006;47:518.
[74] Maeshima T, Nishida M, Mater Trans 2004;45:1096.
[75] Blackburn MJ, Williams JC, T Metall Soc AIME 1968;242:2461.
[76] Blackburn MJ, Feeney JA, J I Met 1971;99:132.
[77] Davis R, Flower HM, West DRF, J Mater Sci 1979;14:712.

[78] Sutuo Y, Yamauchi K, Suzuko M, Furukawa A, Omori T, Takagi T, Kainuma R, Nishida M, Ishida K, Minim Invasiv Ther 2006;15:204.
[79] Baker C, Met Sci, 1971;5:92.
[80] Horiuchi Y, Inamura T, Kim HY, Miyazaki S, Wakashima K, Hosoda H, Mater Trans 2006;47:1209.
[81] Hosoda H, Fukui Y, Inamura T, Wakashima K, Miyazaki S, Inoue K, Mater Sci Forum 2003;426-432:3121.
[82] Hosoda H, Fukui Y, Inamura T, Wakashima K, Miyazaki S, Mater Sci Forum 2005;475-479:2329.
[83] Hosoda H, Kinoshita Y, Fukui Y, Inamura T, Wakashima K, Kim HY, Miyazaki S, Mater Sci Eng A 2006;438-440:870.
[84] Inamura T, Fukui Y, Hosoda H, Wakashima K, Miyazaki S, Mater Sci Forum 2005;475-479:2323.
[85] Inamura T, Fukui Y, Hosoda H, Wakashima K, Miyazaki S, Mater Sci Eng C 2005;25:426.
[86] Balcerzak AT, Sass SL, Metall Trans 1972;3:1601.
[87] Brammer WG, Rhodes CG, Philos Mag 1967;16:477.
[88] Brown ARG, Clark D, Eastabrook J, Jepson KS, Nature 1964;201:914.
[89] Kim HY, Satoru H, Kim JI, Hosoda H, Miyazaki S, Mater Trans 2004;45:2443.
[90] Kim JI, Kim HY, Inamura T, Hosoda H, Miyazaki S, Mater Sci Eng A 2005;403:334.
[91] Kim JI, Kim HY, Hosoda H, Miyazaki S, Maters Trans 2005;46:852.
[92] Kim HY, Ikehara Y, Kim JI, Hosoda H, Miyazaki S, Acta Mater 2006;54:2419.
[93] Kim HY, Hashimoto S, Kim JI, Inamura T, Hosoda H, Miyazaki S, Mater Sci Eng A 2006;417:120.
[94] Kim HY, Sasaki T, Okutsu K, Kim JI, Inamura T, Hosoda H, Miyazaki S, Acta Mater 2006;54:423.
[95] Masumoto K, Horiuchi Y, Inamura T, Hosoda H, Wakashima K, Kim HY, Miyazaki S, Mater Sci Eng A 2006;438-440:835.

[96] Miyazaki S, Kim HY, Hosoda H, Mater Sci Eng A 2006;438-440:18.
[97] Ma J, Karaman I, Maier HJ, Chumlyakov YI, Acta Mater 2010;58:2216.
[98] Ma J, Karaman I, Chumlyakov YI, Scripta Mater 2010;63:265.
[99] Ping DH, Mitarai Y, Yin FX, Scripta Mater 2005;52:1287.
[100] Ping DH, Cui CY, Yin FX, Yamabe-Mitarai Y, Scripta Mater 2006;54:1305.
[101] Tahara M, Kim HY, Hosoda H, Miyazaki S, Acta Mater 2009;57:2461.
[102] Takahashi E, Sakurai T, Watanabe S, Masahashi N, Hanada S, Mater Trans 2002;43:2978.
[103] Nitta K, Watanabe S, Masahashi N, Hosoda H, Hanada S, Proceedings of the International Symposium of Structural Biomaterials for the 21th Century, Warrendale: TMS; 2001.
[104] Sakaguchi N, Niinomi M, Akahori T, Takeda J, Toda H Mater Sci Eng C 2005;25:363.
[105] Tang X, Ahmed T, Rack HJ, J Mater Sci 2000;35:1805.
[106] Koster R, Vieluf D, Kiehn M, Sommerauer M, Kahler J, Baldus S, Meinzertz T, Hamm CW, Lancet 2000;356:1895.
[107] Matsuno H, Yokoyama A, Watari F, Uo M, Kawasaki T, Biomaterials 2002;22:1253.
[108] McMahon RE, Tissue engineering approaches for the treatment of knee joint damage. Dissertation, Texas A&M University, 2011.
[109] Metikoš-Huković M, Kwokal A, Piljac J, Biomaterials 2003;24:3765.
[110] Godley R, Starosvetsky D, Gotman I, J Mater Sci-Mater M 2006;17:63.
[111] Lee CM, Ju CP, Chern Lin JH, J Oral Rehab 2002;29:314.
[112] Kikuchi M, Takahashi M, Okuno O, Dent Mater J 2003;22:328.
[113] Valiev RZ, Langdon TG, Prog Mater Sci 2006;51:881.
[114] Vinogradov A, Ishida T, Kitagawa K, Kopylov VI, Acta Mater 2005;53:2181.
[115] Haouaoui M, Hartwig KT, Payzant EA, Acta Mater 2005;53:801.
[116] Segal VM, Goforth RE, Hartwig KT, U.S. Patent No. 5,400,633, 1995.
[117] Miyazaki S, Imai T, Igo Y, Otsuka K, Metall Trans A. 1986;17A:115.

[118] Gall K, Maier HJ, Acta Mater 2002;50:4643.
[119] Sade M, Damiani C, Gastien R, Lovey FC, Malarría J, Yawny A, Smart Mater Struct 2007;16:S126.
[120] Eucken S, Duerig TW, Acta Metall Mater 1989;37:2245.
[121] Ren X, Otsuka K, Nature 1997;389:579.
[122] Otsuka K, Ren X, Mater Sci Eng A 2001;312:207.
[123] Hartl DJ, Lagoudas D, Thermomechanical characterization of shape memory alloys, in: Lagoudas D, (Ed.), Shape memory alloys: modeling and engineering applications, New York: Springer; 2008.
[124] Hanawa T, Ota M, Biomaterials 1991;12:767.
[125] American Society of Testing Materials. I. subcommittee E08.06, E647: in: ASTM Book of Standards, 2005.
[126] Ball JM, James RD, Arch Ration Mech An 1987;100:13.
[127] Kitamura K, Miyazaki S, Iwai H, Kohl M, Mater Sci Eng A 1999;273-275:758.
[128] Miyazaki S, No VH, Kitamura K, Khantachawana A, Hosoda H, Int J Plasticity 2000;16:1135.
[129] Kockar B, Karaman I, Kim J, Chumlyakov Y, Scripta Mater 2006;54:2203.
[130] Lin HC, Wu SK, Chou TS, Kao HP, Acta Metall Mater 1991;39:2069.
[131] Miyazaki S, Igo Y, Otsuka K, Acta Metall Mater 1986;34:2045.
[132] Moffat DL, Phase transformation in the titanium-niobium binary alloy system, Dissertation, The University of Wisconsin – Madison, 1985.
[133] Moffat DL, Larbalestier DC Metall Trans A 1988;19:1677.
[134] Hosford WF, Mechanical behavior of materials, Cambridge: Cambridge University Press; 2005.
[135] Yang PF, Bruggemann GP, Rittweger J, J Musculoskelet Neuronal Interact 2011;11:8.
[136] Kassner ME, Pérez-Prado MT, Prog Mater Sci 2000;45:1.
[137] Wollants P, Roos JR, Delaey L, Prog Mater Sci 1993;37:227.
[138] Karaman I, Kulkarni AV, Luo ZP, Philos Mag 2005;85:1729.

[139] Paradis A, Terriault P, Brailovski V, Torra V, Smart Mater Struct 2008;17:065027.
[140] Reed-Hill RE, Abbaschian R, Physical metallurgy principles, Boston: PWS Publishing Company; 1994.
[141] Wang YB, Zheng YF, Mater Lett 2009;63:1293.
[142] Hessing C, Frenzel J, Pohl M, Shabalovskaya S, Mater Sci Eng A 2008;486:461.
[143] Shabalovskaya S, Acta Biomater 2008;4:447.
[144] Yeung KWK, Poon RWY, Chu PK, Chung CY, Liu XY, Lu WW, J Biomed Mater Res A 2007;82A:403.
[145] Assad M, Lombardi S, Berneche S, Desrosiers EA, Yahia LH, Rivard CH. Ann Chir 1994;48:731.
[146] Takeshita F, Takata H, Ayukawa Y, Suetsugu T, Biomaterials 1997;18:21.
[147] El Medawar L, Rocher P, Hornez JC, Traisnel M, Breme J, Hildebrand HF. Biomol Eng 2002;19:153.
[148] Coen N, Mothersill C, Kadhim M, Wright EG, J Pathol 2001;195:293.
[149] Williams DF, Biocompatibility of clinical implant materials, Boca Raton, FL: CRC Press; 1981.
[150] Rogers SD, Howie DW, Graves SE, Pearcy MJ, Haynes DR, J Bone Joint Surg 1997;79B:311.
[151] Wang JY, Wicklund BH, Gustilo RB, Tsukayama DT, Biomaterials 1996;17:2233.
[152] Gall K, Tyber J, Wilkesanders G, Robertson S, Ritchie RO, Maier HJ, Mater Sci Eng A 2008;486:389.

VITA

Name: Ji Ma

Address: Department of Mechanical Engineering
Texas A&M University, MS 3123
College Station, TX 77843

Email Address: thatwasandy@gmail.com

Education: B.S., Civil Engineering, Texas A&M University, 2008
Ph.D, Mechanical Engineering, Texas A&M University, 2012